Biogeochemical Investigations on the Atlantic Meridional Transect of R/V Kronprins Haakon, 2018

Master Thesis in

Chemical Oceanography

Lise Bagne Apelthun

20. November 2019

UNIVERSITY OF BERGEN

GEOPHYSICAL INSTITUTE

Acknowledgment

I want to thank my brilliant supervisors, Are Olsen, Meike Becker and Tatiana Tsagaraki for all the guidance, support, education and valuable feedbacks. I appreciate all the time and effort you have given me this past year.

I would also like to thank everyone who made it possible for me to cross the Atlantic Ocean with R/V Kronprins Haakon and everyone who helped me with the measurements: Are Olsen, Kristin Jackson, Meike Becker, Tatiana Tsagaraki, Pål Tore Mørkved, Sigve Naustdal, Agneta Fransson, Gunnar Bratbak, Jorun Karin Egge, Elzbieta Anna Petelenz, Emil Jeansson, and the faculty of Mathematics and Natural Sciences, University of Bergen for financial support. Thanks also to the captain and crew working on Kronprins Haakon for the great company and for making the Christmas of 2018 quite memorable. A special thanks to Stein Kaartvedt and Rune Strømme for helping me with the measurements and instruments during the cruise.

I would also like to thank all the friends I have made during my five years at GFI. Thank you for the laughter, the support, and the cooperation to pass calculus, it would not have been the same without you. A special thanks to Vår Dundas, who I shared an office with the last semester. Thank you for enduring with me and inspiring me. Thanks to my family for the endless support. Finally, thank you to my partner, Sondre Kirchhoff Solnørdal, for supporting and encouraging me, making dinner, and keeping our apartment inhabitable for the last months.

Abstract

During the Atlantic meridional transect of R/V Kronprins Haakon from Bergen, Norway to Punta Arenas, Chile, several samples were collected at the sea surface, the chlorophyll maximum depth, and at 200m. The transect covered over 100 degrees of latitude, crossing a range of biomes: subpolar biomes, subtropical biomes, a low latitude upwelling biome, equatorial downwelling biomes, and an equatorial upwelling biome. The samples resulted in data for altogether nine different variables, which are used to characterize the biochemical properties of the different marine environments that were crossed.

The Atlantic thermocline, upwelling, and gyre structures determine the distribution of oxygen and nutrients, and these structures are evident in the temperature and salinity result. In the equatorial regions, the oxygen concentration is low, while nutrient concentration is high, below the strong thermocline due to the upwelling of old waters. Whereas in the subtropics, the oxygen concentration is high, while the nutrient concentration is low due to the converging gyres. In the subpolar region, the oxygen concentration is high due to the low temperatures, and the nutrient concentrations are low due to the deep and weak thermocline. The north subpolar region is the only oxygen undersaturated region due to the deep thermocline and the low temperature.

Further, some the measurements are used to investigate three issues: 1) the effect of the different physical and environmental properties of the different ocean regions on the particulate elemental ratio of autotrophs; 2) changes in surface water CO_2 chemistry between 1991 and 2018; and 3) the physical and environmental properties as drivers of variations in the stable carbon isotope ratio in organic matter ($\delta PO^{13}C$). 1) In the subtropical and tropical regions, the nutrient limitation and temperature are the main controlling factor on the particulate elemental ratio, whereas, in the nutrient-rich Brazil-Malvinas confluence zone, temperature and the presence of diatoms are dominating. 2) Between 1991 and 2018, the fCO_2 has increased mainly due to the increased dissolved inorganic carbon in the Atlantic Ocean, which is attributed to the uptake of anthropogenic CO_2. 3) At the sea surface, the thermodynamic effect is dominating the latitudinal variation of the $\delta PO^{13}C$, while at the chlorophyll maximum depth, it is determined by ϵ_p.

List of Abbreviations

AS	Air-sea gas exchange
BMCZ	Brazil-Malvinas confluence zone
Chl max	The depth of chlorophyll maximum
DIC	Dissolved inorganic carbon
EQ-D	Equatorial downwelling biome
EQ-U	Equatorial upwelling biome
GF/F	Glass microfiber filter
IQR	Interquartile range
IRMS	Isotope ratio mass spectrometer
LL-U	Low latitude upwelling biome
PC	Polycarbonate filter
SP	Subpolar biome
ST-PS	Permanently stratified subtropical biome
ST-SS	Seasonally stratified subtropical biome
SST	Sea surface temperature
SSS	Sea surface salinity
TA	Total alkalinity

Contents

Chapter 1

Introduction

The atmospheric CO_2 level has increased from approximately 277 to 415 ppm since the industrial revolution, where the main contributors are fossil fuel burning and land-use change. This level of change over the last 250 years may change the earth's climate system more than the previous 20 000 years (Heinze et al., 2015). However, had there not been for the ocean and biosphere CO_2 uptake, the CO_2 levels would have been around 500 ppm. They are each responsible for 25% of the anthropogenic CO_2 uptake annually, making the ocean one of the largest CO_2 sinks in the earth system and, consequently, one of the largest mitigators against global warming (Quéré et al., 2018). However, recent studies suggest that oceanic CO_2 uptake may decrease in the future; therefore, studying the marine carbon cycle is of great importance.

The uptake and transport of CO_2 are mainly controlled by the air-sea gas exchange and the biological pump, and both may change due to global warming. Heating the upper layer of the ocean will alter the marine CO_2 air-sea exchange because of 1) decreased CO_2 solubility and 2) stronger stratification. 1) The solubility of CO_2 in seawater decreases with increasing temperature, which consequently may decrease the CO_2 uptake in the future. 2) The effect of a stronger stratification may both increase and decrease the ocean CO_2 sink. If the ocean stratification increases, it will reduce the mixing between the sea surface and deeper layers. This will increase the CO_2 concentration at the sea surface and lower the ocean's ability to take up CO_2 (Maier-Reimer and Hasselmann, 1987; Sarmiento et al., 1998). However, increased stratification will also improve the storage of deep ocean CO_2, preventing CO_2 outgassing. Increased stratification may also affect the biological pump (Ödalen et al., 2018). The biological pump is the assimilation of CO_2 by photosynthesizing organisms, which ultimately will be transported to the deep sea when the organisms die and sink. The biological pump creates a vertical CO_2 gradient that increases the ocean's ability to dissolve CO_2. Had there not been for this vertical gradient, the atmospheric CO_2 content would have been 50% higher (Ito and Follows, 2005; Sarmiento and Gruber, 2006). If global warming increases the ocean stratification, it may hinder the supply of essential nutrients to the sea surface and ultimately decrease the primary production rate (Laufkotter et al., 2015). However, it may also increase the efficiency of the biological pump, which means that

the uptake and transport of CO_2 will increase compared to essential nutrients.

Understanding the factors affecting the primary producers is not solitary important because of the CO_2 drawdown, but also because they make up the basis for the entire marine food web. Consequently, an alteration of the primary production could affect the whole ocean biodiversity. Because of global warming and anthropogenic influence (e.g., fossil fuel bringing and nutrient supply from agriculture), the marine environment is undergoing rapid change, which alters the distribution and cycle of essential nutrients used during photosynthesis (Tuerena et al., 2019). These cycles can be studied through 1) the ratio of the particulate nutrients in the autotroph and 2) the composition of stable isotopes the nutrients are made up of. 1) The ratio between particulate nutrients in autotrophs may, among other things, reflect the nutrient supply in the different ocean regions. 2) Isotopes are versions of the same element with different atomic mass, which gives them slightly different properties. This difference creates discrimination between the isotopes during different processes and provides a measurable difference in the ratio between the isotopes. Consequently, the ratio can indicate what processes are dominating in different ocean regions.

The important task of studying the highly interconnected biochemical cycles in the ocean requires observations of both spatial and temporal variations. It was, therefore, an excellent opportunity to be able to go on a research cruise with R/V Kronprins Haakon during the first leg of the Southern Ocean cruise 2018/2019, from Bergen, Norway, to Punta Arenas, Chile, to collect biochemical data. The transect covered over 100 degrees of latitude crossing a range of ocean regions: sub-polar, subtropical, upwelling and downwelling regions, and coastal upwelling regions. Eight different types of water samples were collected in the upper 200 m, and three different underway measuring systems were installed, which resulted in data for a total of nine different variables: 1) dissolved oxygen, 2) dissolved inorganic carbon, 3) total alkalinity, 4) inorganic carbon isotopes, 5) inorganic nutrients, 6) pico- and nanoplankton abundance, 7) particulate nutrients, 8) particulate organic carbon and nitrogen isotopes and 9) fCO_2, in addition to temperature and salinity. A O_2/Ar instrument, which can be used to infer net primary production, was also included, but malfunctioned and will not be included in the thesis.

This thesis aims to get an overview of the biochemical condition of the Atlantic Ocean by using the observations collected on the research cruise. 1) The methods used to conduct and measure the samples will be presented in section 3. 2) An overview of the environmental conditions of the Atlantic Ocean will be investigated in section 4. 3) In section, 5 the following three aspects will be addressed: variability of the carbon-nitrogen-phosphate ("Redfield") ratios in organic matter; time changes in the surface ocean CO_2 fugacity; and finally, the variability of the organic matter stable carbon isotopic composition.

Chapter 2

Theoretical background

2.1 Hydrographical Regimes and Biomes in the Atlantic Ocean

Wind-driven gyres and tropical circulations dominate the surface of the Atlantic Ocean. There is a cyclonic subpolar and an anticyclonic subtropical gyre in the North Atlantic Ocean, an anticyclonic subtropical gyre in the South Atlantic Ocean, and a tropical circulation at the equator (figure 2.1) (Talley and Pickard, 2011). These ocean structures, including the wind patterns and the mixed layer depths leads to spatial differences in the supply of nutrients to the sea surface of the Atlantic Ocean. The nutrient supply creates different environments in the ocean that has a major impact on the organisms living there, and these environments are known as biographical provinces, or biomes. During the research cruise, several different biomes were crossed (figure 2.2) (Longhurst, 1995, 2007). The first part of the cruise followed the eastern side of the North Atlantic subpolar gyre (figure 2.2). This area is a subpolar biome (SP), which is nutrient-rich as there is both a deep wintertime mixing and a diverging subpolar gyre. However, as the ship sailed through the North Sea and English Channel and not in the open subpolar gyre, coastal influences dominate. Further, the vessel crossed the eastern boundary of the North Atlantic subtropical gyre. The gyre is divided in to seasonally stratified biome (ST-SS) and a permanently stratified biome (ST-PS) (figure 2.2). The seasonally stratified biome is on the northern part of the gyre, where the mixed layer is deep during winter and shallow during summer. This creates a seasonal difference in nutrient supply, that is, nutrient-rich during winter, and nutrient-depleted during summer. The permanently stratified biome is on the southern part of the gyre, where the mixed layer is shallow all year. This causes a low supply of nutrients regardless of the season, and is defined as an oligotrophic area. Further, the vessel crossed the costal upwelling off the north coast of Africa and crossed from the eastern to the western boundary of the Atlantic Ocean through the tropical circulation in the equatorial currents. This area is divided in to a low latitude upwelling biome (LL-U), an equatorial downwelling biome (EQ-D),

and an equatorial upwelling biome (EQU) (figure 2.2). In both the low latitude upwelling biome and the equatorial upwelling biome there is a high supply of nutrients to the sea surface, while the equatorial downwelling is nutrient depleted. At the western side of the South Atlantic, the vessel sailed southward along the western boundary edge of the subtropical gyre in the Brazilian current. This area is in the permanently stratified biome (ST-PS), on the equatorial side of the converging subtropical gyre (figure 2.1 and 2.2). As there is convergence, and no deep mixing during winter, the supply of nutrients is low all year round (Talley and Pickard, 2011; Sarmiento and Gruber, 2006). Finally, at the end of the research cruise, the vessel entered the Brazil-Malvinas confluence zone (BMCZ). This is at the tip of South America in a subpolar biome (SP) (figure 2.2). Here the Antarctic circumpolar water enters the Atlantic Ocean with the Malvinas current and meets the Brazil current. The mixing of the two water masses, and in particular the nutrient rich Malvinas current, creates a unique and highly productive area (Olguín Salinas et al., 2015).

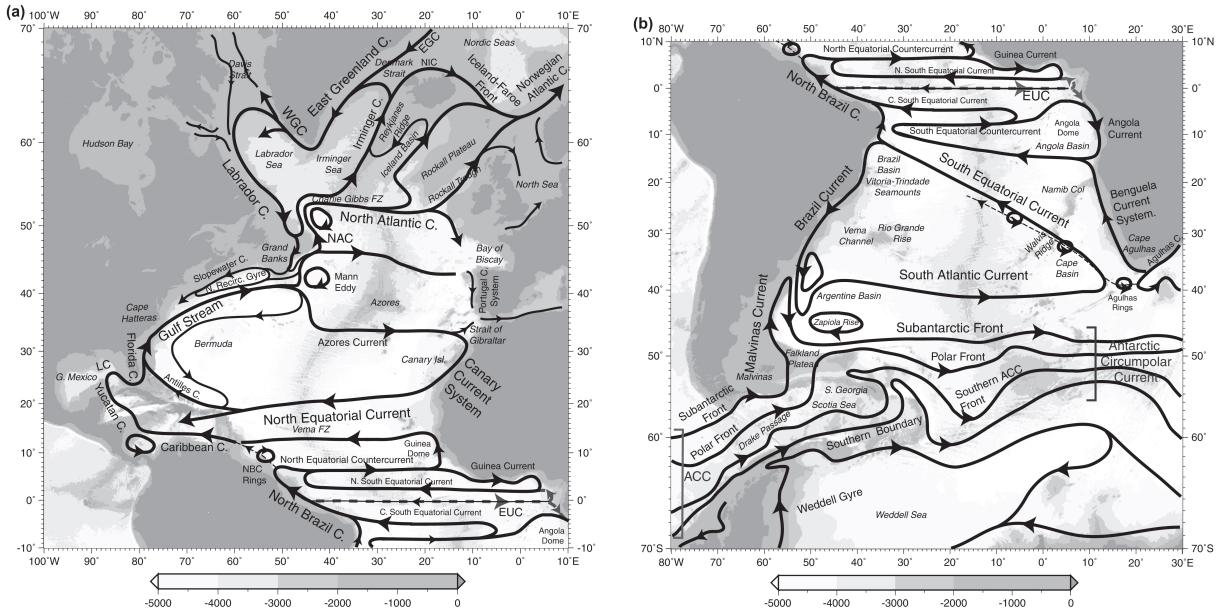

Figure 2.1: The surface circulation of a) the North Atlantic Ocean and b) the South Atlantic Ocean (Talley and Pickard, 2011).

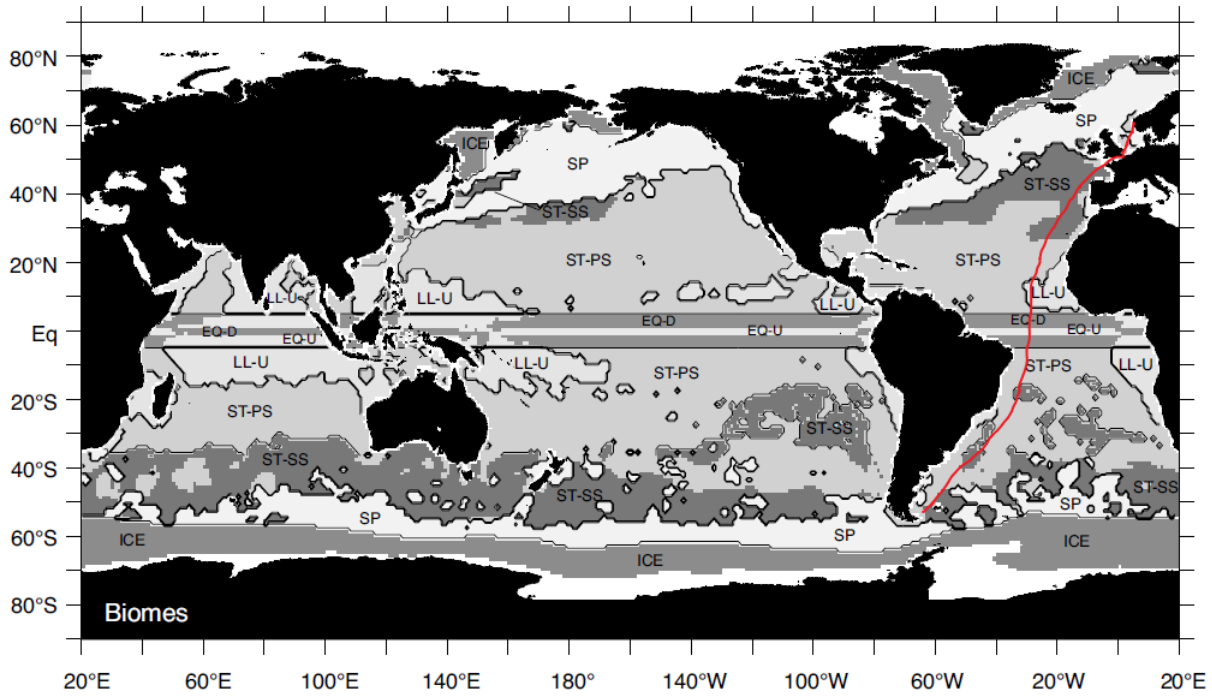

Figure 2.2: Biomes of the global ocean and the approximate route of the research cruise (red line). The symbols are as follows: Eq-D and Eq-U are the equatorially influenced biome split into downwelling and upwelling regions, ST-PS and ST-SS are the subtropics separated into a permanently stratified and seasonally stratified biome, LL-U is the low-latitude upwelling biome, SP is the subpolar biome and Ice is the marginal sea ice biome (Sarmiento and Gruber, 2006).

2.2 Primary Production and the Redfield Ratio

Phytoplankton are the main primary producers in the ocean, and their production varies with light and nutrient supply, mainly. The supply of light depends on the amount of sunlight that reach the ocean surface, and the depth to which it penetrates. The depth to which photosynthesis is possible is called the euphotic depth and is around 100 m in the open ocean, but can be as shallow as 5 m in very turbid waters (Sarmiento and Gruber, 2006). For nutrients, primary producers need both macronutrients (e.g. nitrate (NO_3^-), phosphate (PO_4^{3-}) and CO_2) and micronutrients (e.g. iron (Fe)). As photosynthesis only occurs in the euphotic zone, this is generally nutrient-depleted. The deep ocean on the other hand, is nutrient-rich because the organic matter that sink out of the upper ocean is remineralized there (bacteria degrading organic matter to inorganic nutrients). The supply of nutrients to the sea surface differ between the hydrographical regimes in the ocean (explained in section 2.1) (Sathyendranath and Platt, 2001).

Although phytoplankton comprises a vast amount of different groups, they all have in common that they are autotrophic (using photosynthesis to gain energy). Therefore, primary producers in the ocean are, with just a very few exceptions, made up of the same set of elements (mainly H, C, O, N, and P) as a result of photosynthesis:

$$106\,CO_2 + 16\,HNO_3 + H_3PO_4 + 78\,H_2O + energy \rightleftharpoons C_{106}H_{175}O_{42}N_{16}P + 150\,O_2 \tag{2.1}$$

Because of the stoichiometry of this reaction, the ratio between the elements is approximately constant in the deep ocean (Tyrrell, 2001). A.C. Redfield was the first to discover this, and it is therefore called "the Redfield ratio" and is on average: C:N:P:O_2 = 106:16:1:-145 (Martiny et al., 2013). However, several later observations have shown that the elemental ratio is not the same as the Redfield ratio throughout the global ocean (Tyrrell, 2001). This variation has a clear latitudinal trend where the observed ratios is 195:28:1 in warm nutrient-depleted subtropical gyres, 137:18:1 in warm nutrient-rich upwelling regions in the tropics and 78:13:1 in cold nutrient-rich high latitude regions (Martiny et al., 2013). The elemental ratio of the primary produces will ultimately affect organisms of higher trophic levels. Zooplankton (and other species feeding on phytoplankton) prefer a phytoplankton with a low C:P(N) ratio, as they too depend on these macronutrients. Therefore, the phytoplankton in subtropical regions are of low quality. However, a higher C:P(N) means that the phytoplankton fixes more CO_2 compared to nutrient, and indicates a more efficient biological pump in subtropical regions.

There are several different hypotheses as to what is causing this variability. The ones investigated in this thesis are: 1) the nutrient supply hypothesis, 2) the translational-compensation hypothesis, and 3) the allometric diversity hypothesis (Garcia et al., 2018).

1) The nutrient supply hypothesis is based on the idea that the particulate elemental ratio depends on the nutrient availability of the environment. All phytoplankton groups have a given degree of plasticity for the required nutrient, which means that the elemental ratio may reflect the nutrient concentration. In particular, in the case of phosphate limitation, the C:P ratio is high in response (Garcia et al., 2018).

2) The translational-compensation hypothesis is based on the idea that there is a positive relationship between temperature and C:P and N:P caused by the amount of ribosomes. Ribosomes are molecules in cells that synthesize protein. This relationship arises because there is a lower concentration of P-rich ribosomes at higher temperatures, because the ribosomal translation (the production of proteins) efficiency increases with temperature (Garcia et al., 2018). For simplicity, the hypothesis will be referred to as "the temperature hypothesis" from here on.

3) The allometric diversity hypothesis is based on how the characteristics of different plankton groups change because of their different growth strategies (allometry). In this case, the C(N):P vary between different phytoplankton groups. Fast-growing cells have a lower C(N):P ratio because of larger investments in the P-rich ribosomes, and because fast-growing cells need more protein, they have more ribosomes. This higher need for phosphate means that larger groups like diatoms have a lower N:P and C:P than smaller groups such as marine cyanobacteria (for example, synechoccus) (Martiny et al., 2013; Garcia et al., 2018).

2.3 Inorganic Carbon Chemistry

The inorganic carbon chemistry of the ocean is described by four variables: dissolved inorganic carbon (DIC), total alkalinity (TA), CO_2 partial pressure (pCO_2), and pH. By only knowing two of these four variables it is possible to calculate the carbon chemistry of the ocean. The inorganic carbon chemistry comprises of only a few components (also known as carbon species), and is governed by the following three equilibrium reactions:

$$CO_{2(gas)} + H_2O \rightleftharpoons H_2CO_3^* \tag{2.2}$$

$$H_2CO_3^* \rightleftharpoons H^+ + HCO_3^- \tag{2.3}$$

$$HCO_3^- \rightleftharpoons H^+ + CO_3^{2-} \tag{2.4}$$

Where $[H_2CO_3^*] = [H_2CO_3] + CO_{2(aq)}$ (Sarmiento and Gruber, 2006). DIC and TA are a measure of concentrations. DIC is the sum of the carbon species in these equilibrium reactions:

$$DIC = [H_2CO_3^*] + [HCO_3^-] + [CO_3^{2-}] \tag{2.5}$$

Biology and temperature are the main controllers of DIC in sea surface, as the carbon concentrations are affected by photosynthesis, respiration and air-sea gas exchange (figure 2.3). TA is defined as a measure of bases over acids, or proton acceptors over proton donors:

$$TA = [HCO_3^-] + 2\,[CO_3^{2-}] + [OH^-] - [H^+] + [B(OH)_4^-] \tag{2.6}$$

Including other minor bases, such as, PO_4^{3-} and Si, which also affects the TA (Sarmiento and Gruber, 2006). TA is mainly controlled by salinity, as TA is made up of ions (and salinity is a measure of ions in the ocean). TA is also affected by biology through photosynthesis, respiration and calcification (figure 2.3). However, the effect of primary production and respiration is small compared to salinity, and the effect of calcification is small in the sea surface (Takahashi, 2002; Sarmiento and Gruber, 2006).

pCO_2 and pH is a measure of activity. pCO_2 (fCO_2) is defined as the partial pressure (fugacity) of CO_2 in 100% saturated air equilibrated with the seawater. The fugacity is the partial pressure that has been corrected for non-ideality of the gas (Pierrot et al., 2009). The pCO_2 difference between the atmosphere and the ocean controls the transfer of CO_2 in and out of the ocean (Takahashi, 2002; Pierrot et al., 2009). The atmospheric pCO_2 is relatively uniform, while open ocean pCO_2 at the sea surface varies between 150 ppm and 550 ppm because the ocean is much less effectively mixed than the atmosphere. Consequently, the variations of ocean pCO_2 control patterns of

CO_2 in/outgassing in the ocean. pH is the measure of H^+ activity, which defines the acidity of the ocean. Because CO_2 acts as an acid when it is dissolved, it changes the pH of the ocean (figure 2.3) (Zeebe and Wolf-Gladrow, 2001). Due to increased uptake of CO_2, the pH has decreased from 8.2 to 8.1 since the industrial revolution (Laufkötter et al., 2013).

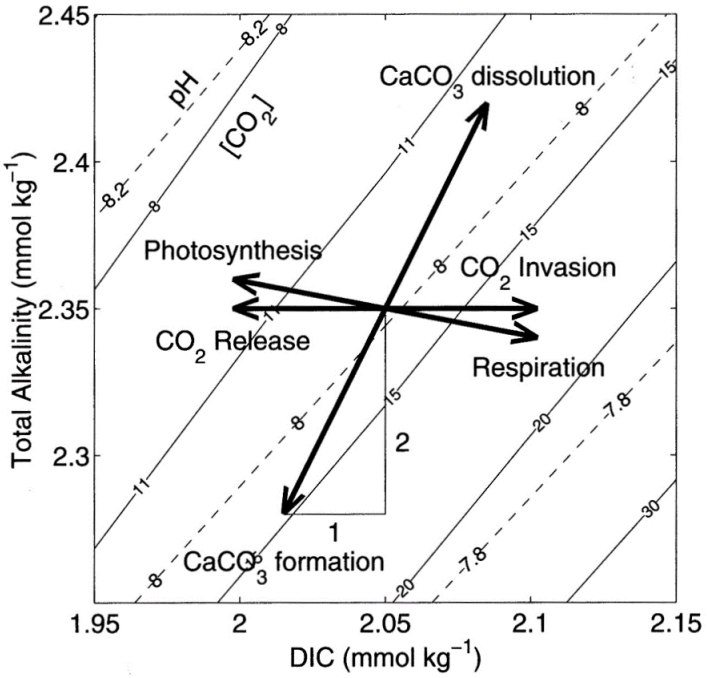

Figure 2.3: The effect of various prosesses on DIC and TA (arrows). The solid black lines are constant CO_2 concentrations and the dashed lines are constant pH (Zeebe and Wolf-Gladrow, 2001)

2.4 Stable Carbon and Nitrogen Isotopes

Both carbon and nitrogen have two stable isotopes, for carbon: ^{13}C and ^{12}C, and for nitrogen: ^{14}N and ^{15}N, where 12, 13, 14 and 15 are the atomic masses. For both, the lighter isotope is most abundant (Sigman and Fripiat, 2019; Nier, 1950). The ratio between the stable isotope are given as $\delta^{13}C(‰)$ and $\delta^{15}N$ (‰), which is the per mil deviation of $^{13}C/^{12}C$ or $^{15}N/^{14}N$ ratio relative to the given standard ratios: ratio Vienna Pee Dee ($^{13}C/^{12}C$ =0.011179) and atmospheric nitrogen ($^{15}N/^{14}N$= 0.003677)(Ohkouchi et al., 2015):

$$\delta(‰) = 10^3 \frac{R_{sample}}{R_{standard}} - 1 \tag{2.7}$$

Where R is $^{13}C/^{12}C$ or $^{15}N/^{14}N$ ratio of the sample or the standard. If a sample contains less ^{15}N or ^{13}C than the standard, δ is negative.

Isotopic fractionation

The ratio of the stable isotopes of carbon and nitrate may change during physical and biological processes. This is known as isotopic fractionation. Consequently, the difference in the isotope ratio caused by isotopic fractionation during various processes provides a way to study the ocean's biogeochemical cycles. (Sigman and Fripiat, 2019; Ohkouchi et al., 2015). The isotopic composition of the reactant and the product gives the magnitude of isotopic fractionation (the 'isotopic fractionation' ϵ) by the following equation:

$$\epsilon = 10^3(\frac{R_r}{R_p} - 1) \tag{2.8}$$

where r and p is the reactant and product. $\epsilon = 0$ is no fractionation, $\epsilon > 0$ is heavier in product and $\epsilon < 0$ is heavier in reactant (Sigman and Fripiat, 2019).

There are two types of isotopic fractionation: 1) equilibrium and 2) kinetic. 1) Equilibrium fractionation occurs in a reversible reaction where a chemical equilibrium is attained, such as in the carbon chemistry reaction (eqs. 2.2, 2.3 and 2.4). The fractionation occurs to ensure the distribution of isotopes of a system requires the least possible energy. Therefore, heavier isotopes equilibrate into compounds or phases that are most stably bound. As it takes a stronger bond to hold a heavy isotope, changes in the energy (difference in vibrational energy), causes an isotopic fractionation. The vibrational energy is dependent on temperature, which means that equilibrium fractionation is too. 2) Kinetic fractionation occurs in irreversible reactions or when the product of the reaction is removed from the system, such as evaporation, diffusion, and biological reactions. The fractionation occurs because heavier isotopes move slower than lighter ones, for example, diffuses slower (Ohkouchi et al., 2015).

Photosynthesis is an example of kinetic fractionation, when the lighter carbon isotope is preferred as it require less energy to assimilate (Ohkouchi et al., 2015). This kinetic fractionation removes the product (organic carbon) from the system (inorganic carbon). In general terms, such a process that removes the lighter isotope from the system and leaves the product enriched in heavy isotopes is known as a Rayleigh process. If the Rayleigh process continues, it will eventually increase the isotopic ratio of the organisms (figure 2.4). Because, if the lighter isotope is continuously removed and transported out of the system, the organism will eventually assimilate heavier isotopes (Ohkouchi et al., 2015). This effect is most evident for nitrogen as the supply is limited, while for carbon, which is abundant in the ocean, the effect is only evident during very intense blooms (Becker, 2016).

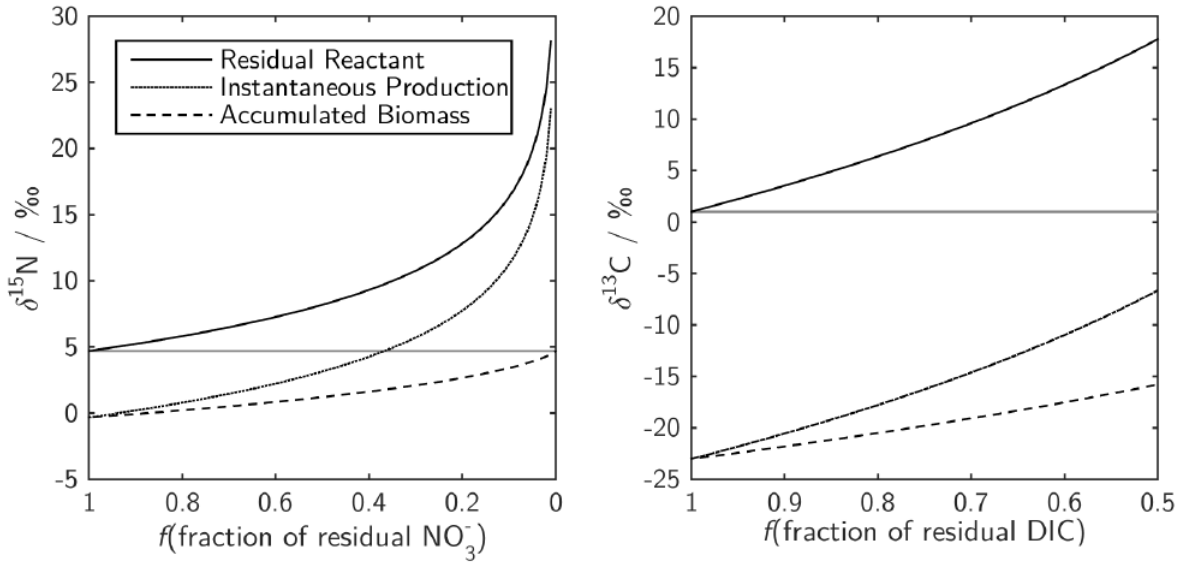

Figure 2.4: Rayleigh process during primary production for nitrate (left hand side) and DIC (right hand side). The isotopic fractionation between nitrogen and organic nitrogen is ϵ=-5‰and between DIC and organic carbon is ϵ=-24‰(Becker, 2016).

Isotopic fractionation of carbon and nitrogen in the marine system

As the cycles of carbon and nitrogen the ocean are different, the processes causing dynamic fractionations are too. For carbon, there are mainly three factors affecting the isotopic ratio: biology, thermodynamic effect, and the ^{13}C Suess effect (the intrusion of anthropogenic CO_2 enriched in ^{12}C). The effect of other processes, like $CaCO_2$ formation/dissolution, are small in comparison.

Biology affects the isotopic composition as photosynthesizing and decomposing organisms prefer lighter ^{12}C over ^{13}C (O'Leary, 1981). Photosynthesis in the ocean surface removes ^{12}C and leaves the remaining DIC enriched in ^{13}C, and at depth the ^{12}C is released through remineralization. This results in an ocean where inorganic δ^{13}C decrease with depth (Zeebe and Wolf-Gladrow, 2001). The organic δ^{13}C of photosynthesizing organisms ranges between -38‰to -10‰(figure 2.6) depending on the fractionation during photosynthesis (ϵ_p):

$$\epsilon_p = \delta \mathrm{PO}^{13}\mathrm{C} - \delta_{13}\mathrm{CO}_{2(\mathrm{aq})} \tag{2.9}$$

The ϵ_p varies with the environmental conditions and the cell physiology of the given organism. The organic δ^{13}C has been shown to be inversely related to the $CO_{2(aq)}$ concentration, meaning that areas with high CO_2 concentration has a low organic matter δ^{13}C. This is because high $CO_{2(aq)}$ concentration allows the organisms to discriminate more against ^{13}C (Tuerena et al., 2019). δ^{13}C is also affected by growth rates, where smaller phytoplankton

tends to have a lower δ^{13}C compared to larger and fast-growing plankton, such as diatoms (Tuerena et al., 2019). This is because large and fast-growing plankton are not as selective when assimilating CO_2 as smaller slower growing plankton.

Thermodynamic fractionation is important for processes: 1) air-sea gas exchange and 2) DIC to $CO_{2(aq)}$. 1) The fractionation occurring during air-sea gas exchange of CO_2 is a highly temperature dependent process. The fractionation results in higher δ^{13}C in cold waters (high latitudes), and low δ^{13}C in warm waters (low latitudes). The temperature dependence of the fractionation, as determined using Eq. 2.10 (Zhang et al., 1995), shown in figure 2.5:

$$\epsilon_{(DIC-^{13}CO_{2(g)})} = (0.014 \pm 0.01)\,T(^{\circ}C)\,f_{CO_3} - (0.105 \pm 0.002)\,T(^{\circ}C) + (10.53 \pm 0.05)‰ \tag{2.10}$$

Where f_{CO_3} is the carbonate fraction assumed to be 0.12 corresponding to a pH of 8.15.

2) The distribution of isotopes in the DIC pool is temperature dependent, where the δ^{13}C of $CO_{2(aq)}$ increases with temperature. This temperature effect may be evident in the δPO^{13}C, by $CO_{2(aq)}$ assimilation during photosynthesis. This will be investigated further in section 5.3.2 by calculating the $\epsilon_{(DIC-CO_{2(aq)})}$ and $\delta^{13}CO_{2(aq)}$. The fractionation $\epsilon_{(DIC-CO_{2(aq)})}$ is calculated using Eq. 2.10 combined with Eq. 2.11 for the fractionation during hydration ($\epsilon_{(CO_{2(aq)}-CO_{2(g)})}$) (figure 2.5) from (Zhang et al., 1995):

$$\epsilon_{(^{13}CO_{2(aq)}-^{13}CO_{2(g)})} = -(0.0049 \pm 0.003)\,T(^{\circ}C) - (1.31 \pm 0.06)‰ \tag{2.11}$$

This combination yields the following fractionation equation between DIC and $CO_{2(aq)}$ (figure 2.5) (Zeebe and Wolf-Gladrow, 2001):

$$\epsilon_{(DIC-^{13}CO_{2(aq)})} = \frac{\epsilon_{(CO_{2(aq)}-CO_{2(g)})} - \epsilon_{(DIC-CO_{2(g)})}}{1 + \epsilon_{(DIC-CO_{2(g)})} \times 10^{-3}} \tag{2.12}$$

$\epsilon_{(DIC-^{13}CO_{2(aq)})}$ and the measured δDI^{13}C is then used to calculate $\delta^{13}CO_{2(aq)}$ (Zeebe and Wolf-Gladrow, 2001):

$$\delta^{13}CO_{2(aq)} = \delta DI^{13}C + \epsilon(DIC \rightarrow {}^{13}CO_{2(aq)}) \tag{2.13}$$

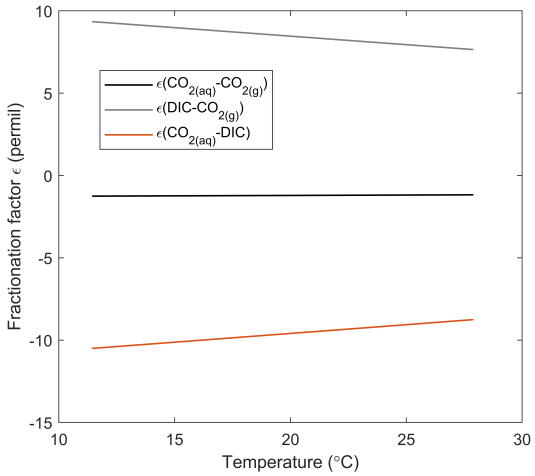

Figure 2.5: The ^{13}C fractionations with temperature between: dissolved and gasous CO_2 ($\epsilon_{(CO_{2(aq)}-CO_{2(g)})}$) (black line), DIC in sea water and CO_2 in air ($\epsilon_{(DIC-CO_{2(g)})}$) gray line and dissolved CO_2 and DIC ($\epsilon_{(DIC-CO_{2(aq)})}$) (red line)

.

The ^{13}C Suess effect is a consequence of the intrusion of anthropogenic CO_2 from burning of fossil. δ^{13}C of fossil fuel is as low as -28‰ because of its biological origin, and has decreased the atmospheric δ^{13}C from a preindustrial value of -6.3‰to -8‰(Francey et al., 1999). Through the air-sea gas exchange of CO_2, the reduced δ^{13}C affects the upper layers of the ocean in particular (Eide et al., 2017).

The cycle of nitrogen in the ocean is complex, and consequently, there are many processes that alter the isotopic composition of nitrate. Because of this, the cycle is explained in three parts: input, output, and internal cycling.

Reactive nitrogen (nitrogen compounds that can be used during primary production) is added to the ocean by mainly: 1) supply from the continents trough river runoff, and 2) by nitrogen fixation. 1) Large amounts of reactive nitrogen are being supplied to the ocean by rivers because of fertilizing. Chemically synthesized fertilizer usually has a δ^{15}N between -6‰to 7‰ (Ohkouchi et al., 2015) (figure 2.4). This supply mainly affects coastal areas. 3) Reactive nitrogen may also be added to the system by specialized organisms that can use nitrogen as a growth substrate, which is called nitrogen fixation. The δ^{15}N of nitrogen fixing organisms is around -2‰to 0‰(figure 2.6) (Sigman and Fripiat, 2019).

Trough denitrification, nitrogen is lost from the ocean — this process occurs when bacteria use nitrate instead of oxygen to remineralize organic matter in oxygen minimum areas. The isotopic fractionation of denitrification is around ~20‰to 30‰(Sigman and Fripiat, 2019).

The internal cycling of nitrogen is made up of nitrogen assimilation by photosynthesis and remineralization. During both processes, lighter ^{14}N is preferred over ^{15}N, as for carbon. Therefore, δ^{15}N of organic matter usu-

ally increases with depth. The fractionation during photosynthesis is ~-5‰, however, the δ^{15}N for marine algae is ~+5‰(figure 2.6). This is due to the stronger Ryleigh effect in the euphotic zone (Sigman and Fripiat, 2019; Ohkouchi et al., 2015)

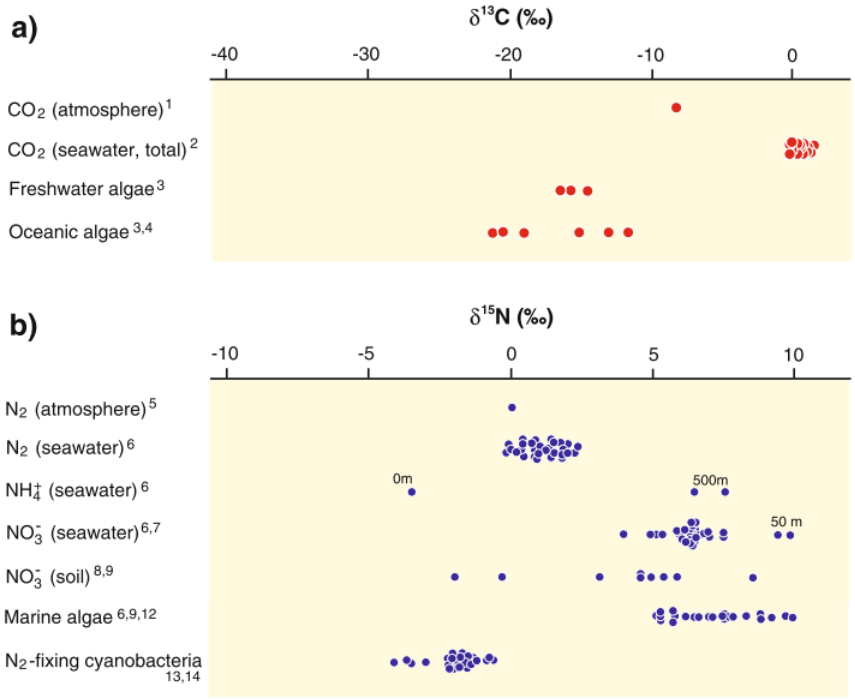

Figure 2.6: Isotopic compositions of a) carbon and b) nitrogen in their various forms in sea water (Ohkouchi et al., 2015).

Chapter 3

Methods

3.1 Observations

Underway instruments and water samples were used to measure ten different biogeochemical variables during the cruise, and the method for each is described in this section. Whenever the vessel was inside the 200-mile zone (Exclusive Economical Zone) surface water samples were collected from the water intake at 4 m depth in the clean water lab placed in the machine room twice a day. Only chemical samples (dissolved O_2, DIC and TA, nutrients, and inorganic isotopes) were collected at these stations, as the water inlet pump destroys biological material. Otherwise, one CTD station was conducted each day, with water samples collected at the surface (~5 m), the depth of chlorophyll maximum, 200 m, and occasionally at 1500 m, for a total of 24 stations. The location of the stations is displayed in figure 3.1. As sampling down to 1500 m was conducted only three times, they are not presented here. At each sampling depth, two 10 L niskins were filled, and the water samples were collected in order of which is most sensitive to contact with air: 1) dissolved O_2, 2) DIC and TA, 3) inorganic carbon isotopes, 4) inorganic nutrients, 5) flowcytometry and 6) filtration samples (for organic carbon and nitrogen isotopes and for particulate elements).

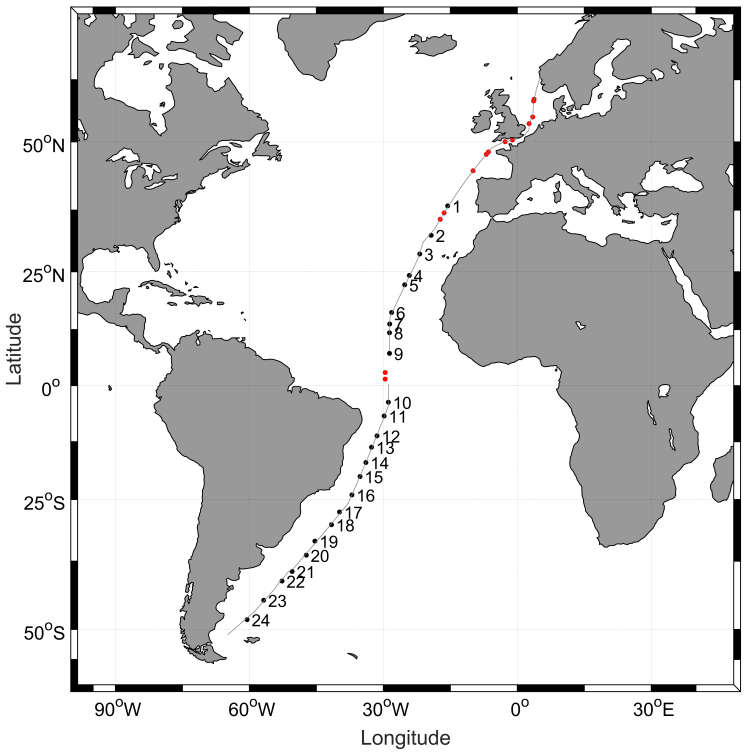

Figure 3.1: Map of transect with sample stations. Red dots are the water inlet stations, the numbered black dots are the CTD stations and the gray line is from the automated measuring system.

3.1.1 Hydrographic Data

A CTD and a thermosalinograph were used to obtain hydrographic measurements (temperature, salinity, and depth (calculated by pressure)) (SBE, 2016, 2015a). Oxygen and fluorescence sensors were attached to the CTD, where the latter was used to determine the chlorophyll max depth. Water samples were collected from niskins for salinity calibration of the CTD measurements.

Table 3.1: Range and accuracy for the SBE911 plus CTD system and the SBE 21 thermosalinogaph system (SBE, 2015b,a)

Instrument	Parameter	Range	Accuracy
CTD	Temperature	-5 to 34 (°C)	±0.001 (°C)
	Conductivity	0-7 S/m	±0.0003 S/m
	Pressure	0-10 340 dbar	±0.015% of range
Thermosalinograph	Temperature	-5 to 34 (°C)	±0.01 (°C)
	Conductivity	0-7 S/m	±0.001 S/m

3.1.2 Surface Underway fCO_2

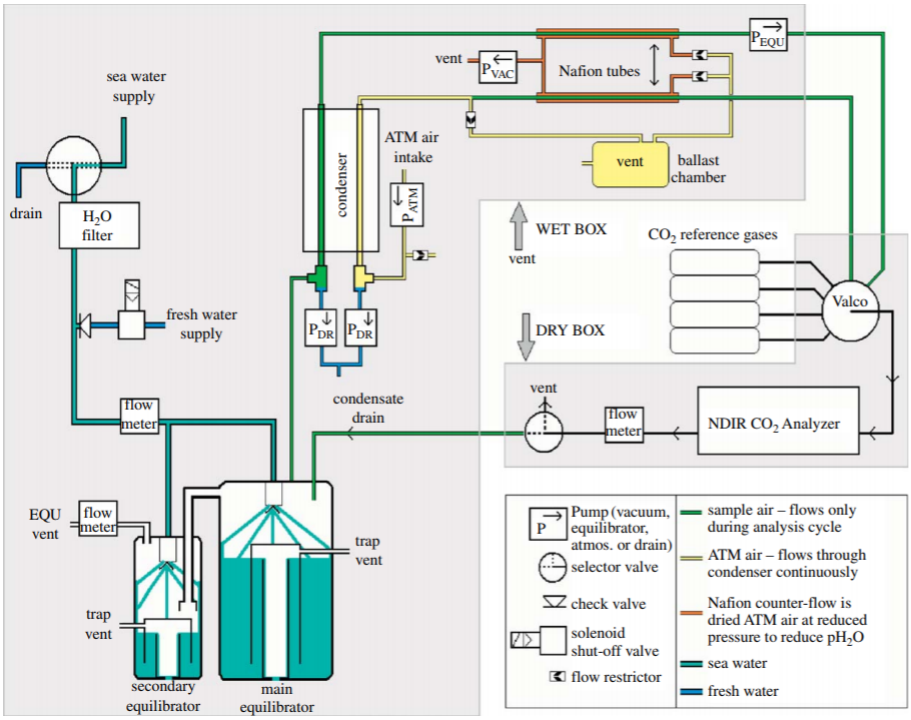

Figure 3.2: Schematic drawing of the underway pCO_2 system (Pierrot et al., 2009).

An automated fCO_2 system was used to measure fCO_2 in the clean water lab, manufactured by General Oceanics according to the design presented in (Pierrot et al., 2009) (Figure 3.2). The system consists of three parts: a wet box, a dry box, and a deck box. Seawater circulates through the wet box continuously at 1.5-2 L/min. The flow enters the equilibrator (a chamber containing seawater and headspace air) through a spiral nozzle as a spray of seawater (Figure 3.2). According to Henry's law, given a large amount of water compared to air, the pressure of a gas in the air is proportional to the concentration of the dissolved gas in the liquid (Pierrot et al., 2009). Hence, the seawater concentration of CO_2 in the equilibrator controls the fCO_2 in the headspace air. The gas circulates to the dry box where the mole fraction of CO_2 (xCO_2) content is measured using a non-dispersive infrared analyzer (NDIR CO_2 Analyser by Licor (Port, 2019)). Standard gasses (one zero gas and tree calibrated gasses ranging from 200-430 ppm) and atmospheric air were measured every 2.5-3 h. The standard gasses are used to correct the analyser response as it tends to drift over time. The accuracy for the system is 0.2 μatm for atmospheric measurements and 2 μatm for seawater measurements (Pierrot et al., 2009).

The measurements were then used to calculate fCO_2 using the following steps: 1) flagging data according to quality, 2) calibrating the data using the standard gas measurements, 3) calculating fCO_2, and 4) removing data according to flags. For 1), the data were flagged into the following categories: good, questionable, and bad using the temperature, salinity, equilibrator gas flow, and pressure measurements. The values were flagged as questionable if the temperature difference between the equilibrator and the thermosalinograph was >10 °C, or the equilibrator gas

flow was <40 ml/min. The values were flagged as bad if the thermosalinograph temperature values were outside of a -2 to 38 °C range, the salinity values were outside of a 2 to 40 psu range, the equilibrator gas flow was <20 ml/min, or if the atmospheric pressure was outside the range 800 to 1150 mbar. For 2), as the analyser drift over time, the xCO_2 data were corrected using the standard gas measurements. The measured standard gas values were interpolated over the measured xCO_2, and used to create a correlation regression, which is used to correct the measured values. For 3), fCO_2 was calculated from the measured xCO_2 as follows (Pierrot et al., 2009):

$$pCO_2 = xCO_2^{dry}(P_{equ} - pH_2O) \tag{3.1}$$

Where xCO_2 is the CO_2 mole fraction, P_{equ} is the pressure inside the equilibrator, and pH_2O is the water vapor pressure at the temperature and salinity of the equilibrator.

$$fCO_2 = pCO_2 e^{(p_{tot}\frac{B+2\delta}{RT})} \tag{3.2}$$

Where T is the equilibrator temperature (K), P_{tot} is the atmospheric pressure (atm), R = 82.0578 cm^3 atm mol^{-1} K^{-1}, and B and δ are virial coefficients for CO_2 (Weiss, 1974). The intake temperature was measured by the thermosalinograph and the temperature by the fCO_2 system to an accuracy of 0.05 °C. To correct for temperature difference between the two temperatures (the equilibrator temperature and the intake temperature) the empirical temperature dependence by Takahashi et al. (1993) (Takahashi et al., 1993) was used:

$$fCO_2^{insitu} = fCO_2^{eq} e^{0.423(t_{insitu} - t_{eq})} \tag{3.3}$$

for 4), using the flagging done in step i) and manually flagging, calculated fCO_2 in questionable or bad positions was removed.

The fCO_2 data was then used to calculate the rest of the carbon system. First, TA was calculated using temperature and salinity data by equations given in Lee et al. (2006). Then, the latter of the carbon system were calculated using CO_2sys. CO_2sys is a MatLab script developed by Lewis and Wallace (1998) for carbon system calculations. The carbon system is made up of DIC, TA, pH, and pCO2 or fCO2, and by knowing only two of these, including temperature and salinity, it is possible to calculate the rest. DIC and pH were calculated using the measured fCO_2, calculated TA, temperature, and salinity from the themosalinograph and measured nutrients (PO_4^{3-} and Si). PO_4^{3-} and Si effects the TA value and can therefore include in the program. Other values used were: K_1 and K_2 dissociation constants from Lueker et al. (2000), the pH scale was given in total scale, the KSO4 dissociation constants from Dickson (1990) with borate-to-salinity ratio from Uppström (1974), and temp in and out were the same (temperature from water inlet), to get insitu data (Lewis and Wallace, 1998).

3.1.3 Dissolved Oxygen

Dissolved oxygen was measured using an optode sensor placed in the clean water lab, an oxygen sensor attached to the CTD rosette, and by Winkler titration. The optode measurements were corrected for salt content, and bad data were removed using the same flagging as for fCO_2, including additional manual flagging of bad data.

Table 3.2: Accuracy and precision for the oxygen optode, oxygen sensor on CTD, and Winkler titration (Aandera, 2018; SBE, 2013; Langdon, 1991)

Instrument	Accuracy	Precision
Oxygen optode	± 2 (μmol kg^{-1})	
Oxygen sensor on CTD	± 3 (μmol kg^{-1})	
Winkler titration	± 0.3 (μmol kg^{-1})	± 0.15 (μmol kg^{-1})

Winkler titration was used to measure the oxygen content of water samples from both the water inlet and the CTD. Two samples were taken from each depth in 250 ml bottles and stored at 4 °C for a maximum of three days before analysing. Before filling the bottle, the tube from the niskin was rinsed, and bubbles were removed. The tube was lowered to the bottom of the bottle and filled for as long as it took to fill the bottle three times. These procedures were followed to ensure as little contact with air as possible. The Winkler titration measures oxygen content in water by adding chemicals that react with oxygen to create an acidic solution. The oxygen content is then determined by how much neutralizing substance is needed to neutralize the solution (Markgraf, 2018)

1 ml of manganous chloride ($MnCl_2$) and alkaline sodium hydroxide-sodium iodide solution (NaOH/NaI) were added right after sample was drawn. Manganous hydrocide ($Mn(OH)_2$) precipitates and reacts with O_2 in the sea-water, which will oxidise the manganese ions giving manganese ($MnO(OH)_2$) giving the sample a yellow/brown colour:

$$\begin{aligned} Mn^{2+} + 2OH^- &\rightleftharpoons Mn(OH)_2 \\ 2Mn(OH)_2(S) + O_2(aq) &\rightleftharpoons 2MnO(OH)_2(S) \end{aligned} \tag{3.4}$$

The iondine (from NaI) remains in the water as iodine ions (I^-). When the sample was ready to be measured 1 ml of a sulfuric acid (H_2SO_4) was added to the sample. The acid will cause the manganese ions to oxidise I^- to free iodine (I_2).

$$2MnO(OH)_2 + 4I^- + 8H^+ \rightleftharpoons 2Mn^{2+} + 2I_2 + 6H_2O \tag{3.5}$$

There are two iodine molecules for each mole of O_2 in the sample at this point, and the O_2 content is determined by determining the iodine amount. This amount is determined by titration with sodium thiosulfate ($Na_2S_2O_3^{2-}$) (a neutralizer) with known concentration. The titration is conducted until all iodine ions are exhausted, which is

marked by a color change, the sample turns from yellow/brown to clear (Langdon, 1991).

$$I_3^- + S_2O_3^{2-} \rightleftharpoons 3I^- + S_4O_6^{2-} \tag{3.6}$$

A UV-light radiates trough the sample and is measured by a sensor on the opposite side, which determines when the sample is clear.

To determine the thiosulfate strength, and to increase the precision and accuracy, standards and blanks were measured before the samples. One can in general expect a precision of 1% of the measured values if everything is done correctly (Olsen et al., 2016).

3.1.4 Dissolved Inorganic Carbon and Total Alkalinity

DIC and TA were measured from water samples from the water inlet and CTD niskins. Both were measured from the same sample bottle. Seawater was collected in 250 ml bottles and one drop of (approx. 0.02 ml) $HgCl_2$ was added to prevent any biological activity to affect the sample. One sample was collected at each every depth, with a duplicate at 200 m every third day. Before filling the bottle, the tube from the niskin was rinsed, and bubbles were removed. The tube was lowered to the bottom of the bottle and filled for as long as it took to fill the bottle twice. This procedure ensures as little contact with air as possible, which would otherwise affect the DIC values of the sample. The samples were stored at 4°C during the cruise but were left at room temperature when stored in Chile and during shipment.

DIC was measured first as the DIC value is more vulnerable to contact with air than TA. DIC was measured using a VINDTA 3D system, which uses acidification and coulometric detection. The sample is acidified to convert the DIC to CO_2 gas, which is extracted, and the coulometer determines the amount. The TA was measured using a VINDTA 3C system. The sample is titrated with a weak acid (0.1M HCl) and the titration curve is used to calculate the TA of the sample (Dickson et al., 2007).

Table 3.3: Accuracy and precision for the DIC and TA instruments (Dickson et al., 2007)

Instrument	Parameter	Accuracy	Precision
VINDTA 3D	DIC	± 1.5 (μmol kg^{-1})	± 4 (μmol kg^{-1})
VINDTA 3C	TA	± 3 (μmol kg^{-1})	± 6 (μmol kg^{-1})

3.1.5 Inorganic Carbon Isotopes: δDI^{13}C

δDI^{13}C was measured using water samples followed by mass spectrometric analysis to determine the isotopic ratio of inorganic carbon.

Seawater for δDI^{13}C was collected in 100 ml bottles and added one drop (approx. 0.02 ml) of $HgCl_2$ to prevent biological activity, which would alter the sample's DIC carbon isotope composition. One sample was taken at each depth, with a duplicate at 200 m every third day. The samples were drawn in the same matter as for DIC/TA; to avoid unnecessary contact with air. The samples were stored at 4°C during the cruise but were left at room temperature when stored in Chile and during shipment.

Three replicate measurements of δDI^{13}C were made on each bottle. 1.4 ml of sample was added into three exitainers, which had been preflushed with He and a small volume of acid injected. When the sample is added, the DIC reacts with the acid and converted to CO_2 gas. This gas is injected to the isotope ratio mass spectrometer (Delta V), which determines the stable carbon isotope composition (Fisher, 2013; Corporation, 2005). The IRMS has a precision of $\pm 0.47‰$ for δ^{13}C.

Standards were used to correct for instrument drift. The standards were weighted and put in bottles that were flushed with He and added acid. Four different standards were used: CO8, CM12, NBS18, and NBS19. All samples were analysed in four separate runs with 70 samples and 28 standards in each.

3.1.6 Inorganic Nutrients

Water samples for inorganic nutrient measurements were collected in 60 ml bottles at each depth and added one drop of chloroform (to prevent biological activity in the sample). One sample was taken at each depth, with a duplicate at 200 m every third day. The samples were stored and shipped in a cooled container (4°C). The nutrient content (NO_3^-, PO_4^{3-}, Si, and NO_2) was measured by the Institute of Marine Research, Bergen, Norway, using standard Gas Segmented Continuous Flow Analysis, with a precision of 2% (Gundersen and Lunde, 2015).

3.1.7 Abundance of Pico- and Nanoplankton

Flowcytometry was used to count picoplankton, synechoccus, heterotrophic bacteria, and nanoplankton in the water samples. Picoplankton is the most abundant planktonic group in the marine ecosystem. Picoplankton are small (cell diameter<2μm) and dominate oligotrophic tropical and subtropical regions. Synechoccus is a picocyanobacterial, which is a photosynthesizing prokaryote. It is widespread in the marine environment but differs

from other pico groups as it is most abundant in well-lit and nutrient-rich waters (Luis Otero-Ferrer et al., 2018). Nanoplankton is larger than picoplankton with a cell diameter of 2-20μm. Nanoplanktons are most abundant in nutrient-rich waters, such as coastal upwelling regions (Leblanc et al., 2018)

Seawater for flowcytometry was collected in a 50 ml tube at each depth. 1.8 ml of the seawater from the tube was combined with 38 μl of 25% glutaraldehyde in 2 ml cryovials, which were frozen in liquid nitrogen and stored in a -80°C freezer.

The cell density of pico- and nanoplankton was analysed with an Attune NxT Acoustic Focusing Cytometer, which uses a laser beam to measure the optical properties of the particles in the sample, which is used to determine the plankton composition. The instrument has an accuracy of <1% (Fisher, 2015). For the bacteria measurements, 100 μl of the sample was mixed with 900 μl of Tris-EDTA (TE) and stained with 10 μl of ZYBR Green x100 (a green nucleic acid dye). The samples were counted for 1 min and discriminated based on their green fluorescence and the side scatter. Phytoplankton samples were counted after thawing and the different groups were sorted based on their side scatter and red fluorescence. The measurements separates between sizes: picoplankton and synechoccus are <2 μm, and nanoplankton 1 and 2 are 2-20 μm.

3.1.8 Organic Carbon and Nitrogen Isotopes: δPO^{13}C and δPO^{15}N

δPO^{13}C and δPO^{15}N were determined by filtering seawater, followed by mass spectrometric analysis of the matter left on the filter to determine the isotopic ratios in the particulate organic matter.

25 mm diameter glass microfiber filters (GF/F) were used to filter 500 ml and occasionally 1000 ml of seawater. The filters and containers were baked beforehand to make sure there were no traces of carbon left, as this would otherwise contaminate the results. Three replicates were taken at each depth until station 12 when the amount was reduced to two and stopped at station 20 due to a limited number of containers. The filters were stored at -20°C and shipped back frozen.

Before analyzes, the filters were dried overnight at 50°C and placed in a tin capsule. During each analysis, three different standards (caffeine, N1-USGS24, and N2-sucrose) were run together with the samples. There were in total nine batches with 20 filters and 18 standards in each. Standards are used to correct for instrument drift, and to correct for different weight of the samples.

An isotope ratio mass spectrometer (IRMS) and element analyzer are used to measure the stable carbon and nitrogen isotopes. The instruments measure the relative abundance of isotopes of carbon and nitrogen based on their atomic masses. The instrument has a precision of ±0.12 for δ^{13}C and ±0.47 ‰for δ^{15}N.

3.1.9 Particulate Elements

To measure particulate C, N, Si and others (Na, S, Mg, Ca, Mn, Fe and Zn), two types of filters were used: 47 mm diameter glass microfiber filters (GF/F) for N and C and 47 mm diameter polycarbonate filters (PC) for Si and others (Na, S, Mg, Ca, Mn, Fe and Zn). Two different filters were used because PC filters contain carbon and can affect the carbon result. Three replicates of both filters were taken at each depth, and 1 L of seawater was filtered through each. The filters were rinsed with distilled water to avoid salt crystals forming on the filters and dried for 2-6 h before they were placed in individual containers and stored at room temperature.

The concentration of the various elements in particulate form was measured by XRF (WDXRF), which is based on wavelength dispersive X-ray fluorescence (Paulino et al., 2013). If the concentration of a certain element was below the detection limit (table 3.4), the results were removed from the dataset. The filters that were not rinsed with distilled water (detected by the Na and Cl result) were also removed from the results.

Table 3.4: Detection limit per filter for the relevant elements (Paulino et al., 2013)

Element	C	N	P	Si
PC (μM/filter)	7.8255	0.9440	0.0006	0.0035
GF/F (μM/filter)	0.5920	0.1082	0.0015	0.0030

3.2 Statistical Analysis

To easier compare and explain the data, some variables are separated into five different regions based on the characteristics of the regions given by the temperature and salinity and latitudes of the different biomes (described in section 2.1).

The variables in the different regions were compared using Welch's t-test and Tukey box plot to determine if the properties in the regions significantly differed. Welch's t-test is a modified version of the two-sample student's t-test, which determines if the mean of two sample groups are significantly different. This particular t-test is used when the sample sizes are small (<30) and the sample sizes and variances are unequal. The t-test was calculated using a significance-level of 95%. A Tukey box plot uses the length of the interquartile range (IQR) (the length of the box) to determine the whisker length. The IQR represent 50% of the data, which is from the middle number between the minimum value and the median to the middle number between the maximum value and the median. The whisker lengths are set to $\pm 1 \times$IQR. The values in the different regions are defined as significantly different if the IQR of the regions do not overlap. A problem often occurred when comparing the data from region 4 with the other regions; often the box plots would show significant differences but not the t-test. This problem occurs because

there are only two stations in region 4, meaning only two values per depth, which is too few for a robust t-test.

The correlation between some variables were determined by calculating a linear regression and hyperbolic approximation. The line was calculated using a model-2 least square fit, using the MatLab script by Peltzer (2016). For a model-2 regression line, neither X or Y is an independent variable, unlike a model-1 regression (figure 3.3). That is: a model 1 regression assumes Y (X) varies in response to X (Y), while a model 2 regression determine how X and Y co-vary in response to some other variable or process. The hyperbolic approximation was calculated by using the slope and Y-intercept obtained from the linear regression:

$$y = \frac{m \times x}{k + x} \tag{3.7}$$

$$m = \frac{1}{intercept}$$

$$k = slope \times m$$

To determine if the correlation of the regression was significant, a t-test was used to determine the significance of the correlation coefficient. The test uses the sample size and the calculated correlation coefficient to determine if the correlation coefficient of the population were significantly different from 0 (Bhattacharyya and Johnson, 1977).

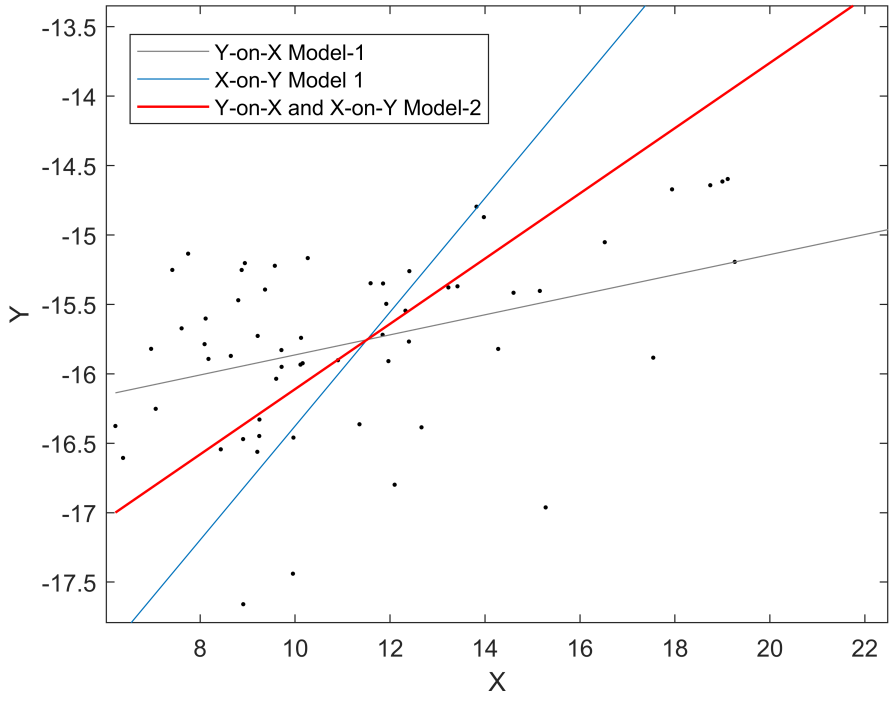

Figure 3.3: Visualization of the Model-2 regression (red line) compared to Model-1 regressions (gray line is Y-on-X and blue line is X-on-Y).

Chapter 4

Results

The variables divided in to five regions are: inorganic nutrients, inorganic and organic isotopes, particulate nutrients, and pico- and nanoplankton abundance (figure 4.1), which is determined by the different characteristics of the regions given by the temperature and salinity (figure 4.2) and latitudes of the different biomes (described in section 2.1):

- Region 0; the European shelf seas: is between 57°N and 41°N, which is in the subpolar and the seasonally stratified biome trough the North Sea, English Channel, Celtic sea and outside of the Bay of Biscay. Only water inlet measurements were done in this region. Results are therefore only at sea surface and for inorganic nutrients, DIC, TA, inorganic isotopes, and automated measuring systems.
- Region 1; northern subtopics: is between 41°N and 19°N, which is a seasonally satisfied biome along the North African coast and outside of the Iberian Peninsula.
- Region 2; tropics: is between 19°N and 12°S, which is in low latitude upwelling and equatorial upwelling biomes. The region starts where the Canary Current turns offshore by the equatorial winds, and continues through the equatorial upwelling.
- Region 3; southern subtropics: is between 12°S and 43°S, which is a permanently stratified biome. The ship sailed along its western boundary of the South Atlantic.
- Region 4; The Brazil-Malvinas confluence zone (BMCZ): is between 43°S and 48°S. It is a well-mixed region at the tip of South America where circumpolar waters enters the Atlantic Ocean.

The depth of the chlorophyll maximum (chl max) varied between 25 m, and 150 m, and is shown as the white line in figure 4.2. This depth therefore varies for all the figures that are presented. Notice that contour figures might

be misleading: the average distance between the stations was 457.58 km (calculated by Haversine formula and Pythagoras theorem), and there were only three depths at each station.

During the cruise, there were two major events causing loss of data from the automated measuring systems (thermosalinograph, oxygen optode, and pCO_2 measuring system). Between 43°N and 41°N the cap on the oxygen optode fell off, stopping the flow of water, and between 7°N and the equator, the system was shut down to clean the filters.

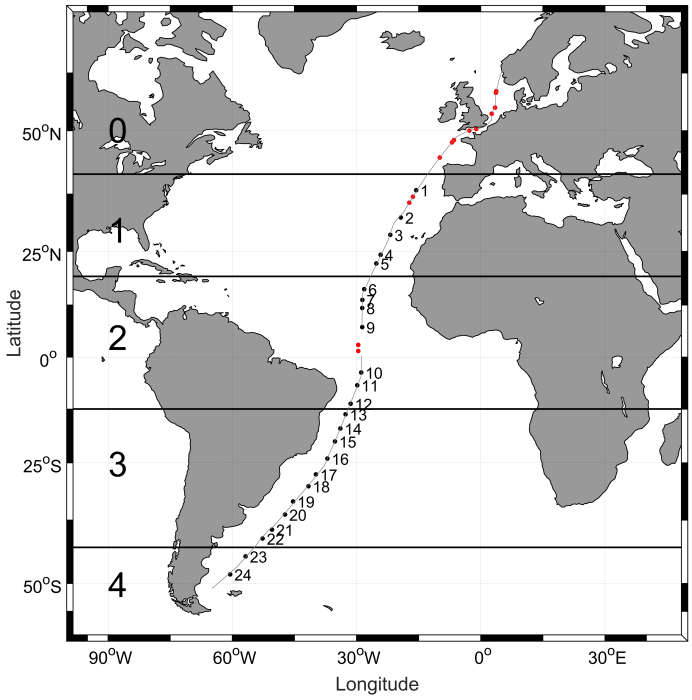

Figure 4.1: Map of transect with sampling locations, divided into the different regions. Red dots are the water inlet stations, the numbered black dots are the CTD stations, and the gray line is from the automated measuring system.

4.1 Temperature and Salinity

Figure 4.2 shows the temperature and salinity measured by the CTD and thermosalinograph, the chl max depth, and the isopycnals. The chl max depth is included in this figure to show how its depth changes over the different regions defined in section 4.

The sea surface temperature (SST) ranged between 10°C and 28°C. It increased toward lower latitudes and decreased toward higher latitudes, and the SST was generally higher at the Southern Hemisphere because it was aus-

tral summer (figure 4.2A). The sea surface salinity (SSS) ranged between 38 psu and 31 psu, with a more complex structure than SST (figure 4.2C). This increased complexity is due to the fact that the factors controlling salinity (evaporation (E), precipitation (P), and river runoff) vary more with latitude than insolation, which controls the temperature. The maximum SSS was observed in the subtropics, and the minimum in the tropics.

The temperature and salinity down to 200 m(figure 4.2B and D) shows Atlantic thermocline and gyre structures, and was used to define the different regions in figure 3.1. The upwelling regions around the equator (region 2) and in the BMCZ (region 4) were evident as colder and fresher water were transported upward from deeper layers. The subtropical gyres in the north Atlantic (region 1) and South Atlantic (region 3) where were identified by their high temperatures and salinities. The isopycnals align better with temperature than salinity, reflecting the dominating influence of temperature on density in the conditions experienced here (figure 4.2 B and D). Efficient mixing caused by wind stress and buoyancy forcing in the upper ocean creates vertical density lines, which is known as the mixed layer. The mixed layer depth was deepest at high latitudes because the temperature difference with depth is low.

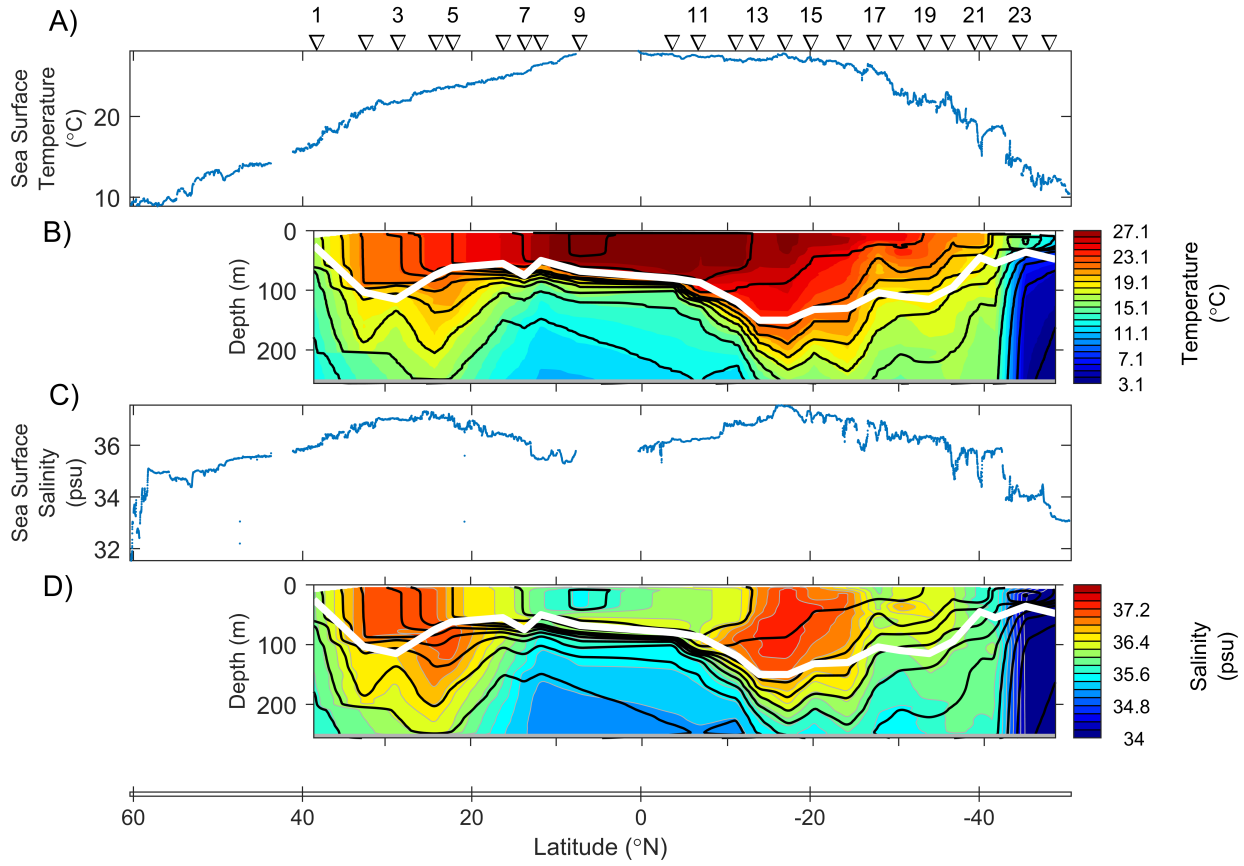

Figure 4.2: Sea surface A) temperature (°C) and C) salinity (psu) from thermosalinograph and, B) temperature (°C) and D) salinity (psu) measurements from CTD from 38°N to 48°S down to 200 m. The white line is the chl max depth, and the black lines are isopycnals in A) and B). The locations of the CTD stations is shown on top of figure A).

4.2 Dissolved Oxygen

Figure 4.3 show the dissolved oxygen concentration and saturation at sea surface and down to 200 m. The water sample drawing and preservation were evaluated by collecting duplicates at every station, and the mean and standard deviation at the sea surface are displayed in figure 4.3A and C. The average standard deviations of the duplicates from CTD (at all depths) was 1.21 μmol kg^{-1}, and 8.09 μmol kg^{-1} for water inlet duplicates. The CTD oxygen sensor values was evaluated by comparing to the water sample measurements, and these had an absolute mean difference of 12.72 μmol kg^{-1} $\pm$ 4.31 μmol kg^{-1}. Figure 4.3A and C shows a good agreement between optode and CTD values, while the water intake values were substantially higher and more variable than the optode values. This is likely artificial, a result of entrainment of air during sampling from the water intake where turbulence and bubbles were frequently observed in the sampling tube used. These data are therefore not considered any further.

Sea surface oxygen concentration decreases towards lower latitudes and increases towards higher latitudes (figure 4.3A). This latitudinal variability is almost the exact opposite to that of temperature (figure 4.2A) and reflects the temperature dependency of the oxygen solubility (Sarmiento and Gruber, 2006). This dependency is removed for the oxygen saturation, which thus gives information about other factors controlling the oxygen concentration (figure 4.3C). Most of the global ocean is supersaturated (Sarmiento and Gruber, 2006), which also was the case for these measurements. Generally, supersaturation in the ocean is caused by photosynthesis in productive areas (could be the case for the measurements done in the tropical upwelling and BMCZ), warming in non-productive areas (could be the case for the measurements done in subtropics) or bubble entrainment. Undersaturated waters were only present close to 60°N. This undersaturation, could be due to the deep winter mixed layer entraining undersaturated waters to the surface and because of cooling (Talley and Pickard, 2011; Ito et al., 2004).

The CTD oxygen concentrations (figure 4.3B and D) shows the following three main features. Firstly, the surface trend aligns with that presented in the previous paragraph and reflects the temperature dependency of the oxygen solubility. Secondly, close to the equator, upwelling brings old waters upwards, which has been without contact with the atmosphere for a long time and exposed to remineralization. The oxygen low waters stay under the thermocline, creating an undersaturated area with low oxygen concentrations below ~100 m. Thirdly, in the BMCZ, the oxygen levels are high and uniform, which is due to the Malvinas Current, which brings newly formed and ventilated Antarctic intermediate waters into the South Atlantic.

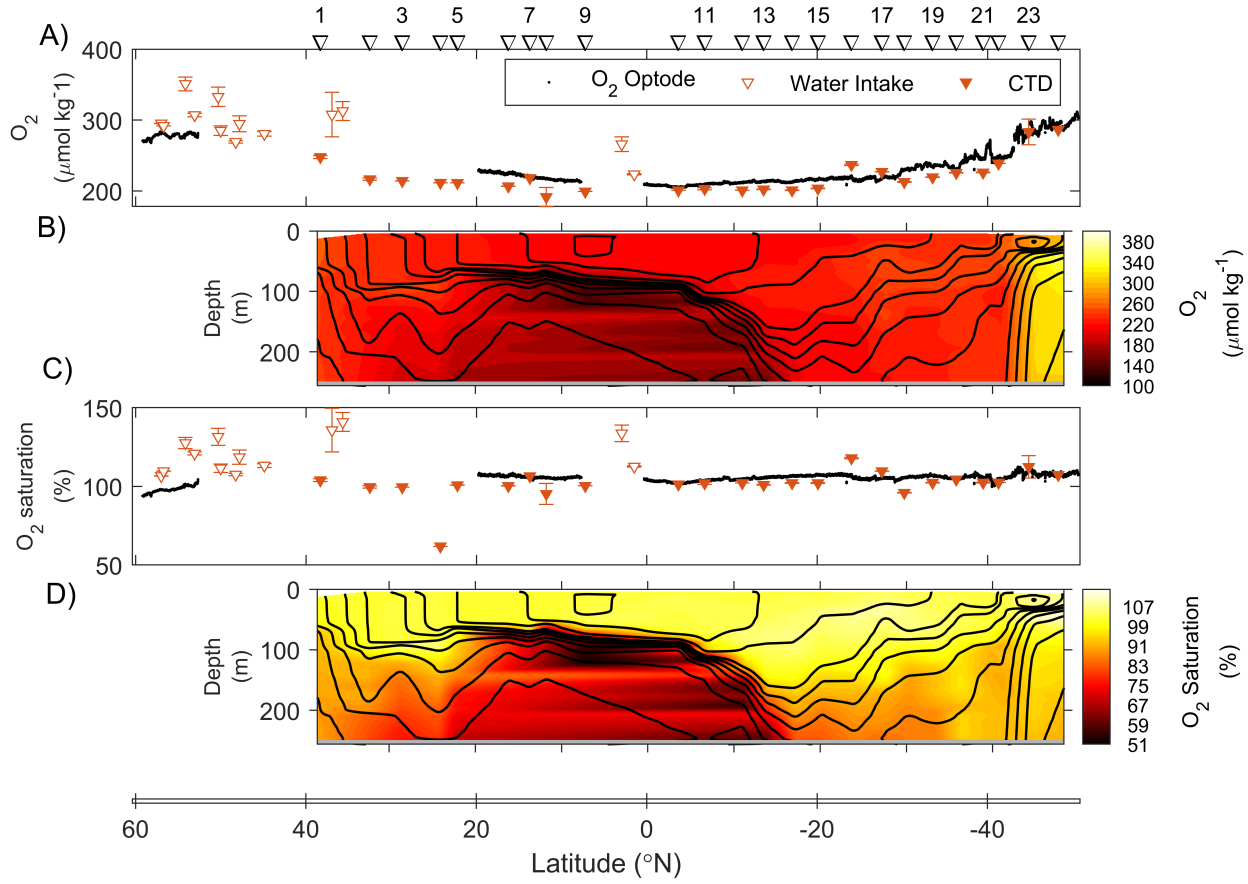

Figure 4.3: A) Dissolved O_2 consentration from the oxygen optode (black line), CTD niskin samples (filled triangles) and water inlet (open triangles), B) Dissolved O_2 consentration down to 200 m from CTD oxygen sensor, C) calculated O_2 saturation from oxygen optode (black line), CTD niskin samples (filled triangles) and water inlet (open triangles), and D) calculated O_2 saturation from CTD oxygen sensor down to 200 m. The loctions of the stations are displayed on top of the figure.

4.3 Inorganic Nutrients

Figure 4.4 shows the distribution of dissolved inorganic NO_3^-, PO_4^{3-} concentrations and figure 4.5 shows Si concentrations at the three depth levels sampled. The sample drawing and preservation were evaluated by collecting duplicate bottles at 200 m every third day. These have an absolute mean difference of 0.012 $\pm$0.082 μmol kg^{-1} for NO_3^-, 0 μmol kg^{-1} for Si, and 0.006 $\pm$0.005 μmol kg^{-1} for PO_4^{3-}. This difference indicates accurate sample drawing and good preservation. NO_2 was also measured, but not shown here because the concentrations were very low, and the variable is not important for further analysis. At the sea surface, the measurements were obtained from both the CTD and water inlet (figure 4.4A, B, and E and 4.5A). The figures are divided into the five different regions (defined in section 4), where regions 0 and 5 are in separate panels with different scales, because the values in these

regions differ a lot from in the other regions. Figure 4.6 show the box plots of NO_3^-, PO_4^{3-} and Si at the three depths for each region. The box plots were calculated using the procedure described in section 4. Figure 4.7 shows the relationship between NO_3^- and PO_4^{3-}, a linear regression line and the canonical Redfield ratio of 16:1. Figure 4.8 show the calculated $N^*=NO_3^- - 16\ PO_4^{3-}$ at the three depth levels sampled. N^* is a tracer for denitrification and nitrogen fixation where $N^*<0$ indicates denitrification, while $N^*>0$ indicates nitrogen fixation (Sarmiento and Gruber, 2006).

In all regions the concentration of all nutrients increased with depth and the largest increase occured between the chl max depth and 200 m (figures 4.4 and 4.5). As the chl max depth often aligns with the euphotic zone depth, the dissolved nutrients are often depleted above chl max depth. The change of NO_3^- with depth was much larger than for PO_4^{3-}, because during remineralization approximately 16 NO_3^- is released for every one PO_4^{3-} (chapter 2.2).

At the sea surface, NO_3^-, PO_4^{3-} were significantly higher in region 0 and 4, and Si was significantly higher in region 0 than in the other regions (figure 4.6), which is supported by a t-test. The high nutrient concentrations in region 0 were probably due to low primary production as it was winter, nutrient supply from river runoff and/or fall/winter mixing. Region 4 is in the BMCZ, where nutrients are supplied by the Malvinas current, which transfers nutrient-rich Southern Ocean waters to the South Atlantic Ocean. Unlike region 0, Si is not high in region 4, which can indicate a presence of a diatom abundance in this region (figure 4.5) (Sarmiento and Gruber, 2006). In region 1, 2 and 3 surface nutrient values were overall low (figure 4.4B and 4.5A). This is likely due to the lack of supply from below because of the strong stratification in the subtropics (region 1 and 3) and the equatorial regions (region 2) preventing the nutrient-rich waters from reaching the sea surface.

At the depth of chl max, PO_4^{3-}, NO_3^- and Si in region 4 were significantly higher than in the other regions, because of the supply of nutrients from the Malvinas current (figure 4.6). The low chl max depth nutrient concentrations in region 1, 2 and 3 were low because the samples were conducted in the subtropics (region 1 and 3), and because the chl max depth is above the thermocline in the equatorial region (region 2) (figure 4.4C and 4.5B). The chl max depth PO_4^{3-} and NO_3^- values at station 7 in region 2 were considerably higher than in region 2 because the sample was collected at a deeper level, below the thermocline, where the nutrient concentrations were high (figure 4.4C and 4.2).

At 200 m, the nutrient concentrations in region 2 and 4 were significantly higher than in region 1 and 3 (figure 4.6), which is supported by a t-test. The concentrations were high in region 2 because the samples were collected below the thermocline, where the upwelling of nutrient-rich waters is evident, while in region 4, it is due to the Malvinas current. In region 4 the nutrient concentration does not change as much with depth as in region 2, because the thermocline is much weaker (figure 4.4 and 4.5) (Olguín Salinas et al., 2015). The nutrients at 200 m in region 1 and 3 are still low, but slightly higher in region 1 than in region 3. This is because region 1 is on the eastern boundary of the Atlantic Ocean, close to the Canary Current upwelling; there is a greater supply of nutrients than region 3, which is on the western boundary (figure 4.4D and 4.5C).

In region 0 and 3 the NO_3^-:PO_4^{3-} relationship was low, which indicates either a high supply of PO_4^{3-} or a low supply of NO_3^- (figure 4.7). As region 0 was in the English Channel, it is reasonable to assume that there was a high supply of PO_4^{3-} from river runoff, while figure 4.8 indicates denitrification. Denitrification occurs in oxygen minimum where NO_3^- is used during matter degrading instead of oxygen. Oxygen depletion is common in areas where there is nutrient supply from river runoff, such as region 0, because it ultimately increases the remineralization (Keeling et al., 2010). In region 3 it was probably due to NO_3^- limitation, partly because it is a nutrient limited region and because N* indicates denitrification in region 3 (figure 4.8). The NO_3^-:PO_4^{3-} relationship in region 4 was close to the Redfield ratio, however, the Y-intercept indicates that NO_3^- was used up before PO_4^{3-} (figure 4.7). The Y-intercept is probably caused by denitrification, which is clearly indicated by N* (figure 4.8). While the slope is not affected by this because despite high levels of denitrification, the NO_3^- concentrations remained high because of the Malvinas current. The NO_3^-:PO_4^{3-} relationship in region 1 and 2 was close to the Redfield ratio (figrue 4.7), which fits with no denitrification as shown in figure 4.8.

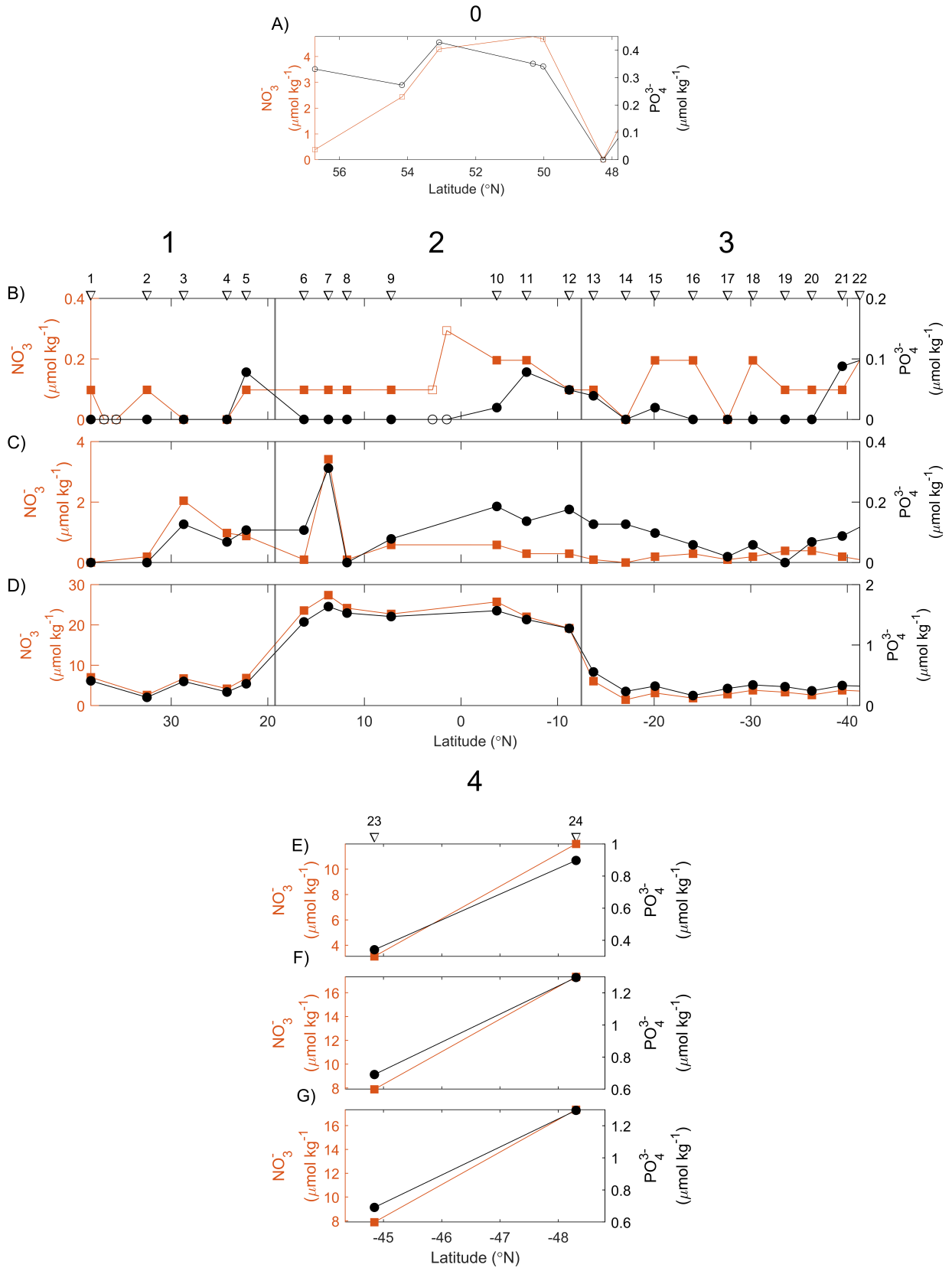

Figure 4.4: NO_3^- (squares) and PO_4^{3-} (circles) concentration at sea surface (A, B, and E), chl max depth (C and F), and at 200 m (D and G) in region 0, 1, 2, 3 and 4. At the sea surface, the measurements are from both CTD (filled symbols) and water inlet (open symbols). Note that the Y-scale changes between panels. The different regions are numbered on top of the panels. The locations of the CTD stations are displayed on top of the figure.

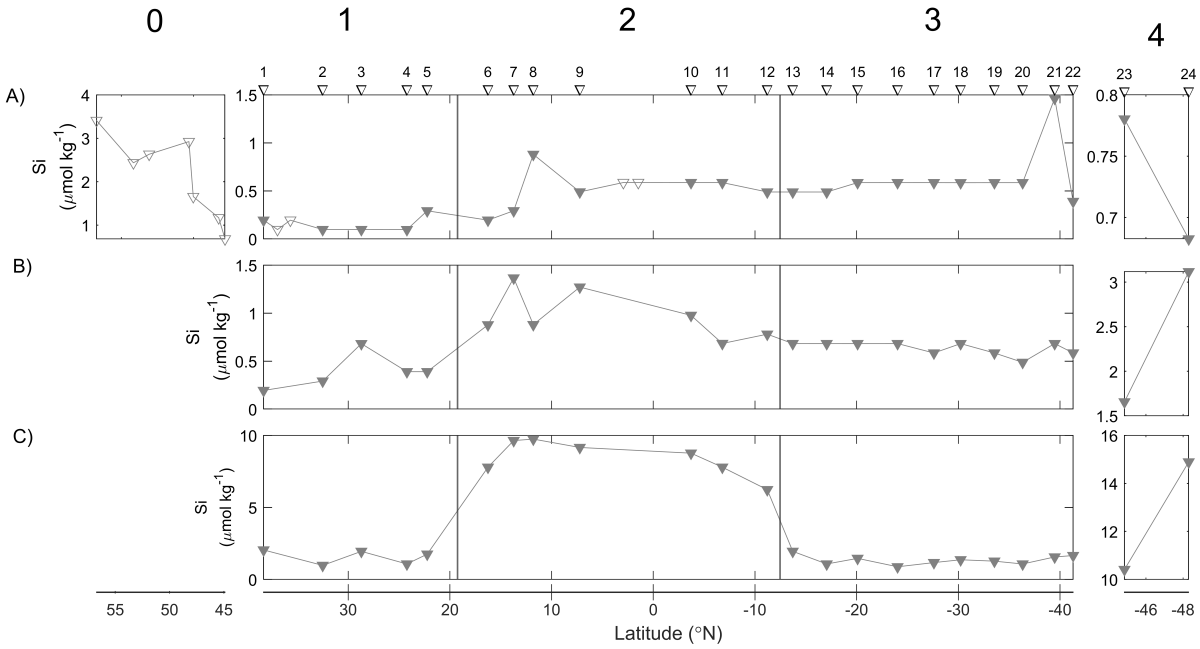

Figure 4.5: Si concentration in A) the sea surface, B) chl max depth and C) at 200 m in region 0, 1, 2 ,3 and 4. At the sea surface, the measurements are from both CTD (filled symbols) and water inlet (open symbols). Note that the Y-scale changes between panels. The different regions are divided by the black vertical lines with the region number on top. The locations of the CTD stations are displayed on top of the figure.

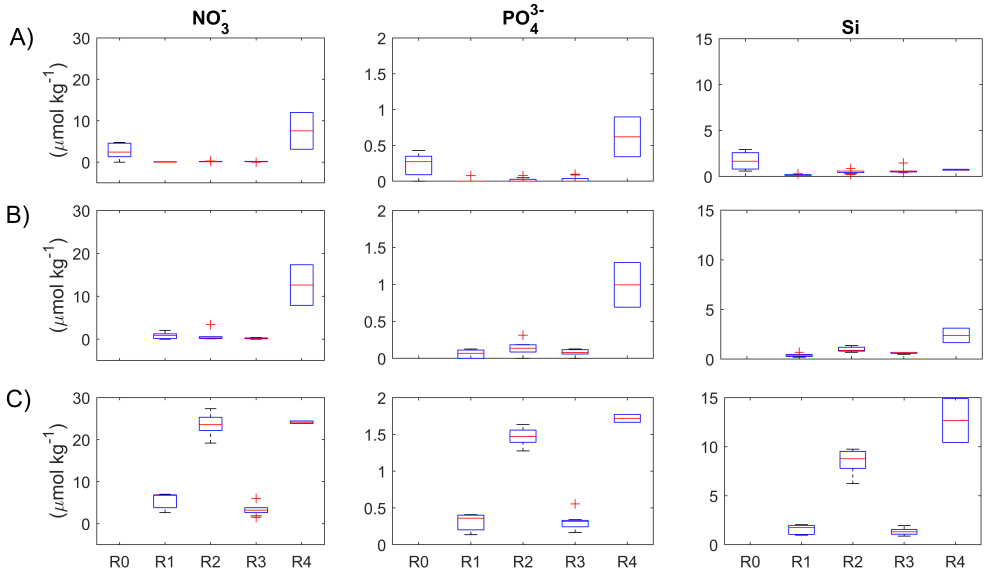

Figure 4.6: Box plot of NO_3^-, PO_4^{3-}, and Si at A) sea surface, B) chl max depth, and C) at 200 m in the different regions. Note that the Y-scale changes between panels.

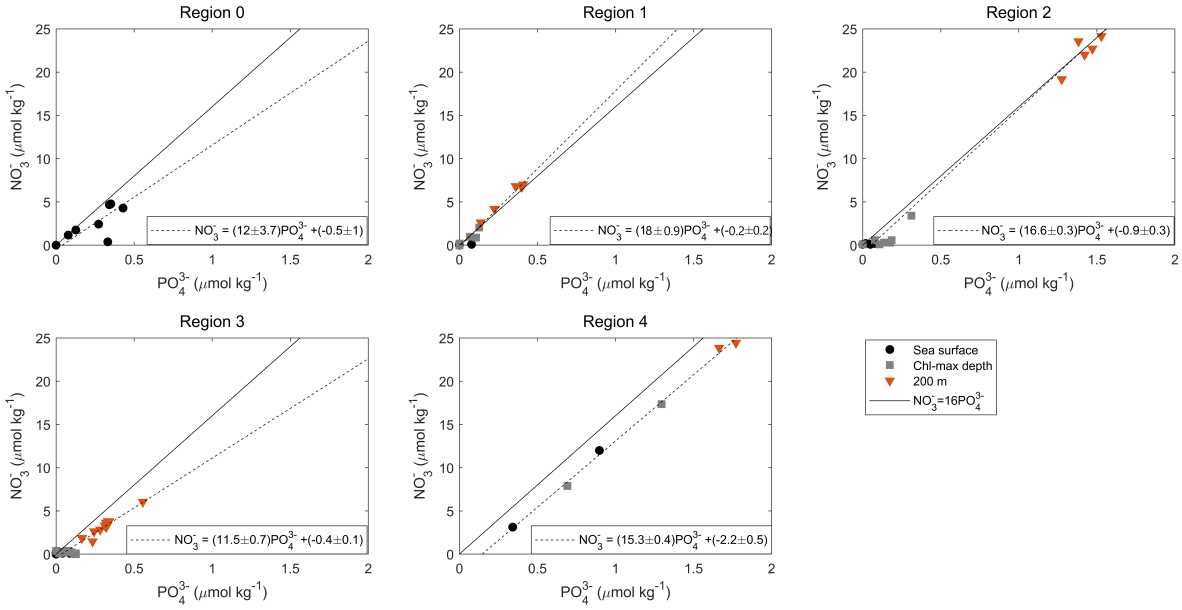

Figure 4.7: The relationship between NO_3^- and PO_4^{3-} at sea surface (black circles), chl max depth (gray squares), and at 200 m (red triangles), in the different regions. The solid line is the Redfield ratio, while the dashed line is the regression line, with the specific slope stated on each panel.

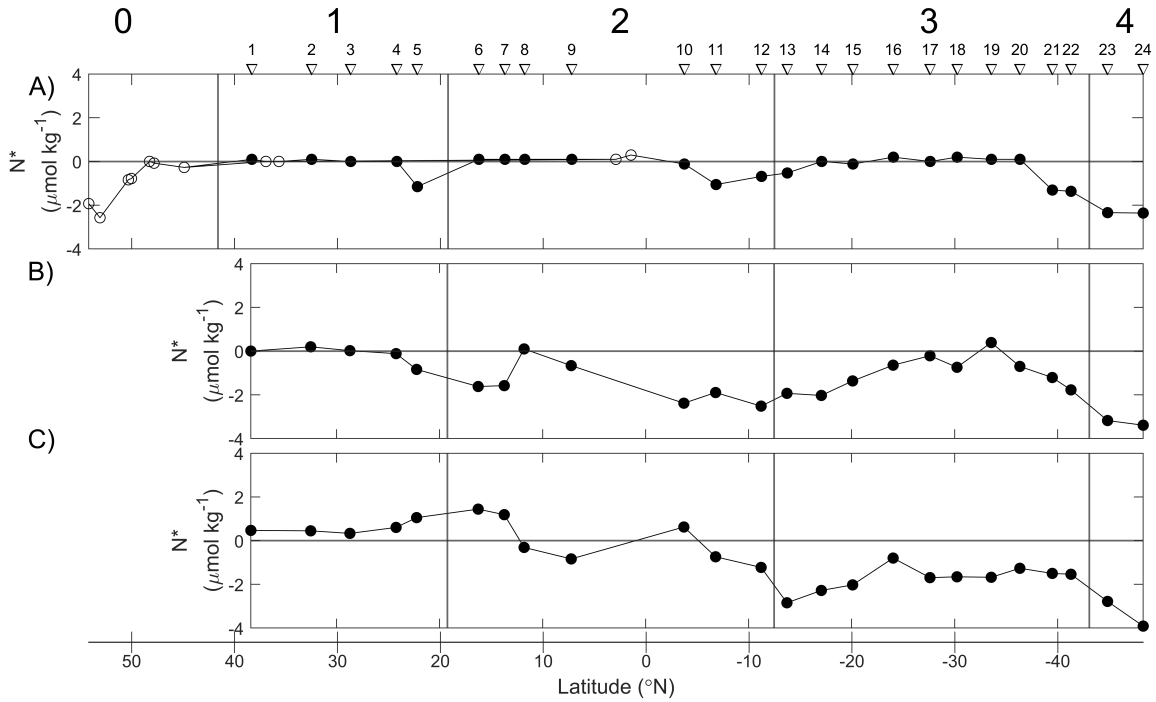

Figure 4.8: Calculated N* = NO_3^- - 16×PO_4^{3-}, at A) sea surface, B) chl max depth and C) at 200 m. The different regions are divided by the black vertical lines with the region number on top. The locations of the CTD stations are displayed on top of the figure.

4.4 Carbon Chemistry

Figure 4.9 shows the distribution of fCO_2, TA, pH, and DIC over the transect, and TA and DIC down to 200 m. For the water samples, the sample drawing and preservation were evaluated by collecting duplicate bottles at 200 m every third day; these had an absolute mean difference of 5.36 ± 8.75 μmol kg^{-1} for TA and 3.91 ± 2.46 μmol kg^{-1} for DIC. Figure 4.9 C and F was calculated using the water samples and is interpolated with respect to the chl max depth. These figures might be misleading as there were only three samples per depth and approximately 457.6km between each station.

In figure 4.9A, the fCO_2 data are compared with the atmospheric xCO_2 of approximately 400 μatm. Although, there were some areas where fCO_2 was higher than 400 μatm north of 40°N (approximately trough the English Channel (see figure 3.1)), fCO_2 was mostly below 400 μatm north of the equator. This indicates a likely net ocean uptake of CO_2. The low fCO_2 in the English Channel could be because the measurements were done in December, after a productive season and before the winter mixed layer had reached its maximum depth, combined with low temperatures, which increases the CO_2 solubility (decreasing the fCO_2 thermodynamically). The opposite was observed south of the equator, where the fCO_2 was above 400 μatm, indicating possible net outgassing of CO_2. South of about 30°S however, in the BMCZ, high primary production and low sea water temperatures strongly decreases the fCO_2.

For figure 4.9B, TA was calculated using temperature and salinity (figure 4.2) and aligns well with the measured TA from water samples. The distribution of TA (figure 4.9B and C) is reasonably similar to salinity (see figure 4.2) because open ocean TA is mainly controlled by salinity. (Lee et al., 2006). Consequently, TA was highest in the subtropics (approximately 20°N and °S) and lowest in the tropics (equator) and subpolar regions.

For figure 4.9C, TA values from water sampling depths at the CTD stations are used to show TA at depth. The distribution of TA is similar to the salinity (figure 4.2), as expected. The TA is low at 200 m in the equatorial upwelling and the BMCZ because of the upwelling of less saline waters, while in the subtropic convergence leads to deep penetration of fairly saline and high TA waters.

For figure 4.9D, pH was calculated using fCO_2 and the calculated TA in CO2sys. pH was below the average sea surface value of 8.1 over most of the transect, but is increasing south of about 30°S (Laufkötter et al., 2013). The waters south of 30°S are in the BMCZ, where the temperature is low, which results in a higher pH.

For figure 4.9E, DIC was determined using fCO_2 and the calculated TA in CO2sys, the same as for pH. The measured and calculated DIC values were similar north of 35°N and south of 13°S, but in between the measured DIC is lower than the calculated. The deviation is not caused by temperature and salinity difference between thermosalinograph and the CTD (validated by calculating DIC using the T/S data from both instruments). However, on the

day the low DIC samples were measured, the blank values were unusually low, such that the low values are likely due to measurement issues (poor cell sensitivity). However, the trend of the values follows the temperature and salinity as expected. DIC is mainly controlled by the air-sea gas exchange in the open ocean, and the gas exchange is mainly controlled by temperature where colder water contains higher concentrations because of solubility. While the salinity has a minor control on DIC, because DIC is partly made up of ions. DIC was low close to the equator where the salinity was low, and the temperature was high, while it was higher in the subtropics because of high salinity, and it was high at higher latitudes due to low temperatures. In the BMCZ, DIC is low because of high primary production.

Figure 4.9F shows that DIC increase with depth, and that DIC concentrations were generally higher south of the equator. This is probably caused by higher salinity in the subtropical region south of the equator, as it is austral summer. At 200 m, DIC is high close to the equator and in the BMCZ because of the upwelling of remineralized waters.

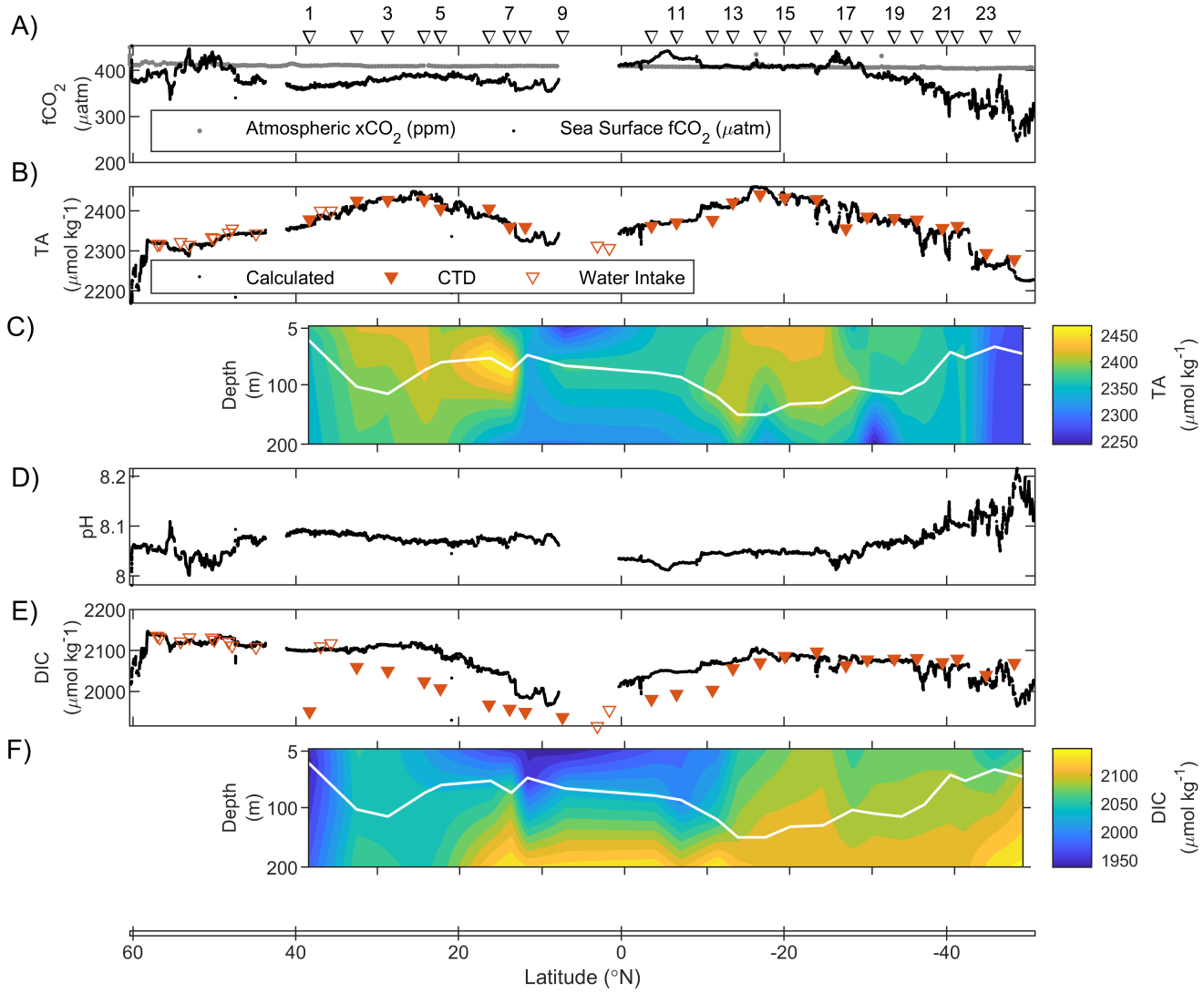

Figure 4.9: A) Measured sea surface fCO_2 (black) and atmospheric xCO_2 (grey) from the pCO_2 measuring system, B) calculated sea surface TA (black dots), and measured TA from CTD water samples (filled triangles) and water inlet samples (open triangles), C) TA to 200 m from measured CTD water samples, D) calculated pH, E) calculated DIC (black dots), measured DIC from CTD water samples (filled triangles) and measured water inlet samples (open triangles), and F) DIC to 200 m from measured CTD water samples.

4.5 Inorganic Carbon Stable Isotopic Ratio: $\delta DI^{13}C(‰)$

Figure 4.10 shows measured $\delta DI^{13}C(‰)$ at the three sampled depths. The precision of the instrument was evaluated by measuring on average three replicates of each bottle; the mean and standard deviation are displayed in figure 4.10. The sample drawing and preservation were evaluated by collecting duplicate bottles at 200 m every third day,

these have an absolute mean difference of 0.011 ± 0.012 ‰, indicating that the sample drawing and preservation was good. Figure 4.11 show the box plots of $\delta DI^{13}C(‰)$ for the three sampled depths in the different regions. The box plot was calculated using the procedures described in section 4. Finally, the relationship between PO_4^{3-} and $\delta DI^{13}C$ is plotted per region along with the linear regression line in figure 4.12. The regression line is compared to the $\delta^{13}C = \delta^{13}C_{(bio)} + \delta^{13}C_{(AS)}$ equation derived by Eide et al. (2017). Where $\delta^{13}C = 2.8 - 1.1PO_4^{3-}$ when $\delta^{13}C_{(AS)} = 0$ is the expected relationship between $\delta DI^{13}C$ and PO_4^{3-} during photosynthesis and organic matter remineralization. The trend of this equation is that $\delta DI^{13}C$ is high when PO_4^{3-} is low because of photosynthesis. If the regression line has a different slope or Y-intercept ($\delta^{13}C_{(AS)} \neq 0$) than the equation, it is an indication of additional influence of thermodynamic fractionation or the C Suess (intrusion of anthropogenic CO_2) affecting the $\delta DI^{13}C$ (section 2.4).

The sea surface (figure 4.10A) $\delta DI^{13}C$ was overall increasing over the entire transect from north to south. In region 0, $\delta DI^{13}C$ was significantly lower than in the other regions (figure 4.11), which is supported by a t-test. The low $\delta DI^{13}C$ values could be a result of the supply of water with low $\delta DI^{13}C$ from river run off. In Region 4, $\delta DI^{13}C$ was significantly higher than in the other regions (figure 4.11), which is supported by a t-test. The high $\delta DI^{13}C$ could have been caused by both high primary production and thermodynamic effect. However, as the relationship between $\delta DI^{13}C$ and PO_4^{3-} differs from the $\delta^{13}C_{(bio)}$ line, which means that $\delta DI^{13}C$ is not solitary affected by biology, and indicates that the thermodynamic effects was the probable cause (figure 4.12). The surface $\delta DI^{13}C$ in region 1 and 3 was slightly lower than in region 2, probably because region 1 and 3 covers the subtropical gyres, where $\delta DI^{13}C$ is expected to be low because of C suess effect (which is strong because of the long residence times of waters there), while in region 2, the equatorial upwelling brings older waters that have not been exposed to the current atmosphere to the surface. (Eide et al., 2017). This inference is supported by the $\delta DI^{13}C$ vs. PO_4^{3-} relationship ; for any given PO_4^{3-} concentration in region 1 and 3, the $\delta DI^{13}C$ is lower than in region 2 (figure 4.12).

At the depth of the chl max, $\delta DI^{13}C$ follows the same trend as at sea surface (figure 4.10B), $\delta DI^{13}C$ was low in the subtropical regions: region 1 is significantly lower than region 2 and region 3 is significantly lower than region 4 (figure 4.11), which is supported by a t-test. As at the sea surface, the $\delta DI^{13}C$ in region 1 and 3 were low, probably due to the C Suess effect, while it was higher in region 2 because of the lack of C Suess effect, and in region 4 because of thermodynamic effect (figure 4.12).

At 200 m, the $\delta^{13}C$ is lower than at the depth of chl max and the sea surface, as expected because at this depth, remineralization dominates. The $\delta DI^{13}C$ in region 4 is significantly higher than in the other regions (figure 4.11), probably because of thermodynamic fractionation. In region 2, $\delta DI^{13}C$ was significantly lower than in region 1 and 3 (figure 4.11), which is supported by a t-test. The samples were collected underneath the thermocline, dominated by old waters upwelled with large amounts of remineralized carbon, explaining the low $\delta DI^{13}C$ and high PO_4^{3-} values (figure 4.12). $\delta DI^{13}C$ in region 3 was significantly higher than in region 1 (figure 4.11), which is supported by a t-test. This could be because region 1 is on the eastern boundary, where the low $\delta DI^{13}C$ could be a result of upwelling as in region 2, while region 3 is on the western boundary where there is no upwelling.

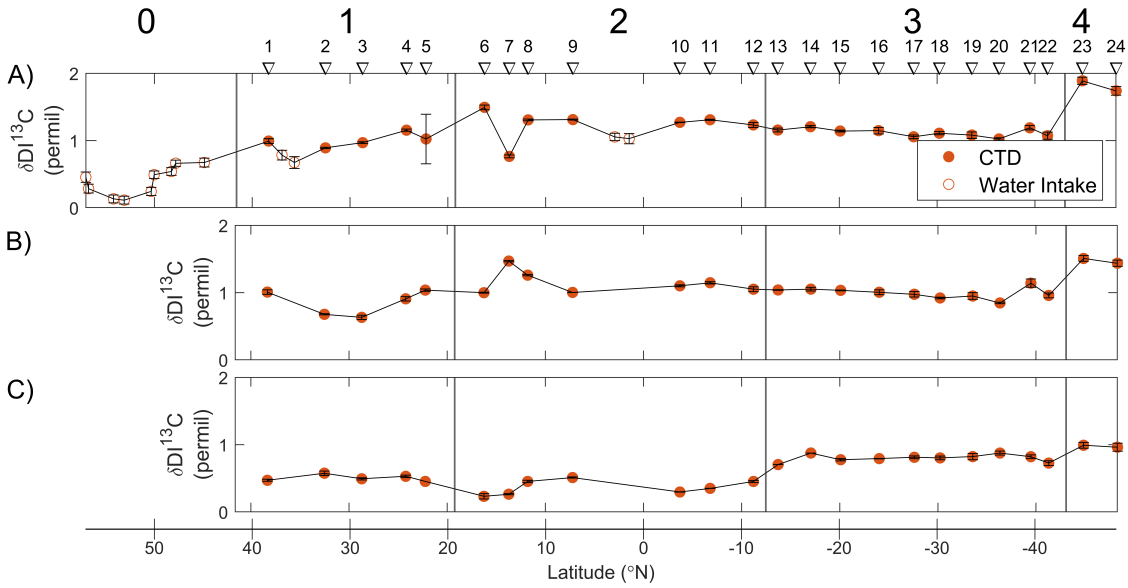

Figure 4.10: Measured δDI^{13}C(‰) at A) sea surface, B) depth of the chl max and C) at 200 m. Note that the Y-scale changes between panels. The measurements were conducted from both CTD (filled symbols) and water inlet (open symbols) samples. The locations of the stations are displayed on top of the figure.

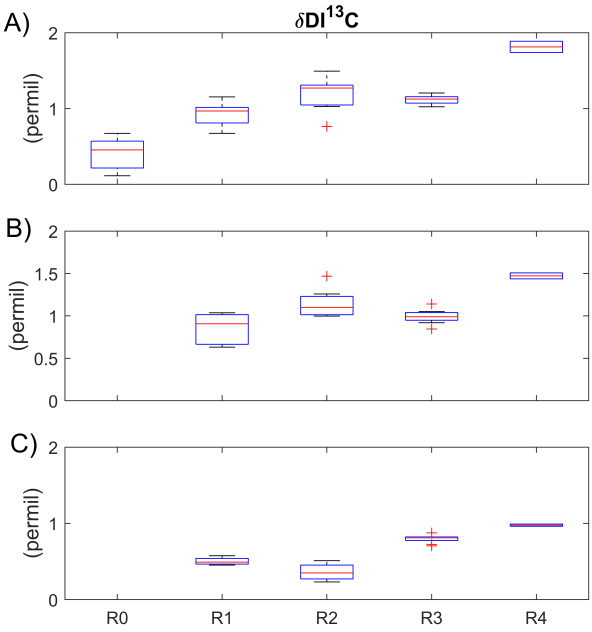

Figure 4.11: Box plot of δDI^{13}C(‰) at A) sea surface, B) depth of the chl max, and C) at 200 m in the different regions. Note that the Y-scale changes between panels.

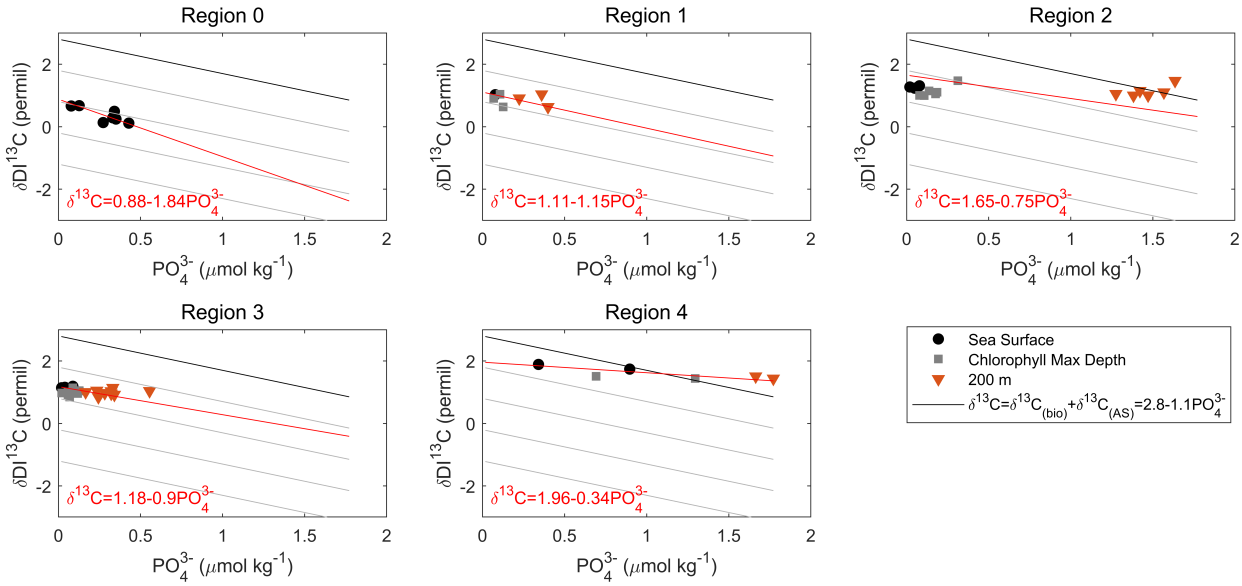

Figure 4.12: The relationship between $\delta^{13}C$ and PO_4^{3-} at sea surface (black cicles), chl max depth (gray squares), and 200 m (red triangles) in the different regions. The red line in each panel is the calculated regression line, and the black line is $\delta^{13}C = \delta^{13}C_{(bio)} = 2.8 - 1.1PO_4^{3-} + \delta^{13}C_{(AS)}$, at $\delta^{13}C_{AS}=0$. The grey lines are $\delta^{13}C_{(AS)}$ at -1‰ intervals (Eide et al., 2017).

4.6 Organic Nitrogen and Carbon Stable Isotopic Ratio: $\delta PO^{15}N$(‰) and $\delta PO^{13}C$(‰)

Figure 4.13 shows the distribution of $\delta PO^{15}N$ and figure 4.14 shows organic $\delta PO^{13}C$ at the three sampled depths. Replicates were taken at every depth at every measured station, and the mean and standard deviation are displayed in the figures. Figure 4.15 show the box plots of $\delta PO^{15}N$ and $\delta PO^{13}C$ at the sampled depths in the different regions. The box plot is calculated using the procedure described in section 4. Figure 4.16 shows the relationship between $\delta PO^{15}N$ and N* and figure 4.17 shows the relationship between $\delta PO^{13}C$ and $\delta DI^{13}C$.

A challenge with both the $\delta PO^{15}N$ and the $\delta PO^{13}C$ measurements was the low concentration of Particulate Organic Matter in the water that was sampled, as a large fraction of the cruise covered oligotrophic regions. In principle, if the amount of matter on the filter does not result in a signal with amplitude above 1000 hz in the IRMS, the result should not be used. None of the $\delta PO^{15}N$ results (figure 4.13) met this criterion. In an attempt to get the strongest possible signal, the entire filter and two tin capsules were used for each sample, but this resulted in uneven burning of the filets. During the process of finding the best way to analyse the filters, several filters were lost as they were physically damaged, which resulted in poor signals. Regardless of the low signal, the overall $\delta PO^{15}N$

results align with expected values (see section 2.4), so the results will be used further.

$\delta PO^{15}N$ and N* are negatively correlated, N* is >0 (indication of N_2 fixation) where $\delta PO^{15}N$ is <0 and N* <0 (indication of denitrification) (figure 4.16). This correspond with the theory in section 2.4, and $\delta PO^{15}N$ may therefore be used as an indication of nitrogen fixation and denitrification. The spatial variations of $\delta PO^{13}C$ are similar to those inorganic $\delta DI^{13}C$ in the current regions (figure 4.17) this similarity will be further investigated in section 5.1.

At the sea surface, $\delta PO^{15}N$ was mostly negative (figure 4.13), which is lower than the expected $\delta PO^{15}N$ of marine algae (figure 2.6). As N_2 fixation is common in the subtropical regions, it is reasonable to believe that this is what caused the low $\delta PO^{15}N$. $\delta PO^{13}C$ at sea surface was close to -24‰, which is the expected value (figure 4.14) (Ohkouchi et al., 2015). $\delta PO^{13}C$ in region 2 was significantly higher than in the other regions (figure 4.15), which is supported by a t-test.

At the depth of chl max, the $\delta PO^{15}N$ was below zero and it is reasonable to believe there was nitrogen fixation in region 1 and 3 at this depth too (figure 4.13 and 4.8). $\delta PO^{13}C$ at the depth of chl max was fairly constant over the transect and overall lower than at the sea surface (figure 4.14).

At 200 m depth $\delta PO^{15}N$ was increasing from north to south (figure 4.14), which supports the inference that denitrification affects region 3 (section 4.3). $\delta PO^{13}C$ at 200 m was overall similar to the values observed at the depth of chl max. This is counterintuitive because at 200 m it is expected to be more remineralization than photosynthesis, which would result in higher $\delta PO^{13}C$ as the lighter ^{12}C is used up during remineralization.

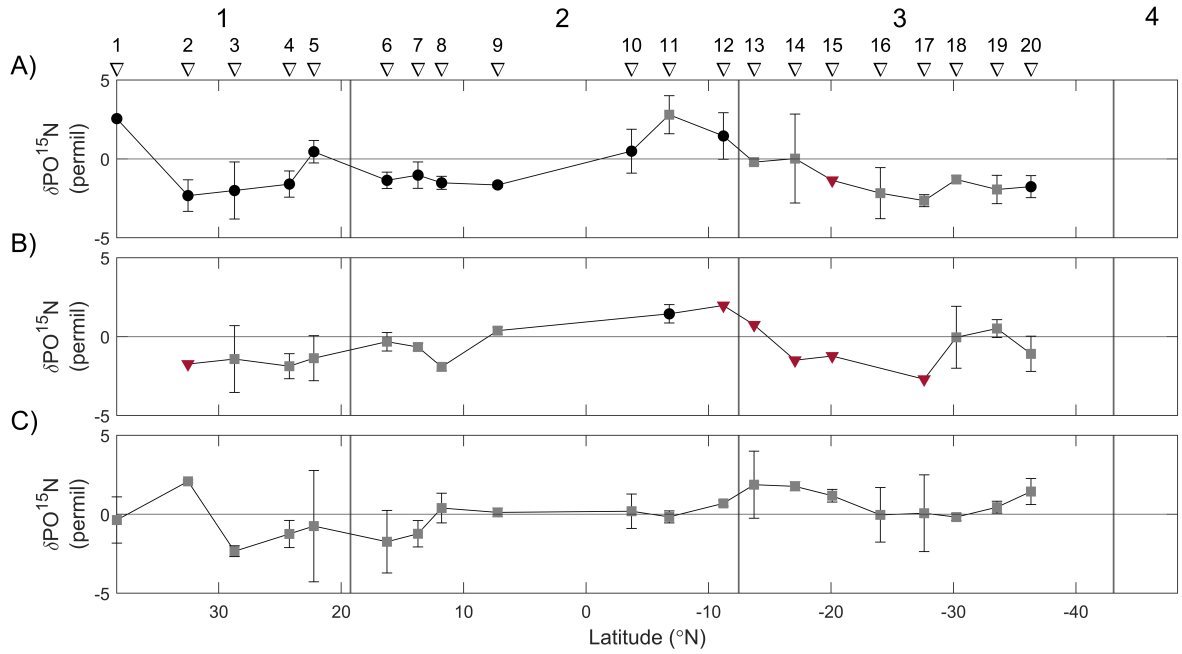

Figure 4.13: Measured $\delta PO^{15}N$(‰) at A) sea surface, B) chl max depth and C) at 200 m. Black circles indicate that three replicates were measured, gray squares two, and red triangles one. For each sample with two or three replicates, the standard deviation is plotted. The regions are divided by the black vertical lines, with numbers on top. The locations of the stations are displayed on top of the figure.

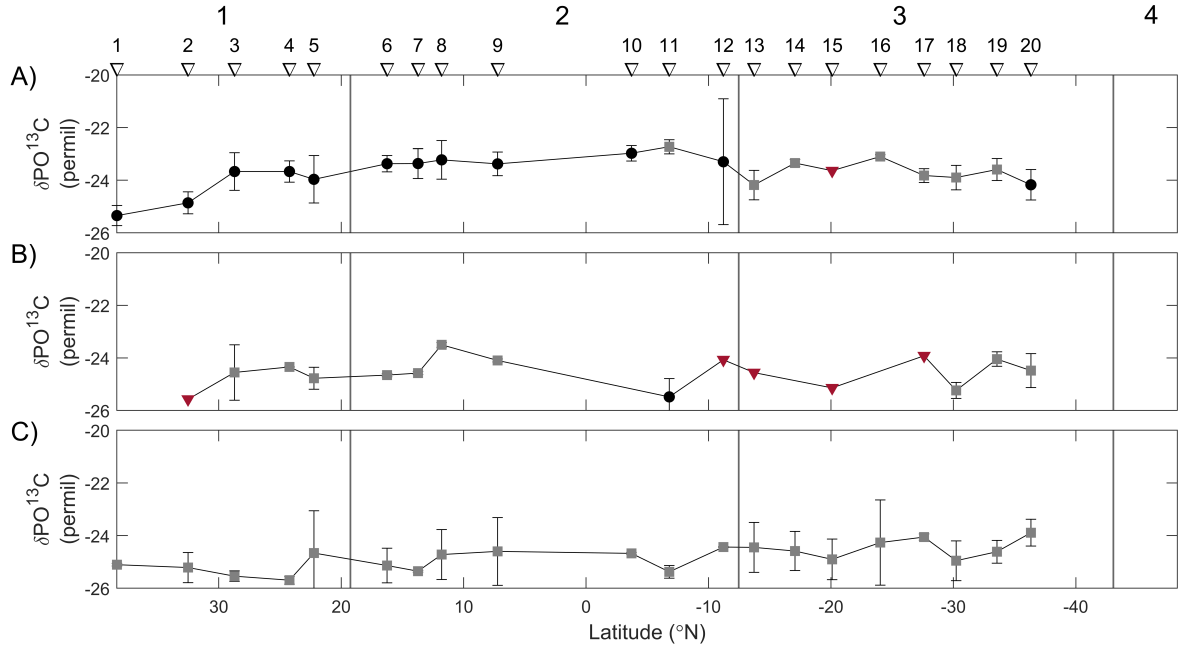

Figure 4.14: Measured $\delta PO^{13}C$(‰) at A) sea surface, B) chl max depth and C) at 200 m. Black circles indicate that three replicates were measured, gray squares two, and red triangles one. For each sample with two or three replicates, the standard deviation is plotted. The regions are divided by the black vertical lines, with numbers on top. The locations of the stations are displayed on top of the figure.

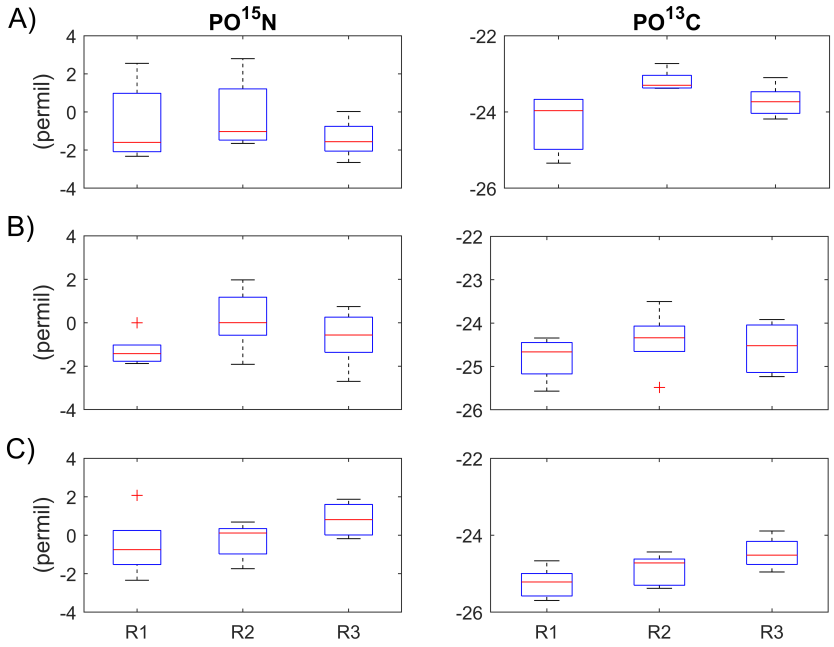

Figure 4.15: Box plot of $\delta PO^{15}N$ and $\delta PO^{13}C$ at A) sea surface, B) chl max depth and C) at 200 m in the different regions displayed at the bottom of the figure.

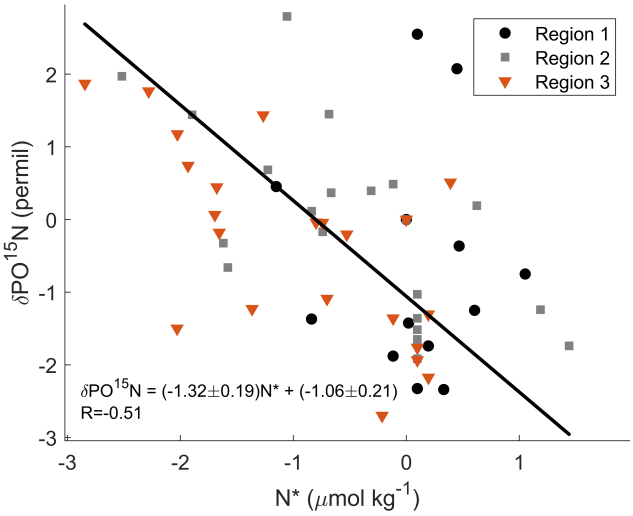

Figure 4.16: The relationship between measured $\delta PO^{15}N$ and N*

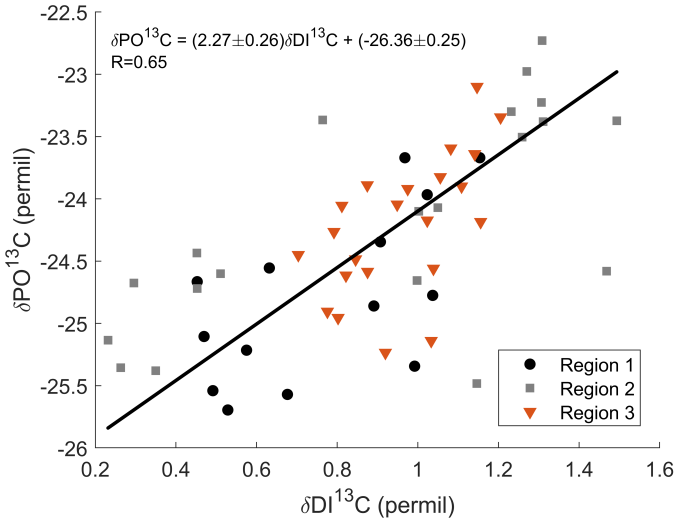

Figure 4.17: The relationship between measured $\delta DI^{13}C$ and $\delta PO^{13}C$

4.7 Particulate Elements

Figure 4.18 and 4.19 shows the concentration of particulate nutrients (P and Si from polycarbonate filters (PC) and N and C from glass fibre filters (GF/F)) at the three sampled depths. Three replicates were taken at every sampling depth, and the mean and standard deviation of these are displayed on each point. Stations where the measured values were below the detection limit (section 3.1.9) are not shown in the figure. Figure 4.20 shows the N:P ratio (both from GF/F filter). For this figure, all values are used, although some of the values were under the detection limit. As the relative ratio between N and P is correct even if the values are below the detection limit. Figure 4.21 shows the box plots of P, Si, N, and C at the three depths in the different regions. The box plot was calculated using the procedures described in section 4.

At the sea surface, the concentrations of particulate N, P, Si, and C were significantly higher in region 4 than in the other regions (figure 4.21), which is supported by a t-test. The concentrations of particulate nutrients were high in region 4 and the southernmost station in region 3 because the stations were taken close to, or inside, the BMCZ (an area with a supply of nutrient-rich waters from the Malvinas current) (figure 4.4 and 4.5). The high particulate Si in region 4 compared to the low inorganic Si supports the inference based on nutrients (Section 4.3), that the abundance of diatoms were large in this region. In region 1, 2 and 3, the concentrations of all measured particulate nutrients were low with minor variability (figure 4.18 and 4.19). This is most likely due to the overall low availability of inorganic nutrients in tropical and subtropical surface water, which keeps biololgical activity low.

At the depth of the chl max, concentrations of all particulate nutrients were similar to, or slightly above, those

at the sea surface (figure 4.18 and 4.19); this is expected as part of the particulate nutrients is organic matter, which is produced by photosynthesizing organisms containing chlorophyll. The N, P, Si concentrations at the chl max depth in region 4 were significantly higher than in region 1, 2, and 3 (figure 4.21), which is supported by a t-test. The P, N, and C values in region 2 were slightly higher than in region 1 and 3. The higher values in region 2 could be a result of specialised organisms migrating below the thermocline to harvest from the rich supplies of nutrients in the upwelling waters.

At 200 m, the particulate nutrient levels were significantly lower than those at the depth of the chl max and at the sea surface (figure 4.18 and 4.19). As this is below the euphotic depth, it likely reflects low concentrations of primary producers. P and Si were significantly higher in region 4 than in the other regions (figure 4.21), which supports the assumption of diatom growth in the region. The high concentrations of Si and P at 200 m could be a result of sinking dead cells, or live diatoms who can adjust their buoyancy to go below the euphotic zone to collect nutrients (Sarmiento and Gruber, 2006). Several values of C and N in region 1, 2, and 3 were below the detection limit and are not plotted in the figure 4.18 and 4.19 or used in the calculations of the box plot and t-test. The lack of data makes the box plot in figure 4.21 and t-test not trustworthy.

The slope of the N:P regression lines for the particulate matter is lower than the Redfield ratio in all regions, which indicates an overall N limitation over the entire transect (figure 4.20). However, the N:P ratio in regions 1, 2, and 4 are relatively similar and higher than in region 3, which was also the case for the inorganic NO_3^-:PO_4^{3-}. This could be because region 1 and 2 are on the eastern boundary where there is nutrient upwelling, and region 4 is in the nutrient-rich BMCZ, while region 3 is on the western boundary of the nutrient-poor subtropical gyre. Possible causes for the variations in C:N:P will be further investigated in section 5.1.

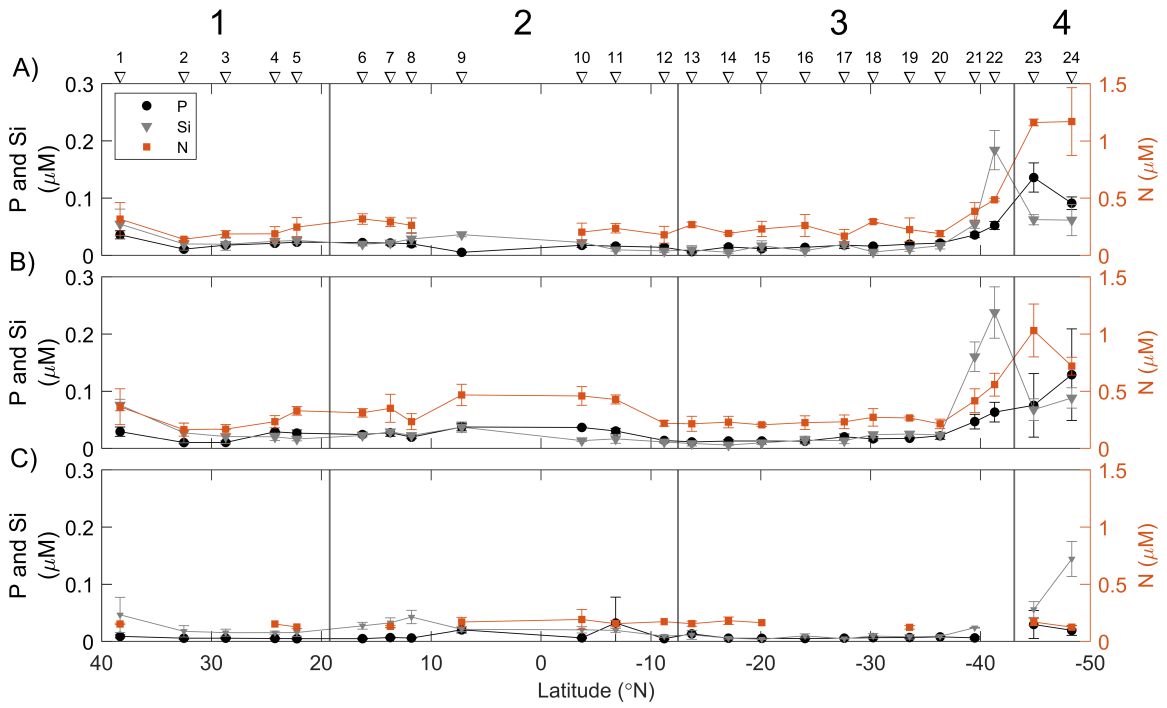

Figure 4.18: Particulate P (circles), Si (triangle), and N (squares) concentrations at A) the sea surface, B) the chl max depth, and C) at 200 m. Note that the Y-scale changes between panels. The different regions are divided by the black vertical lines with the region number on top. The locations of the CTD stations are displayed on top of the figure.

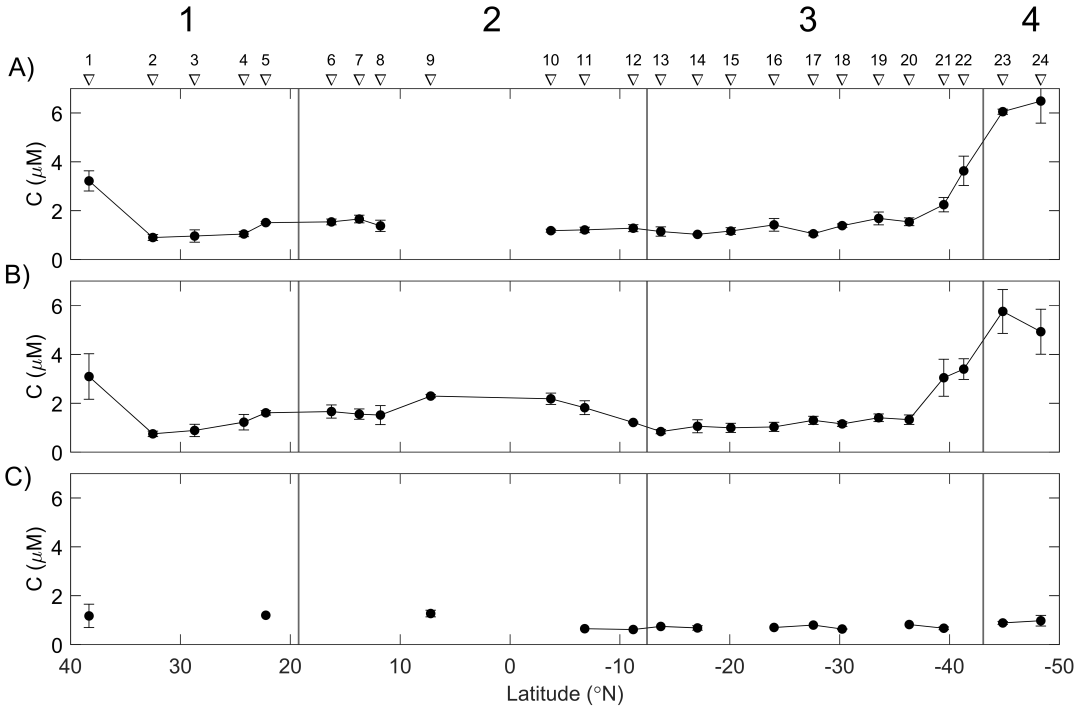

Figure 4.19: Particulate C concentration at A) the sea surface, B) the chl max depth, and C) at 200 m. Note that the Y-scale changes between panels. The different regions are divided by the black vertical lines with the region number on top. The locations of the CTD stations are displayed on top of the figure.

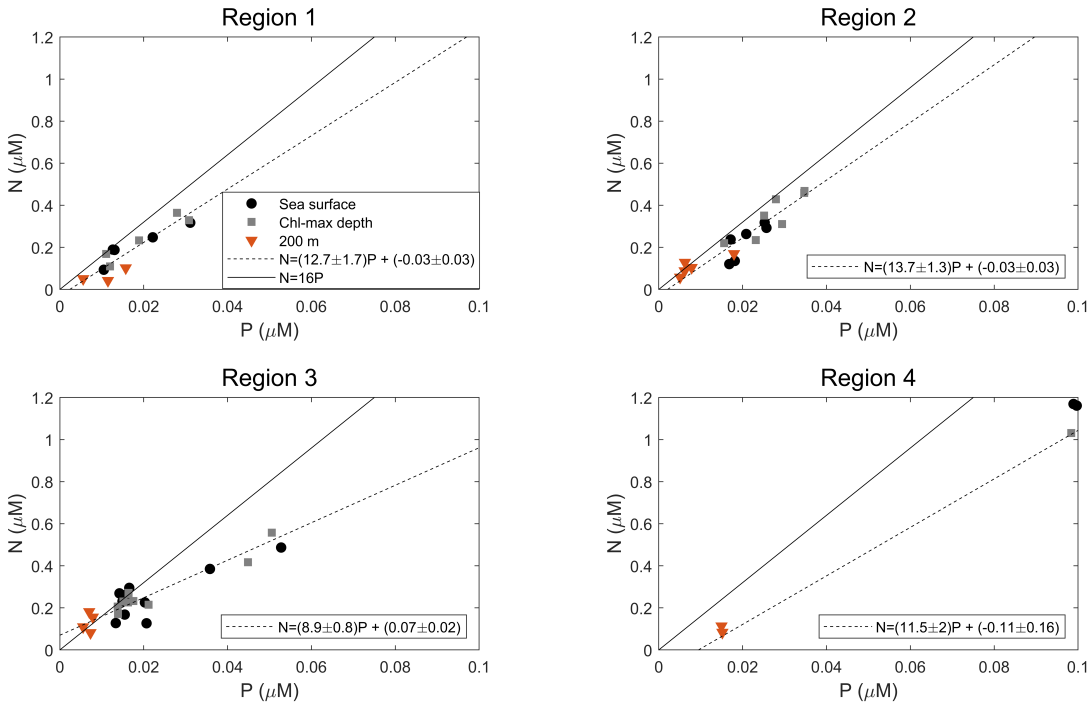

Figure 4.20: The relationship between N and P at the sea surface (black circles), the chl max depth (gray squares), and at 200 m (red triangles) in the different regions. The solid line is the Redfield ratio, while the dashed line is the regression line, with the specific slope stated on each panel.

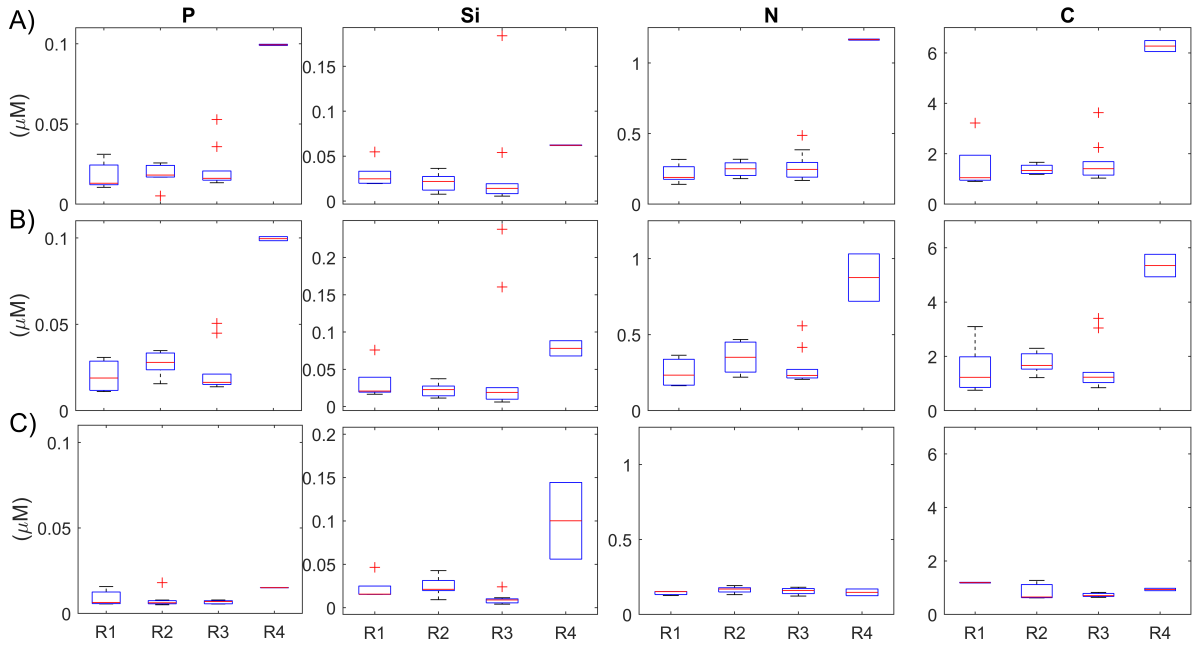

Figure 4.21: Box plot of P, Si, N, and C at A) the sea surface, B) the chl max depth, and C) at 200 m in the different regions. Note that the Y-scale changes between panels.

4.8 Nano- and Picoplankton Abundance

Figure 4.22, figure 4.23, and figure 4.24 shows the abundance of picoplankton (picoautotrophs), synechoccus, nanoplankton 1, nanoplankton 2 and heterotrophic bacteria at the three sampled depths. Figure 4.25 shows the box plots of all the groups at the three depth in the different regions. The box plot was calculated using the procedure described in section 4.

At the sea surface, the abundance of picoplankton, synechoccus, nanoplankton 1, nanoplankton 2 were low in region 4 compared to what is expected from the particulate nutrient concentrations (figure 4.22, 4.23 and 4.19). This could support the assumption of a high diatom abundance in region 4, because the flowcytometer does not count diatoms and these are consequently not evident in figure 4.22 or 4.23. Picoplankton, synechoccus, nanoplankton 1, nanoplankton 2 were most abundant at the southmost most point in region 3, probably because of a supply of nutrients from the nutrient-rich BMCZ region in region 4. The bacteria abundance was higher in region 4 compared to the other regions, which could indicate that there were most organisms in region 4 despite what is shown by picoplankton, synechoccus, nanoplankton 1, and nanoplankton 1 (figure 4.24).

At the depth of chl max, the abundance of picoplankton was higher than the abundance of other groups in all regions (figure 4.22 and 4.23). Picoplankton are small and able to adjust their elemental ratio based on the nutrient limitation in the region, which is too energy-costly for bigger species (Luis Otero-Ferrer et al., 2018). Therefore, there was a high abundance of picoplankton in the nutrient-poor subtropics (region 1 and 3) and above the thermocline in the equatorial region (region 2). Nanoplankton 1 and nanoplankton 2, however, are larger plankton who needs higher nutrient concentrations, and had therefore a higher abundance in region 2 and at the southmost point in region 3 compared the other regions (figure 4.23). Synechoccus is the same size range as picoplankton but is usually more abundant in upwelling regions, which was evident at the same point as nanoplankton 1 and nanoplankton 2 in region 3 (figure 4.22). The trend of the bacteria abundance was almost identical to the sea surface (figure 4.24).

The picoplankton, synechoccus, nanoplankton 1, and nanoplankton 1 abundance were lower at 200 m than the depth of chl max and the sea surface, because it is beneath the euphotic zone depth (figure 4.22 and 4.23). Bacteria were also quite a bit lower (a factor of ten) lower at 200 m than at the other depth levels, despite not being dependent on sunlight. The likely reason is the higher supply of organic matter to decompose at the depth of chl max and at the sea surface (figure 4.24). The abundance of bacteria is significantly higher in region 4 , at all three levels, than in the other regions (figure 4.25), which is supported by a t-test.

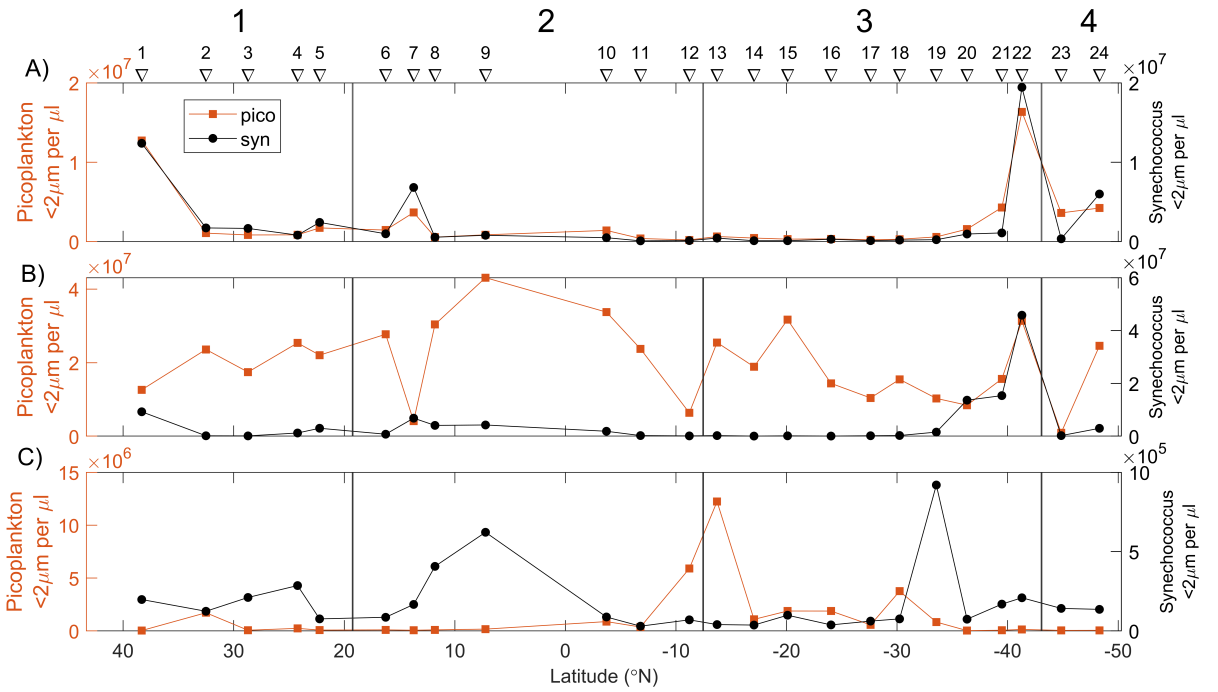

Figure 4.22: Picoplankton and synechococcus at A) the sea surface, B) the chl max depth, and C) at 200 m. Note that the Y-scale changes between panels. The different regions are divided by the black vertical lines with the region number on top. The locations of the CTD stations are displayed on top of the figure.

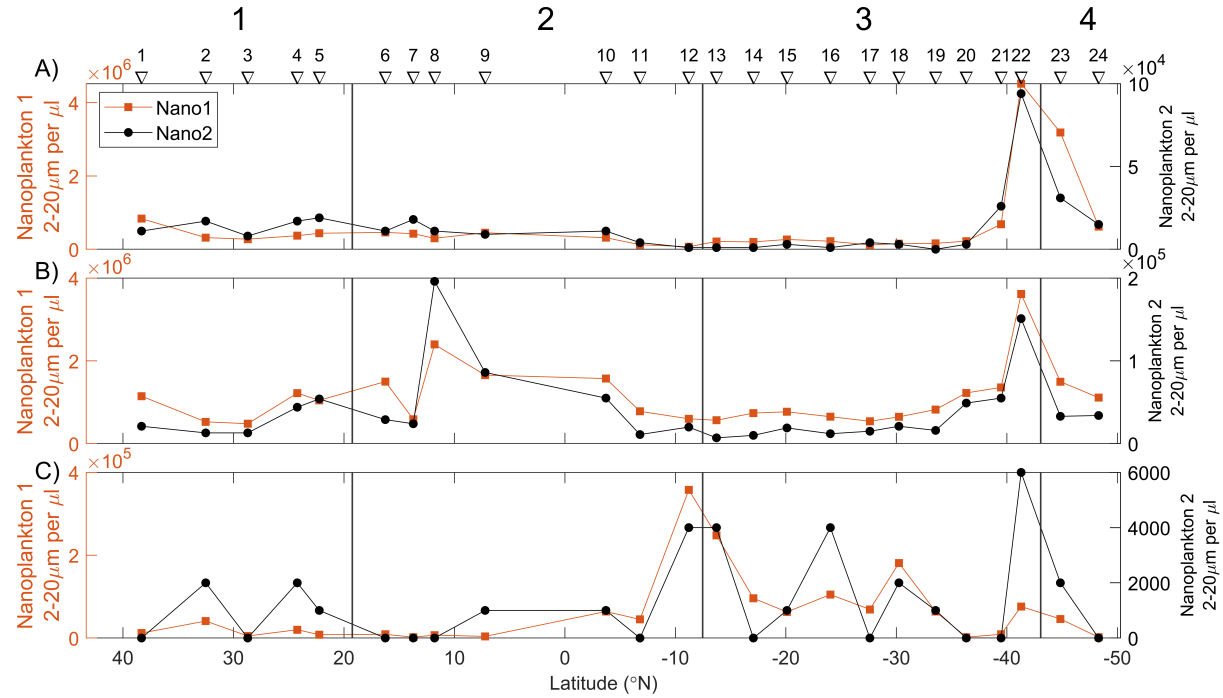

Figure 4.23: Nanoplankton 1 and nanoplankton 2 at A) the sea surface, B) the chl max depth, and C) at 200 m. Note that the Y-scale varies across panels. The different regions are divided by the black vertical lines with the region number on top. The locations of the CTD stations are displayed on top of the figure.

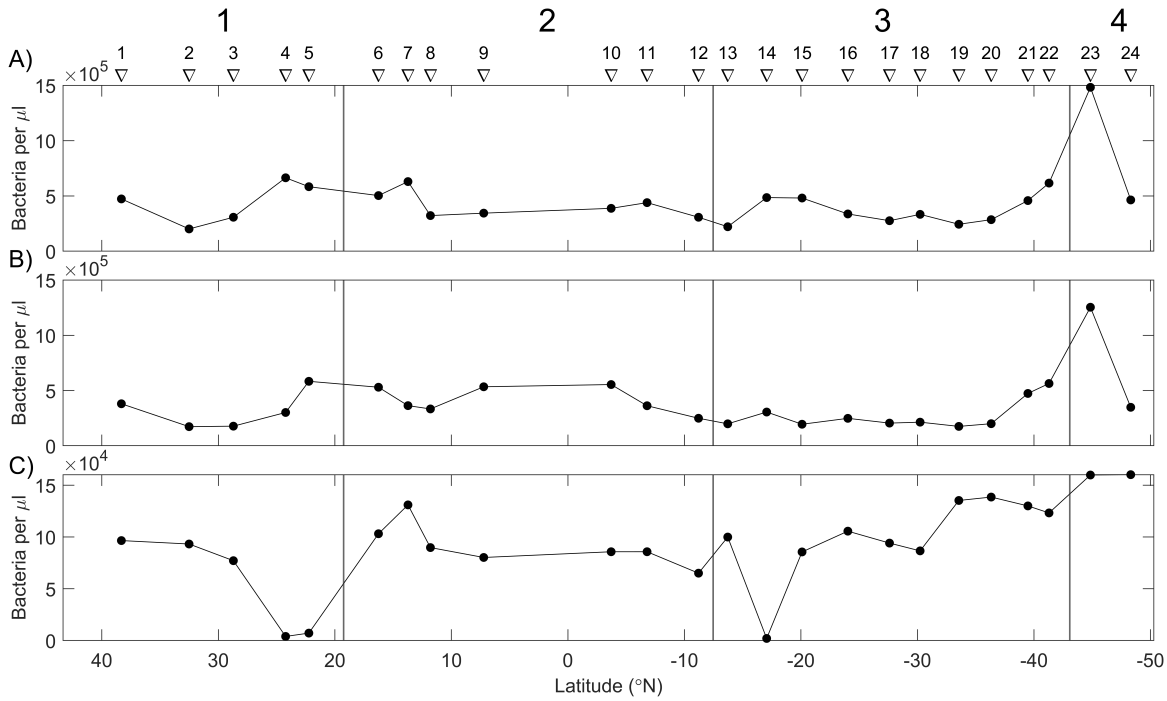

Figure 4.24: Heterotrophic bacteria at A) sea surface, B) chl max depth, and C) at 200 m. Note that the Y-scale changes between panels. The different regions are divided by the black vertical lines with the region number on top. The locations of the CTD stations are displayed on top of the figure.

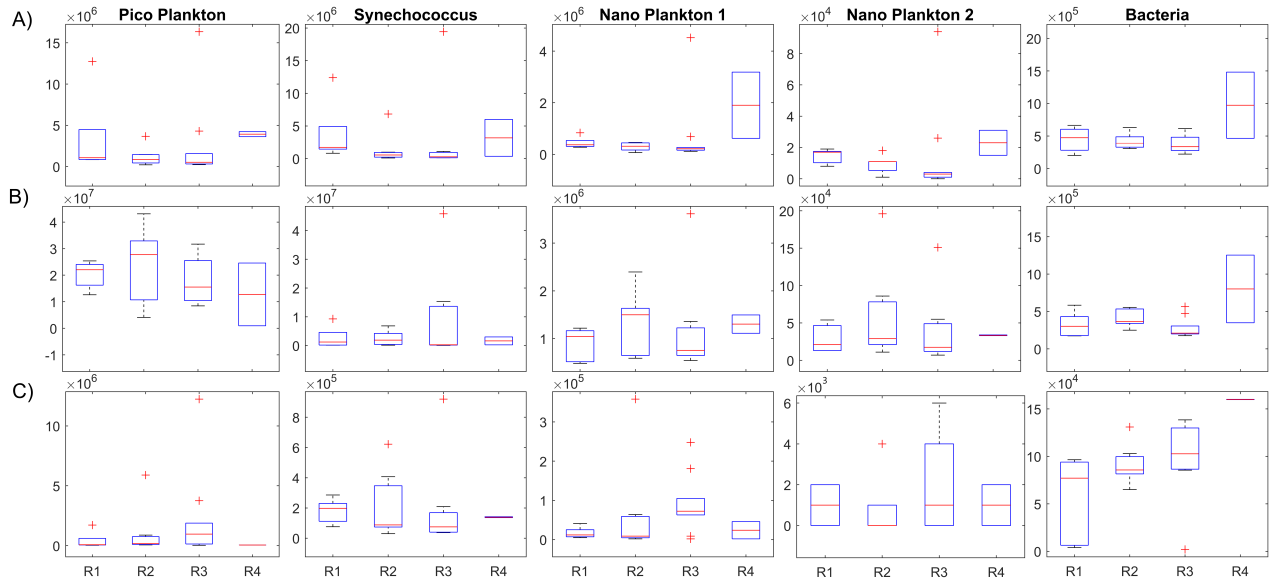

Figure 4.25: Box plot of organic picoplankton, synechococcus, nanoplankton 1 and nanoplankton 2 at A) sea surface, B) chl max depth and C) at 200 m in the different regions. Note that the Y-scale varies across panels.

Chapter 5

Discussion

For the discussion section, some of the results presented in section 4 will be analyzed further to investigate the biochemical properties of the Atlantic Ocean. For this, three main topics were chosen: the controls on the particulate elemental ratio, the controls on fCO_2 over time and the controls on $\delta PO^{13}C$.

5.1 Controls on the Particulate Elemental Ratio

Several mechanisms in the ocean may affect the particulate elemental ratio of primary producers. In this section, the three hypotheses describing this variation represented by (Garcia et al., 2018) will be tested to determine the cause for the latitudinal variations in the euphotic zone: the nutrient supply hypothesis, the allometric diversity hypothesis, and the temperature hypothesis (described in section 2.2).

When considering elemental ratios, it is important to consider that despite numerous studies on the variability, there is no easy way to separate the direct cause because these hypotheses strongly co-vary in the ocean (Garcia et al., 2018). Also, the particulate nutrients are not only composed of organic matter; they may be, among other things, dead cells or inorganic matter, which may have a different elemental ratio as it may not be affected by photosynthesis or remineralization. As the interest of this section is to examine the particulate ratio of primary producers, only the measurements at sea surface and the depth of chl max is used.

5.1.1 The Nutrient Supply Hypothesis

The nutrient supply hypothesis suggests that the inorganic nutrient availability may control the amount of the given nutrient in particulate form (explained in section 2.2). This means if the nutrient limitation is the dominating controller on the particulate elemental ratio, C:N will decrease with increasing NO_3^-, while C:P will decrease with increasing PO_4^{3-}. A way to study this hypothesis is to compare the C:N ratio to the NO_3^- concentration, and the C:P ratio to the PO_4^{3-} concentration, as shown in figure 5.1 and 5.2.

The assimilation and storing of nutrients are energy demanding in nutrient-depleted environments. Therefore, primary producers have a high C:P(N) when the PO_4^{3-} (NO_3^-) concentrations are low. As the nutrient concentration increases, the cost of the storing and assimilate them decreases, which results in a lower C:P(N). This is investigated by Galbraith and Martiny (2015), who showed that the C:N ratio decreases over the range of 0-3 μM of NO_3^-, and then remains relatively constant, while C:P decreases linearly with the PO_4^{3-} concentrations. This means that the NO_3^- concentration affects the C:N ratio at low NO_3^- concentrations but not high, while the PO_4^{3-} concentration may affect the C:P at any concentration. Following Galbraith and Martiny (2015) results, the NO_3^- concentrations are assumed to be the controlling factor on C:N if the concentration is below 3 μmolkg^{-1}, C:N decreases with increasing concentration, and the population correlation coefficient is significantly high at a significance level of 95%. While the PO_4^{3-} concentration is assumed to be the controlling factor on C:P if C:P decreases with increasing concentration and the correlation coefficient is significantly high at a significance level of 95%.

For the entire transect, C:N is decreasing with increasing NO_3^- till approximately 3 μmolkg$^-$1, and C:P is decreasing with increasing PO_4^{3-}. However, the population coefficient is not significantly high for either(figure 5.1 and table 5.1). This indicates that nutrient hypothesis may be the controlling factor on the C:N and C:P ratio in the Atlantic Ocean, but it is not possible to say with certainty.

In regions 1 and 2, C:N is decreasing with increasing NO_3^-, and the population correlation coefficients are significantly high. This indicates that the NO_3^- concentration controls the C:N in these regions. In region 3, C:N is decreasing with increasing NO_3^-, however, the population correlation coefficient is not significantly high. This indicates that the NO_3^- concentration may control the C:N, however, this is without certainty. In region 4, C:N is increasing with increasing NO_3^-, and the population correlation coefficient is not significantly high. This indicates that NO_3^- does not control C:N in region 4 (figure 5.2 and table 5.1).

In region 1, C:P is increasing with increasing PO_4^{3-}, and the population correlation coefficient is not significantly high. This indicates that the PO_4^{3-} concentration is not controlling the C:P in region 1. In regions 2 and 4, C:P is decreasing with increasing PO_4^{3-}, however, the population correlation coefficients are not significantly high. This indicates that the PO_4^{3-} concentration may control the C:P in regions 2 and 4, however, this is without certainty. In region 3, C:P is decreasing with increasing PO_4^{3-} concentration, and the population correlation coefficient is

significantly high. This indicates that the PO_4^{3-} concentration controls the C:P in region 3 (figure 5.2 and table 5.1).

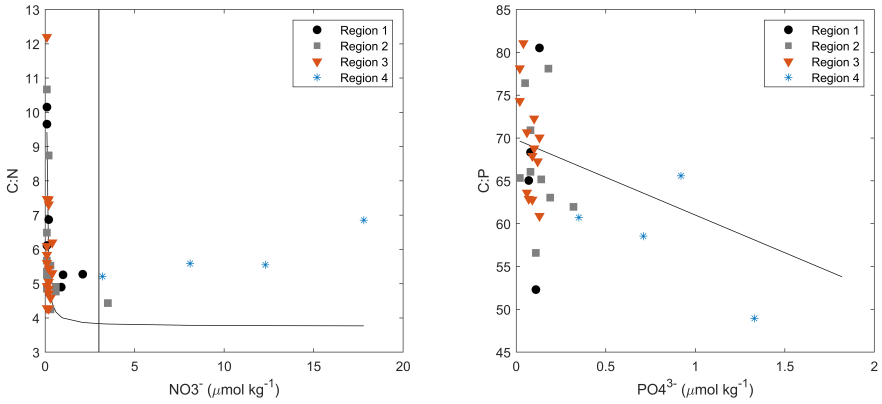

Figure 5.1: Relationship between C:N and NO_3^- and C:P and PO_4^{3-} for the entire transect (black circles are region 1, gray squares are region 2, red triangles are region 3, and blue star are region 4). The black line in the panels on the left side show a hyperbolic approximation, while in the panels on the right side show a linear regression line. The vertical gray line is the 3μmolkg$^-1$ concentration.

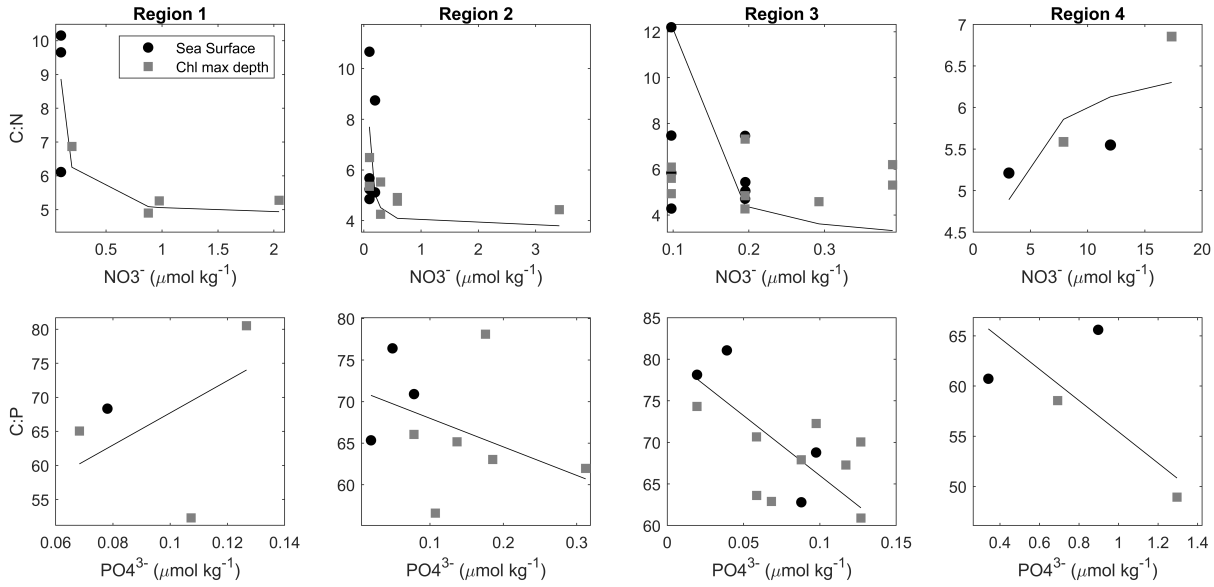

Figure 5.2: Relationship between C:N and NO_3^- and C:P and PO_4^{3-} for samples at sea surface (black) and chl max depth (gray) in the different regions. The black line in the upper panels show a hyperbolic approximation, while in the lower panels it is a linear regression line. The scales of the panles differ to better show the trend in the data in the differen regions.

Table 5.1: Equations of the linear and hyperbolic approximation in figure 5.2 for the different regions where m is the slope, b is the Y-intercept, n is 1/b and k are m×n with the standard deviations. ρ is the population correlation coefficient

Region	C:N = $\frac{n\times NO_3^-}{k+NO_3^-}$	Correlation Coefficient	Is ρ significantly different from 0
All	m = -0.02±0.00, b = 0.27±0.02	R = -0.36	No
1	m = -0.01±0.00, b = 0.21±0.02	R = -0.85	Yes
2	m = -0.01±0.00, b = 0.27±0.03	R = -0.46	Yes
3	m = -0.03±0.01, b = 0.37±0.05	R = -0.24	No
4	m = 0.17±0.09, b = 0.15±0.02	R = 0.72	No
Region	C:P=m×PO_4^{3-} + b	Correlation Coefficient	Is ρ significantly different from 0
All	C:P = -8.8±2.6PO_4^{3-} + 69.8±1.6	R = -0.32	No
1	C:P = 236.2±301.9PO_4^{3-} + 44.1±29.6	R = 0.30	No
2	C:P = -34.3±29.3PO_4^{3-} + 71.4±4.5	R = -0.23	No
3	C:P = -144.3±42.4PO_4^{3-} + 80.4±3.6	R = -0.59	Yes
4	C:P = -15.6±10.5PO_4^{3-} + 71.0±9.2	R = -0.61	No

5.1.2 The Temperature Hypothesis

The temperature hypothesis suggests that temperature controls the C:P and N:P ratios. This hypothesis bases on how temperature may affect the organic N:P or C:P directly because the need for P is temperature-dependent on a cellular level. In high temperatures, the protein-producing ribosomes (which has a high P concentration) work more efficiently than in low temperatures. This means that primary producers in high temperatures need fewer ribosomes than in low temperatures, and consequently, contain a lower concentration of P (Garcia et al., 2018). In other words, the temperature may be controlling the elemental ratios if C(N):P increase with temperature. The temperature may also contribute to a change in the nutrient supply by altering stratification, which ultimately affects the C:P. In higher latitudes, increased temperature will increase the stratification due to ice melting and heating of the top layer. While at lower latitudes, temperature increase may increase the salinity and consequently weaken the stratification (Laufkotter et al., 2015).

This hypothesis is studied by plotting the C:P and N:P vs. temperature (figure 5.4), where the temperature hypothesis is dominant if C:P and N:P increases with temperature and the population correlation is significantly high at a significance level of 95%. Both C:P and N:P are considered because the particulate C is by far more abundant than N and P, which gives a more normalizing factor when considering the elemental ratios (Galbraith and Martiny, 2015). Whereas particulate N may also be a limiting nutrient as particulate P, and studies have shown that higher N:P because of increasing temperatures due to global warming may cause more N-limitations in the future

(Toseland et al., 2013).

Over the entire transect, both C:P and N:P increases with increasing temperatures, however, the population correlation coefficient is not significantly high (figure 5.3 and table 5.2). This indicates that the temperature may control C(N):P in the Atlantic Ocean, but it is not possible to say with certainty.

In region 1, C:P decreases with increasing temperatures, however, the population correlation coefficient is significantly high. This indicates that the temperature does not control C:P in region 1. In regions 2 and 4, C:P is increasing with increasing temperatures, however, the population correlation coefficients are not significantly high. This indicates that the temperature may control C:P in regions 2 and 4 but cannot be said with certainty. In region 3, C:P is increasing with increasing temperatures, and the population correlation coefficient is significantly high. This indicates that the temperature controls C:P in region 3 (figure 5.4 and table 5.2).

In region 1, N:P is increasing with increasing temperature, however, the population correlation coefficient line is not significantly high. Given the low correlation coefficient, this indicates that the temperature does not control N:P in region 1. In region 2, N:P is decreasing with increasing temperature, and the population correlation coefficient is not significantly high. This indicates that temperature does not control N:P in region 2. In regions 3 and 4, the N:P increases with increasing temperature, and the population correlation coefficients are significantly high. This indicates that the temperature controls the N:P in region 3 and 4 (figure 5.4 and table 5.2).

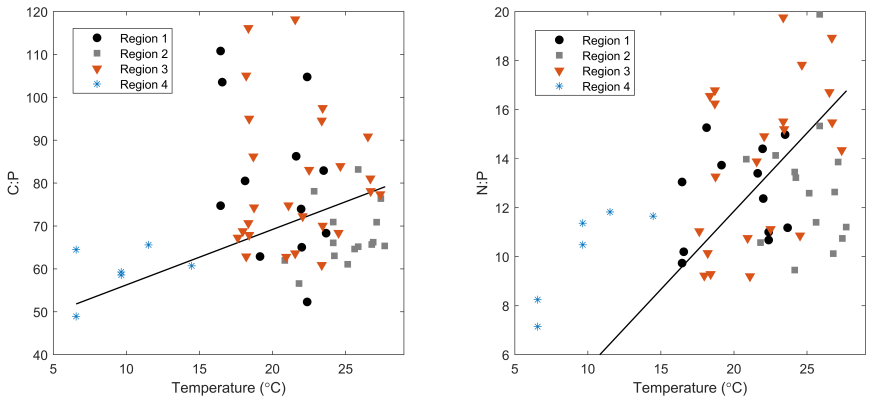

Figure 5.3: The relationship between C:P and temperature, and N:P and temperature over the entire transect (black circles are region 1, gray squares are region 2, red triangles are region 3, and blue star are region 4). The black line is a linear regression line.

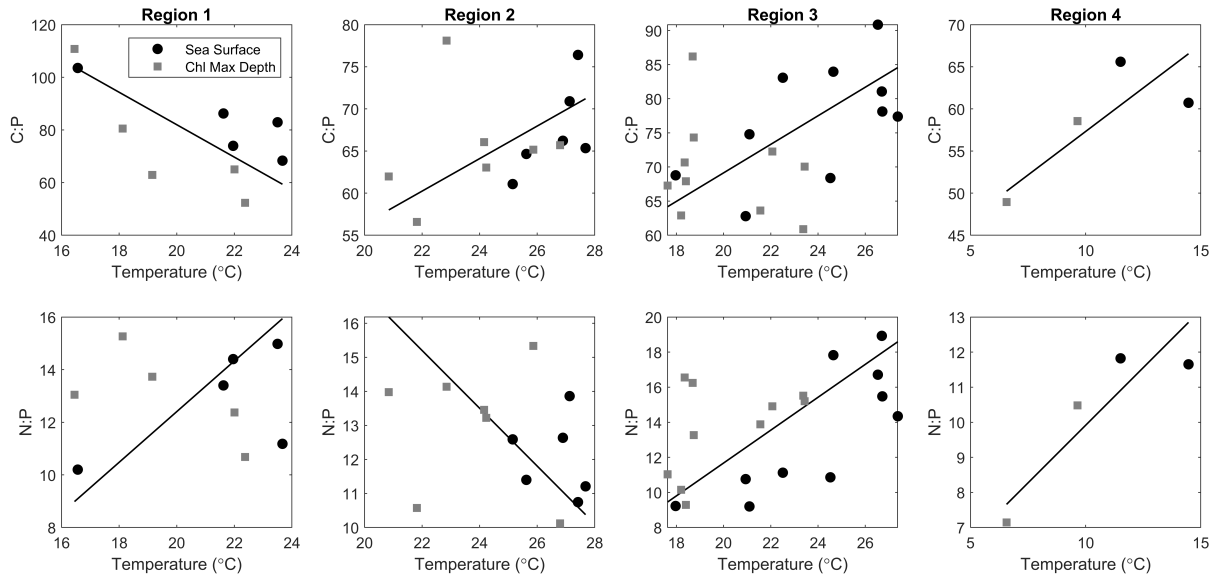

Figure 5.4: The relationship between C:P and temperature, and N:P and temperature at the sea surface (black circles) and the chl max depth (gray squares) in the different regions. The black line is a linear regression line. The scales of the panels differ to better show the trend in the data in the different regions.

Table 5.2: Equations of the regression lines in figure 5.4 for the different regions where m is the slope ± the standard deviation , b is the Y-intercept ± the standard deviation and T is the temperature. ρ is the population correlation coefficient

Region	C:P=mT + b	Correlation Coefficient	Is ρ significantly different from 0
All	C:P = 1.3±0.4T + 43.3±8.8	R = 0.12	No
1	C:P = -6.2±1.9T + 205.2±38.5	R = -0.67	Yes
2	C:P = 1.9±0.8T + 17.7±20.6	R = 0.34	No
3	C:P = 2.1±0.6T + 27.3±13	R = 0.45	Yes
4	C:P = 2.1±1T + 36.7±10.9	R = 0.77	No
Region	N:P=mT + b	Correlation Coefficient	Is ρ significantly different from 0
All	N:P = 0.6±0.1T - 0.9±2.1	R = 0.40	No
1	N:P = 1±0.4T - 6.9±8.3	R = 0.04	No
2	N:P = -0.8±0.3T + 33.9±7.2	R = -0.28	No
3	N:P = 0.9±0.2T - 7.1±4.7	R = 0.54	Yes
4	N:P = 0.7±0.2T + 3.3±2.4	R = 0.89	Yes

5.1.3 The Allometric Diversity Hypothesis

The allometric diversity hypothesis suggests that the C:P and N:P depend on the size and growth rate of different plankton groups. Larger, fast-growing plankton contains more ribosomes (with high P concentrations), as they need a higher protein production than smaller plankton. That is, C:P and N:P decreases with increasing growth-rate and size. Preferably the elemental ratio would be compared to the size fractionation of the particulate element, but as these measurements were not done, the ratios will be compared to the pico- and nanoplankton abundance. As pico and nanoplankton were categorized using their cell diameter, it can give an indication to the hypothesis. However, the elemental ratio of these plankton groups is not only controlled by their size. For example, is the elemental ratio of picoplankton known to be highly affected by the nutrient supply, which may overwrite the effect of growth rate (Pitta et al., 2016).

In regions 1 and 3, C:P and N:P are high, and there is a high abundance of picoplankton and synechoccus (<2μm), which may indicate that the low C:P and N:P is due to the size and growth-rate. In region 2, C:P and N:P is low, but picoplankton and synechoccus are the most abundant groups. This indicates that C:P or N:P is not caused by the size and growth rate in the region 2. In region 4, C:P and N:P are low, and there is assumed to be a diatom abundance. Diatoms are fast-growing big plankton, which means that the C:P and N:P in region 4 may be caused by diatom in the region.

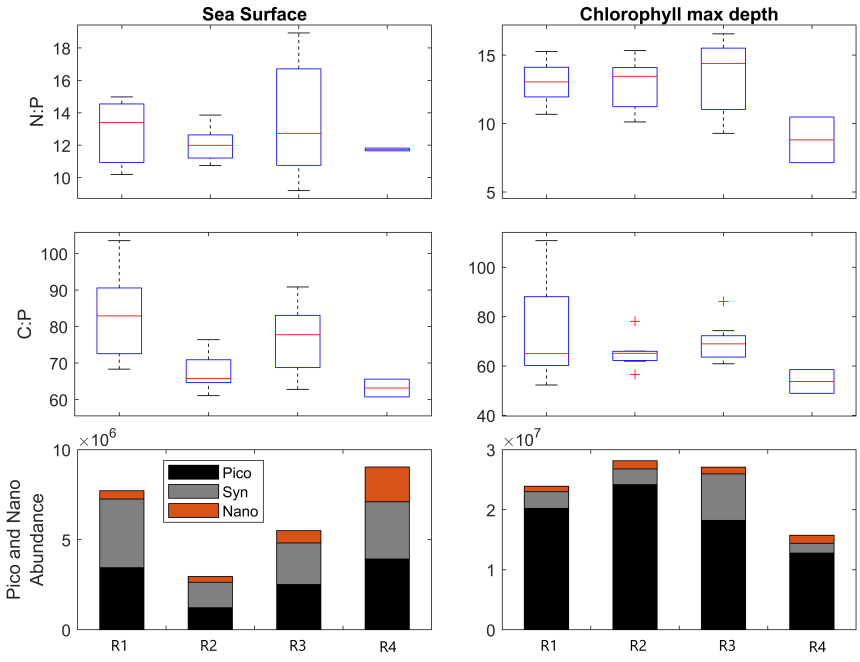

Figure 5.5: Box plot of N:P and C:P, and a bar graph of picoplankton, synechoccus and nanoplankton in the different regions.

5.1.4 Summary

The result of the different hypothesis tests is shown in table 5.3, divided into the different regions and over the transect as a whole. This shows that there are regional differences and that the different hypothesizes often co-vary.

Over the entire transect, nutrient limitation and temperature are both possible main controllers of the C:N and C:P ratio, however, the population correlation is not significant for any of these. As there are clear regional differences (table 5.3), it is likely that the change in the elemental ratio is a combination of the hypothesizes.

Region 1 is in the subtropics, where nutrient concentrations are low. The results presented here show that the C:N ratio is positively and significantly correlated with the NO_3^- concentration (table 5.3). This suggests that the nutrient limitation hypothesis is correct for C:N. For PO_4^{3-}, on the other hand, no clear conclusions can be drawn, but if any, temperature seems to be the driver of C:P variations, as this is the only factor that shows a correlation - but it is not significant (table 5.3). However, figure 4.13 suggests there are nitrogen fixers in this region, which is common in subtropical regions (Sarmiento and Gruber, 2006). Nitrogen fixers have a lower C:N than the Redfield ratio, as such, these may also be contributing to the low C:N. They may also be the cause for the N:P variations with temperature. Nitrogen fixers have a low N:P and are most abundant in the sea surface where the temperatures are highest. The subtropical region is commonly most abundant in small plankton groups, such as picoplankton. The small size of the picoplankton may contribute to the low C:P and N:P, however, picoplankton is known to have high elemental ratio plasticity. Therefore, the nutrient limitation overwrites the effect of the size and growth-rate of the picoplankton.

Region 2 is in the equatorial region but is nutrient depleted as the considered measurements were collected above the thermocline. The NO_3^- concentration was causing variations in C:N, while the variations in C:P is likely caused by a combination of the PO_4^{3-} concentration and the temperature. In this region, there was no evidence of nitrogen fixation (section 4.3), which strengthens the finding that the C:N variations are mainly caused by the NO_3^- concentration.

Region 3 is in the subtropics, as region 1, where there is nutrient limitation, however, there is no evidence of nitrogen fixation by the N* (section 4.3). The C:P is controlled by both the PO_4^{3-} concentration and the temperature, while the N:P is controlled by temperature. The C:P ratio significantly decreased with increasing PO_4^{3-} concentrations (figure 5.2 and table 5.3); which strongly suggest that phosphate concentrations are the diver of variations in C:P. As there are no nitrogen fixers in this region, it supports the assumption that the NO_3^- concentration controls C:N. The trend between size and growth-rate and C:P and N:P is not valid for the same reasons as in region 1.

Region 4 is in the BMCZ, which is nutrient-rich, cold, has a high diatom abundance. The NO_3^- concentrations

are too high in this region to affect the C:N, while the PO_4^{3-} concentration might control C:P. The assumed presence of diatoms (figure 4.18 and 4.5) indicates that their large size and fast growth-rate control C:P and N:P, while the temperature indicates to control the C:P and N:P. However, because the C:P and N:P is overall low, the presence of diatoms is probably the main controller. Other studies have shown that both diatoms size and growth-rate and the low temperatures cause low C:P and N:P in the Southern Ocean, which gives reason to believe that this effect is present in region 4 (Galbraith and Martiny, 2015; Toseland et al., 2013).

Table 5.3: Summary of the controls on particular elemental ratios. If there are two symbols, the first +/- symbol represents the slope, which is + when the slope is as expected, and - if not. The second +/- symbol represents the significance of the population correlation coefficient, which is + when the correlation is significantly higher than 0, and - when the correlation is not significantly higher than 0. If there is one symbol; it represents the trend, which is + when there is a clear trend, (+) if there is a possible trend, and - if there is no trend.

	All	Region 1	Region 2	Region 3	Region 4
C:N - NO_3^-	+ -	+ +	+ +	+ -	- -
C:P - PO_4^{3-}	+ -	- -	+ -	+ +	+ -
C:P - Temp	+ -	- +	+ -	+ +	+ -
N:P - Temp	+ -	+ -	- -	+ +	+ +
C:P - Size	-	(+)	-	(+)	+
N:P - Size	-	(+)	-	(+)	+

5.2 Change in fCO_2 Between 1991-2018

In this section the fCO_2 data collected at the cruise will be compared to data from 1991, 1995 and 2013 (table 5.4 and figure 5.6), retrieved from SOCAT (Bakker et al., 2016). Further, the factors (temperature, TA, or DIC) responsible for the changes in fCO_2 over the given timeframe will be identified. These particulate datasets were chosen because the cruises followed approximately the same route, they are all from north to south and were conducted between October and December (table 5.4 and figure 5.6).

Table 5.4: List of research cruises

Vessel	Year	Date	Expocode
Polarstern	1991	14.11-09.12	06AQ19911114
James Clark Ross	1995	02.10-24.10	74JC19951003
James Clark Ross	2013	09.10-03.11	74JC20131009
Kronprins Haakon	2018	01.12-03.01	KPH2018716

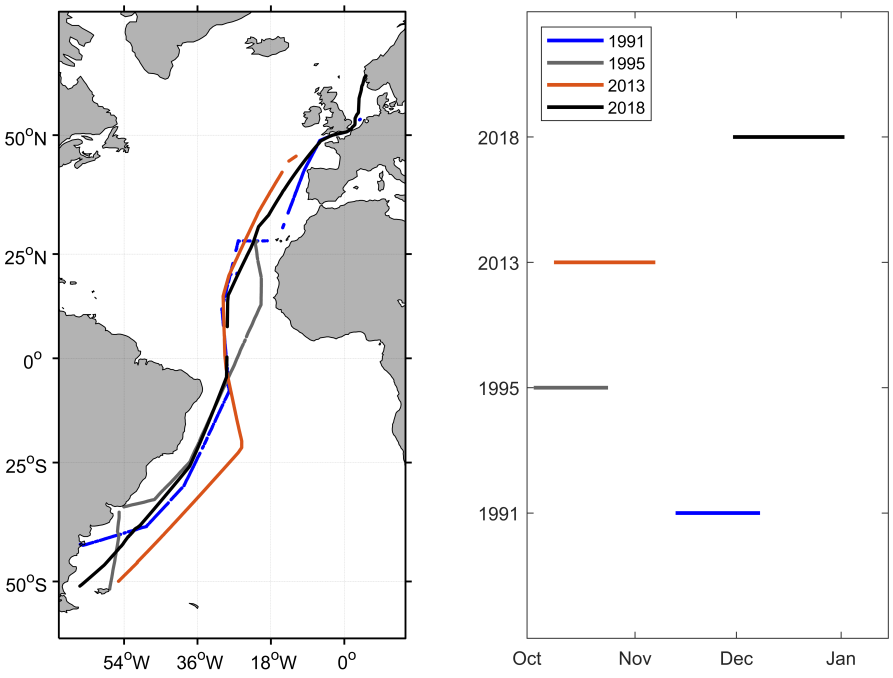

Figure 5.6: Map of the transects and the monthly coverage of the cruises in 1991 (blue), 1995 (gray), 2013 (red), and 2018 (black).

5.2.1 Time Trend of Temperature, fCO_2, TA and DIC

Figure 5.7 show how the temperature, fCO_2, TA and DIC changed between 1991, 1995, 2013 to 2018. Since 1991 the global ocean temperature anomaly in December has increased from 0.34°C to 0.72°C (NOAA, 2019a), while the atmospheric CO_2 levels have increased from 354 ppm to 408 ppm (Dlugokencky and Tans, 2019). Consequently, an increase in temperature, fCO_2, and DIC is expected over this timeframe. However, the temperature is also highly dependent on the season. Therefore it is reasonable that the temperature in 1995 and 2013 are warmer than in 2018 north of the equator as these cruises were conducted earlier in the fall (figure 5.7 and 5.7). The season can also explain why the temperatures in 1995 and 2013 are colder than 2018 south of the equator, although this is also expected from global warming. On the other hand, the temperatures in 1991 are overall higher than in 2018 north of the equator, even though it was conducted at approximately the same time of the year. A definite signal of global warming is, therefore, not present in these data. This could be caused by the interannual variations caused by, e.g., El Niño events (NOAA, 2019b), however, this is not of any relevance for the issues discussed in this section.

The fCO_2 values from 1991 and 1995 are, on average, the lowest, while fCO_2 from 2013 is higher than in 2018 to the north of the equator and lower to the south (figure 5.7B). The fCO_2 in 2018 shows a clear difference between north and south of the equator. This difference likely arises because the cruise was conducted during December

when the temperature difference between the hemispheres is high (summer vs. winter). The fCO_2 data from 2013, however, were collected in October, when the temperature difference expected to be lower than in December (fall vs. spring) (figure 5.7A). The DIC values in 1991 and 1995 are, on average lower than in 2013 and 2018, while the values in 2013 and 2018 are fairly similar (figure 5.7D). For TA, the differences between the years are overall very small, reflecting low variations in salinity (which as used to calculate TA) (figure 5.7C).

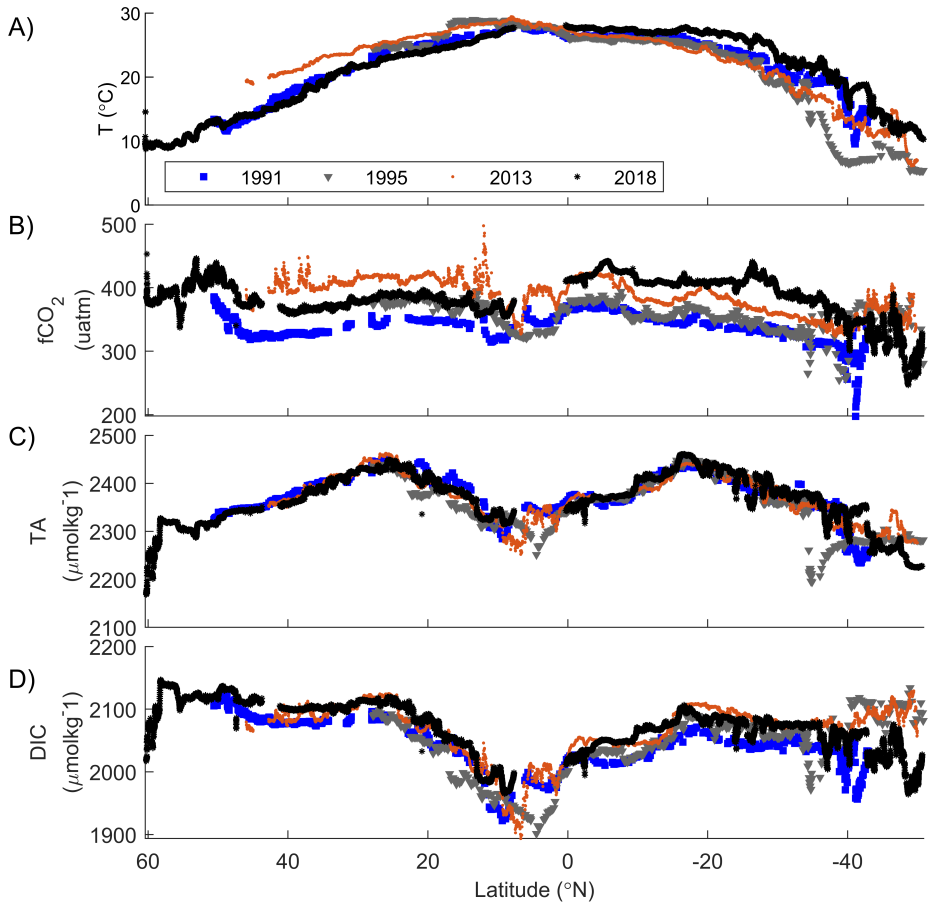

Figure 5.7: a) Temperature b) fCO_2, c) TA and d) DIC from 1991 (blue), 1995 (gray), 2013 (red) and 2018 (black) obtained from, or calculated using data from, SOCAT and pCO_2 measuring system.

5.2.2 Controls on fCO_2 Change Between 1991-2018, 1995-2018 and 2013-2018

Temperature, TA and DIC all affect the fCO_2 (section 2.3). In this section, the importance of the fCO_2 changes between 1991-2018, 1995-2018 and 2013-2018 is determined using calculations of the carbonate system

The following calculations were carried out to obtain the results in figure 5.8: The effect of temperature change was determined by using TA and DIC from 1991/1995/2013 and temperature 2018, the resulting fCO_2 is the fCO_2

for 1991/1995/2013 if the temperature whereas in 2018. If fCO_2 for the new calculated result and the measured from 2018 is the same, the temperature difference between 1991/1995/2013 and 2018 is the dominating controlling factor. The effects of DIC and TA were calculated using the same principle. The effect of DIC was determined by calculating fCO_2 with TA and temperature from 1991/1995/2013 and DIC from 2018, and the effect of TA was determined by calculating fCO_2 with DIC and temperature from 1991/1995/2013 and TA from 2018. DIC or TA is the dominating controlling factor of the fCO_2 change if the calculated fCO_2 is similar to the 2018 measured value.

The fCO_2 in 2018 was higher than in 1991 over the entire transect, and the latitudinal trends similar. The difference is lower north of the equator than south. This fits with the temperature difference; the 2018 temperature is lower than in 1991 north of the equator (figure 5.7). However, the temperature differences between 1991 and 2018 are quite small, which gives reason to assume that this is not the cause for the fCO_2 change (figure 5.7). This is confirmed by figure 5.8, where the calculated 1991 fCO_2 using the temperatures from 2018 and the measured values from 2018 are dissimilar. The 1991 fCO_2 calculated using TA from 2018, is not similar to the measured values from 2018 either (figure 5.8). This is as expected because the TA is not changing much over the timeframe. The DIC in 1991, however, was lower than in 2018, and the fCO_2 values calculated using 1991 temperatures and TA but 2018 DIC are similar to the measured 2018 values (figure 5.8). Therefore, the DIC increase was the cause of the fCO_2 increase between 1991 and 2018. As the two cruises were conducted at the same time of the year, it is reasonable that the influence of natural processes, such as primary production and seasonal in/outgassing on the DIC difference is small. Likely, the DIC and fCO_2 have increased as a direct consequence of the increased uptake of atmospheric CO_2.

The fCO_2 in 2018 is higher than the 1995 fCO_2 between ~10°N and ~40°S. The fCO_2 values calculated using the 1995 DIC and TA, but 2018 temperatures are fairly similar to the 2018 measured values in this area. This shows that the temperature increase is the reason for fCO_2 change, in particular, south of 20°S. The 1995 fCO_2 calculated using TA from 2018, is not similar to the measured values from 2018 (figure 5.8). This is expected as it is an even shorter timeframe then 1991-2018. Between 10°N and 20°S increasing DIC appears more important, as here, the fCO_2 determined using 1995 temperatures and TA but 2018 DIC, match the 2018 measured fCO_2 pretty well. The increases DIC could be a result of the time of the year the cruises were conducted, as the solubility of CO_2 is higher in December than October because of the temperature difference. However, as the temperature is fairly constant over the years in equatorial regions, it is reasonable to assume that DIC has increased over the years due to increased uptake of CO_2.

For 2013 to 2018, the fCO_2 values in 2013 are higher than in 2018 north of the equator and lower to the south. As described above, the temperatures north of the equator were higher in 2013, likely because of the timing of the cruises (October 2013 vs. December 2018). This is reflected in figure 5.8 showing the effect of temperature, where the fCO_2 of 2013 is similar to the measured fCO_2 in 2018 if the 2013 temperatures were lowered to those of 2018 (figure 5.8). South of the equator, however, the fCO_2 difference appears to be caused by several factors, but overall,

the low effects of TA and DIC are compensated by warmer temperatures in 2018, which is caused by the timing of the cruises.

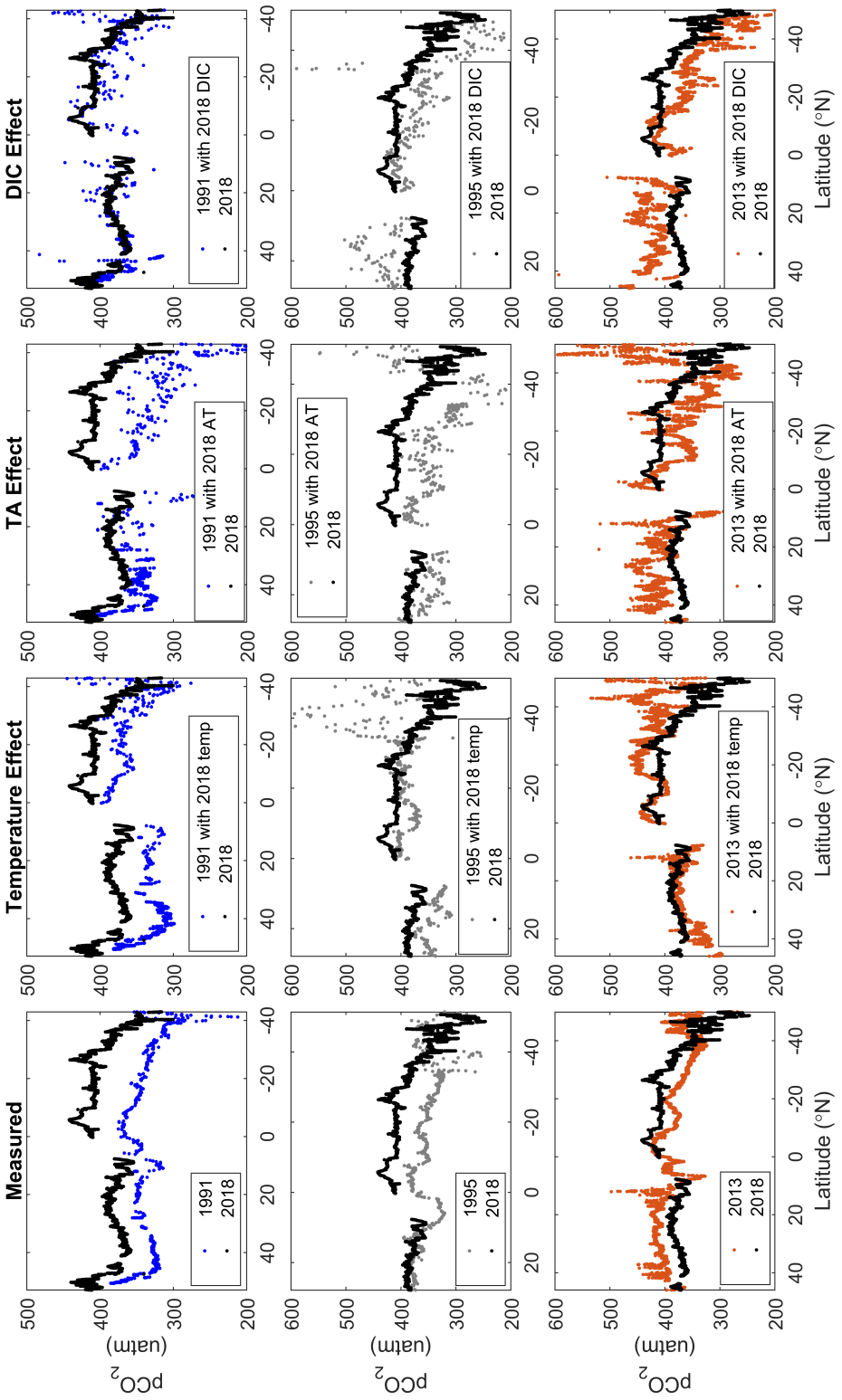

Figure 5.8: The pCO_2 measured in 2018 (black), and pCO_2 in 1991/1995/2013 (red), which is either the measured values or calculated to show effect of temperature, DIC or TA.

5.3 Controls on $\delta PO^{13}C$

Several processes in the carbon cycle cause isotopic fractionation, which alters the organic and the inorganic $\delta^{13}C$ ratios in the ocean, such as photosynthesis and air-sea gas exchange (section 2.4). In section 4.6, the latitudinal trend of $\delta DI^{13}C$ was found to be caused by mainly biology, thermodynamic effect, and the ^{13}C Suess effect. However, the causes for the latitudinal changes in $\delta PO^{13}C$ remained unclear. In this section, the factors controlling the latitudinal variations in $\delta PO^{13}C$ shown in figure 4.14 will be investigated. The potential factors are: the Rayleigh effect, the thermodynamic effect, the $CO_{2(aq)}$ concentration and the growth rate (these are further described in section 2.4). Note that only regions 1, 2, and 3 are investigated due to the lack of $\delta PO^{13}C$ measurements in region 4. Determining the direct cause for the isotopic fractionation by investigating the isotopic ratios is difficult. As shown in figure 4.17 the $\delta PO^{13}C$ and $\delta DI^{13}C$ correlate, which indicates that factors that initially only affect $\delta DI^{13}C$, may also affect $\delta PO^{13}C$.

5.3.1 Primary Production and Rayleigh Effect on $\delta PO^{13}C$

Primary producers have a lighter carbon pool than DIC as they prefer ^{12}C over ^{13}C. During a bloom, this will cause the $\delta DI^{13}C$ to increase. However, an increase in $\delta DI^{13}C$ will, in turn, also cause an increase in $\delta PO^{13}C$ as the bloom proceeds. (described in section 2.4). This could explain the correlation between $\delta PO^{13}C$ and $\delta DI^{13}C$ in figure 4.17. However, the Rayleigh effect will only occur in areas where the CO_2 concentrations are low, which is only the case during intense blooms. As this was not the case for any of the given regions (given by figure 4.18 or 4.19), the Rayleigh effect is not responsible for the latitudinal difference in $\delta PO^{13}C$.

5.3.2 Thermodynamic Effect on $\delta PO^{13}C$

Equilibrium fractionation, which is the fractionation occurring in equilibrium reactions, depends on temperature (section 2.4). The inorganic carbon chemistry is an example of equilibrium reactions, and two of these temperature-dependent reactions are: 1) the air-sea gas exchange and 2) the distribution of carbon isotope ratios across the species that make up the DIC pool. 1) Air-sea gas exchange results in higher $\delta DI^{13}C$ in colder waters and lower $\delta DI^{13}C$ in warmer waters. 2) The $[CO_{2(aq)}]$ part of the DIC pool has lower $\delta^{13}C$ in colder waters and a higher $\delta^{13}C$ in warm water.

An interesting feature of figure 4.14 was that the latitudinal trend of organic $\delta PO^{13}C$ indicates that the $\delta PO^{13}C$ increase with temperature. However, the temperature effect on the fractionation occurring during photosynthesis (ϵ_p) is very low. One possible explanation for this feature could then be that the temperature dependence of the

DIC - [$CO_{2(aq)}$] fractionation controls $\delta PO^{13}C$ through the [$CO_{2(aq)}$] assimilation by autotrophs. This could then explain the correlation in figure 4.17. In the following, the effects of fractionation during air-sea gas exchange, DIC-[$CO_{2(aq)}$], and primary production will be determined, to evaluate if any of these or a combination can explain the observed relationship between $\delta DI^{13}C$ and $\delta PO^{13}C$.

First, the fractionation during air-sea gas exchange ($\epsilon_{(DIC-^{13}CO_{2(g)})}$) is calculated using Eq. 2.10 (figure 5.9B). As the variations in atmospheric $\delta^{13}C$ are much smaller than the here discussed changes in the isotope ratio of DIC, we assume the atmospheric $\delta^{13}C$ to be constant at -8 ‰(figure 5.9A) (Eide et al., 2017). If the thermodynamic effect is the dominating controller on $\delta DI^{13}C$ at the surface (where air-sea exchange occurs), it should have a similar trend to figure 5.9B. However, the $\delta DI^{13}C$ shows an opposite trend (figure 5.9C). This gives reason to believe that the thermodynamic effect on the air-sea gas exchange is not the cause for the latitudinal trend of $\delta DI^{13}C$ and, consequently, do not affect the latitudinal trend of $\delta PO^{13}C$. As argued in section 4.5, the $\delta DI^{13}C$ trends are mostly controlled by a combination of biological production and the ^{13}C Suess effect.

Further, the thermodynamic effect on the DIC - [$CO_{2(aq)}$] pool is studied by calculating the fractionation factor between DIC and [$CO_{2(aq)}$] ($\epsilon_{(DIC-^{13}CO_{2(aq)})}$) using Eq. 2.12 (figure 5.9D). This is next used to calculate $\delta^{13}CO_{2(aq)}$ using Eq.2.13 (figure 5.9E). The resulting $\delta^{13}CO_{2(aq)}$ follows mainly the temperature trend given by the $\epsilon_{(DIC-^{13}CO_{2(aq)})}$ as expected.

The possible thermodynamic effect on $\delta PO^{13}C$ is investigated, by calculating the fractionation occurring during carbon fixation (ϵ_p) using Eq. 2.9. If $\delta^{13}CO_{2(aq)}$ and $\delta PO^{13}C$ have a similar shape, while $\delta PO^{13}C$ and ϵ_p are not, it is the $\delta^{13}CO_{2(aq)}$ that governs the $\delta PO^{13}C$ (figure 5.9E, F and G). If ϵ_p proved to be similar to $\delta PO^{13}C$, the latitudinal trend in $\delta PO^{13}C$ would be caused through the carbon fixation or other processes affecting the particulate matter as respiration.

Firstly, at the sea surface, the temperature effect on the $\epsilon_{(DIC-^{13}CO_{2(aq)})}$ is strong. This results in a latitudinal trend of $\delta^{13}CO_{2(aq)}$ that follows the temperature, which is similar to the $\delta PO^{13}C$ (figure 5.9). The ϵ_p does not have a similar overall latitudinal trend as $\delta PO^{13}C$. This indicates that the latitudinal sea surface trend of $\delta PO^{13}C$ is a result of the temperature dependency of the DIC - [$^{13}CO_{2(aq)}$] isotope fractionation. Secondly, at the chl max depth, the temperature dependency creates a $\delta^{13}CO_{2(aq)}$ trend that follows the temperature, similar to the sea surface. However, at this depth there is almost no similarities between $\delta^{13}CO_{2(aq)}$ and $\delta PO^{13}C$, while $\delta PO^{13}C$ has a similar pattern as the ϵ_p (figure 5.9). This indicates that the $\delta PO^{13}C$ trend at the chl max depth is not a result of the temperature dependency of the DIC - [$^{13}CO_{2(aq)}$] isotope fractionation, but the ϵ_p. Finally, at 200 m, the spatial patterns of $\delta^{13}CO_{2(aq)}$ and $\delta PO^{13}C$ do not match. However, there is no clear connection between ϵ_p and $\delta PO^{13}C$ either (figure 5.9). At 200 m, the particulate matter is also influenced by e.g., respiration. Therefore, the hypothesis that $\delta PO^{13}C$ is determined by the carbon the primary producers assimilated does not hold.

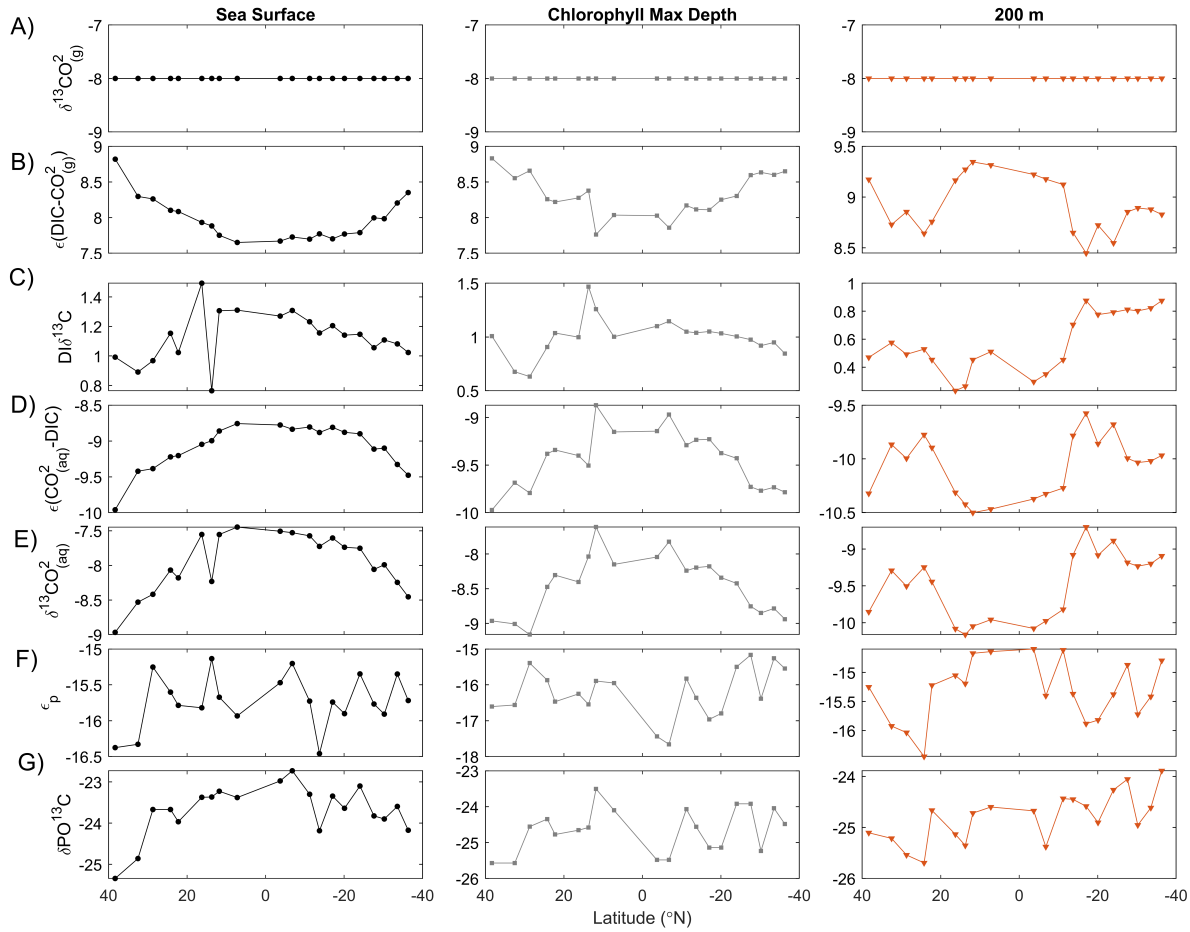

Figure 5.9: A) Average atmospheric $\delta^{13}CO_{2(g)}$, B) calculated $\epsilon_{(DIC-CO_{2(g)})}$, C) measured $\delta DI^{13}C$, D) calculated $\epsilon_{(CO_{2(aq)}-DIC)}$, E) calculated $\delta^{13}CO_{2(aq)}$ F) calculated ϵ_p and E) measured $\delta PO^{13}C$ at the sea surface, the chl max depth and 200 m.

5.3.3 $CO_{2(aq)}$ Concentration Control on $\delta PO^{13}C$

High concentrations of natural $[CO_{2(aq)}]$ in the ocean may result in stronger discrimination against ^{13}C during photosynthesis and consequently lead to a lower $\delta PO^{13}C$ (Tuerena et al., 2019). Therefore, $[CO_{2(aq)}]$ and $\delta PO^{13}C$ should inversely correlate, while $[CO_{2(aq)}]$ and ϵ_p (the fractionation occurring during photosynthesis) should correlate. It is important to consider that this effect is not evident when considering anthropogenic CO_2, because the anthropogenic carbon $\delta^{13}C$ is very low and will overwrite this effect in the $\delta PO^{13}C$.

To evaluate this, $[CO_{2(aq)}]$ was first calculated with CO2sys using the measured TA and DIC then plotted against $\delta PO^{13}C$ and ϵ_p in figure 5.10, for the different regions. $\delta PO^{13}C$ is assumed to be controlled by the $[CO_{2(aq)}]$ concentration if $\delta PO^{13}C$ decreases, and ϵ_p increases with increasing $[CO_{2(aq)}]$ concentrations, and the population correlation is significant at a level of 95%.

In region 1, the relationship between $\delta PO^{13}C$ and $[CO_{2(aq)}]$ is opposite: $\delta PO^{13}C$ increases with $[CO_{2(aq)}]$ (figure 5.10), while the population correlation coefficient for $\delta PO^{13}C$ vs. ϵ_p is not significant (table 5.5). This indicates that the natural $[CO_{2(aq)}]$ does not control the $\delta PO^{13}C$ in region 1. This may be a consequence of the uptake of anthropogenic CO_2, as region 1 is in the subtropics where there is a high concentration of anthropogenic CO_2. Anthropogenic CO_2 has a much lower $\delta^{13}C$ than natural CO_2, which will produce a low $\delta PO^{13}C$ regardless of the natural $[CO_{2(aq)}]$ concentration. This results in low $\delta PO^{13}C$ values at the surface and chl max depth, because of anthropogenic CO_2, and similarly low values at 200 m because of remineralization. In region 2, both $\delta PO^{13}C$ vs. $[CO_{2(aq)}]$and $\delta PO^{13}C$ vs. ϵ_p is as expected and the population correlation is significant (figure 5.10 and table 5.5). Here, the $\delta PO^{13}C$ appears to be controlled by the concentration of $[CO_{2(aq)}]$. As region 3 is in the subtropics, the results are expected to be similar to region 1. This is partly true, but not to the same extent. The ϵ_p vs. $[CO_{2(aq)}]$ relationship has a low correlation, and the difference with depth is small, as in region 1. However, the $\delta PO^{13}C$ vs. $[CO_{2(aq)}]$ relationship has a significantly high population correlation in region 3 (figure 5.10 and table 5.5).

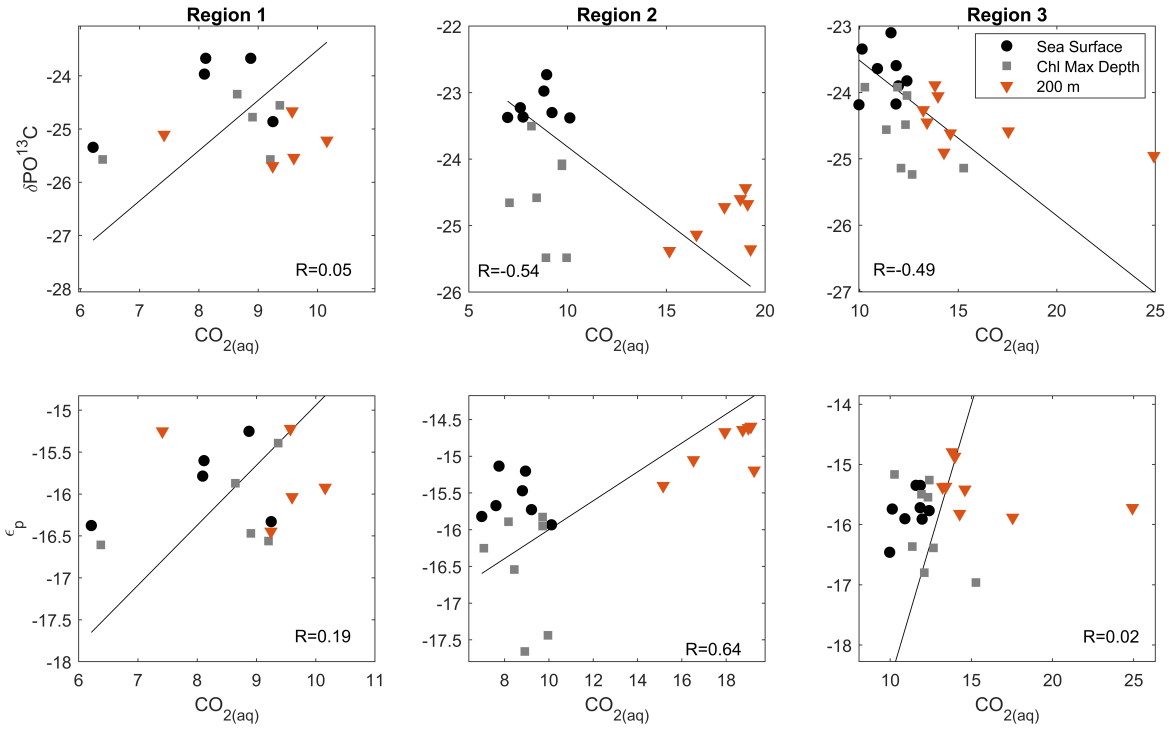

Figure 5.10: $\delta PO^{13}C$ vs. $[CO_{2(aq)}]$ and $\delta PO^{13}C$ vs. ϵ_p at sea surface (black circles), the depth of the chl max (gray squares), and at 200 m (red triangles) in the different regions. The black line is the calculated regression line. The scales of the panles differ to better show the trend in the data in the differen regions.

Table 5.5: Equations of the regression lines in figure 5.10 for the different regions where m is the slope ± the standard deviation, and b is the Y-intercept ± the standard deviation. ρ is the population correlation coefficient

Region	$\delta PO^{13}C$=m[$CO_{2(aq)}$] + b	Correlation Coefficient	Is ρ significantly different from 0
1	$\delta PO^{13}C$ = (0.9±0.3)[$CO_{2(aq)}$] - (33.0±2.5)	R = 0.05	No
2	$\delta PO^{13}C$ = (-0.2±0.0)[$CO_{2(aq)}$] - (21.5±0.6)	R = -0.54	Yes
3	$\delta PO^{13}C$ = (-0.2±0.0)[$CO_{2(aq)}$] - (21.2±0.6)	R = -0.49	Yes
Region	ϵ_p=m[$CO_{2(aq)}$] + b	Correlation Coefficient	Is ρ significantly different from 0
1	ϵ_p = (0.7±0.2)[$CO_{2(aq)}$] - (22.1±1.8)	R = 0.19	No
2	ϵ_p = (0.2±0.0)[$CO_{2(aq)}$] - (18±0.5)	R = 0.64	Yes
3	ϵ_p = (0.9±0.2)[$CO_{2(aq)}$] - (27.7±2.7)	R = 0.02	No

5.3.4 Growth Rate effect on $\delta PO^{13}C$

The size and growth rate of plankton may affect the $\delta PO^{13}C$ because large and fast-growing plankton are not as selective when assimilating CO_2 as smaller, slower-growing plankton. In other words, they do not discriminate as strongly against ^{13}C, which will result in higher $\delta PO^{13}C$ (Tuerena et al., 2019). Similar to the allometric diversity hypothesis, this would preferably be explored using the size fractionation of the particulate C on the filters, but as these measurements were not conducted, the ratios will be compared to the pico- and nanoplankton abundance. As pico and nanoplankton were categorized using their cell diameter, it can give an indication to the hypothesis (Pitta et al., 2016).

Region 1 and 3 are in subtropical regions and dominated by smaller plankton, especially picoplankton, as they are adapted to live in oligotrophic areas (Luis Otero-Ferrer et al., 2018). As picoplankton are <2μm and slow-growing a low $\delta PO^{13}C$ is expected. This is evident at the sea surface, where $\delta PO^{13}C$ in regions 1 and 3 are significantly lower than in region 2 (figure 5.11), which is supported by t-test. However, as there is an uptake of anthropogenic CO_2 (with very low $\delta^{13}C$) in regions 1 and 3, this may result in a low $\delta PO^{13}C$ regardless of the growth rate. It is, therefore, impossible to determine if the size and growth-rate are responsible for the low $\delta PO^{13}C$ in regions 1 and 3. In region 2 there is no evidence of large fast-growing plankton by figure 5.11, however the $\delta PO^{13}C$ is high. The size and growth rate are therefore assumed not to affect the $\delta PO^{13}C$ in region 2. However, the results may be caused by plankton groups that were not measured.

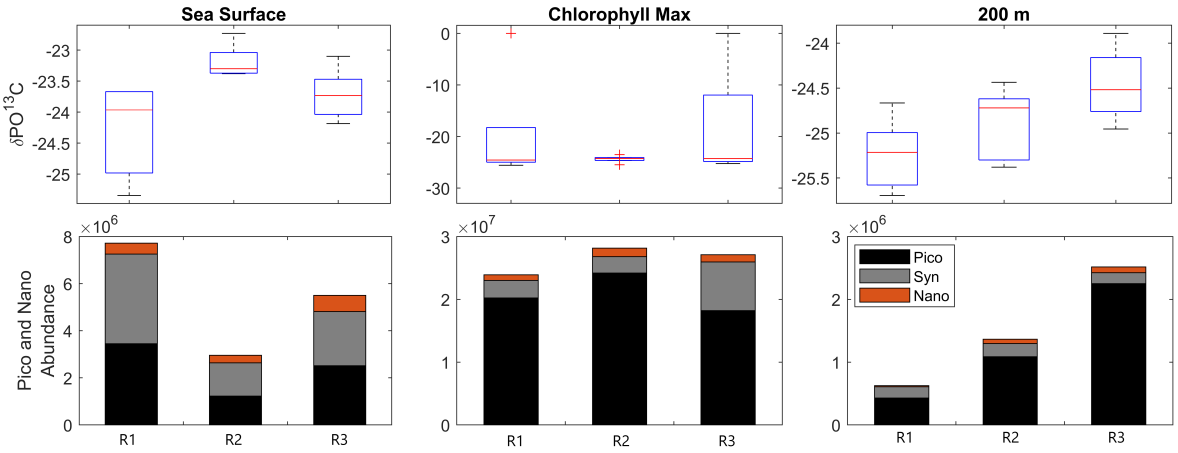

Figure 5.11: Box plot of $\delta PO^{13}C$, and a bar graph of picoplankton, synechoccus and nanoplankton in the different regions.

5.3.5 Summary

The results of the thermodynamic fractionation explain both the latitudinal trend in $\delta PO^{13}C$ at sea surface and the covariation between $\delta PO^{13}C$ and $\delta DI^{13}C$ (figure 5.9) . At the chl max depth, the thermodynamic effect is not evident, and the $\delta PO^{13}C$ variations are caused by factors controlling ϵ_p. ϵ_p varies with both $[CO_{2(aq)}]$ and the size of plankton groups, however, due to the uncertainties in figure 5.10 and 5.11 it is not possible to determine the cause for variations in ϵ_p. At 200 m the $\delta PO^{13}C$ is controlled by neither the thermodynamic effect or ϵ_p. At 200 m, there is no photosynthesis as it is below the euphotic zone. This means that the hypothesis that $\delta PO^{13}C$ is determined by the carbon the primary producers assimilated does not hold at this depth. At 200 m, $\delta PO^{13}C$ trend could be the result of respiration.

Chapter 6

Conclusion

The temperature and salinity reflect the Atlantic thermocline, gyre structures, and upwelling region, which determine the distribution of oxygen and nutrients. Also, due to the temperature dependence of DIC and salinity dependence of TA, the temperature and salinity reflect their distribution. In the subpolar regions the salinity and temperature is low and the thermocline is weak, which creates low TA, and high DIC and oxygen concentrations (due to the temperature effect on solubility). Because of the deep thermocline, the nutrient supply is high, and the region is productive during summer. The north subpolar region is the only oxygen undersaturated region due to the deep thermocline and the low temperature. In the subtropics, the temperature, salinity, and oxygen concentration are high at both the surface and at deeper layers due to the convergence in the region. The convergence in these regions is also responsible for the low nutrient supply and production. Whereas the low production and high salinity create high DIC and TA. In the equatorial regions, the salinity is low due to precipitation, while the temperatures are high above the thermocline, which creates low TA and DIC. Below the strong thermocline, the DIC and nutrient concentrations are high, while the oxygen concentration is low, because of the upwelling of old waters. The strong thermocline creates low nutrient concentrations in the surface layer, which results in low production. In the Brazil-Malvinas Confluence zone, the temperature and salinity are low, while the oxygen and nutrient concentrations are high because of the newly ventilated, nutrient-rich Antarctic waters entering the South Atlantic. During austral summer, this area is highly productive and has a high diatom abundance.

The controls on the particulate elemental ratio are only considered at the sea surface, and chl max depth and are evaluated by region and as a whole. For the entire transect, both nutrient limitation and temperature may control the elemental ratio. As the transect covers 100 degrees of latitude crossing several biomes, this might also reflect co-variation between nutrients and temperature, i.e., either nutrients or temperature controls the elemental ration, but as these co-vary themselves, both correlate with the elemental ratio. In region 1, the nutrient limitation

hypothesis is valid for NO_3^- concentration on the C:N ratio. However, this result may also be produced by the nitrogen fixators present in this region, which may also cause the N:P and temperature connection. The size of the plankton groups in region 1 indicates that the allometric diversity hypothesis may be valid; however, due to the high plasticity of picoplankton, the hypothesis is rejected. In region 2, the nutrient hypothesis is valid for NO_3^- concentration on the C:N ratio, while C:P may be controlled by PO_4^{3-} and temperature. Unlike region 1, there is no nitrogen fixation in region 2, which lends more confidence to the idea that the nutrient limitation hypothesis is valid in region 2. In region 3, both the temperature hypothesis and nutrient limitation hypothesis is valid, nor is there any nitrogen fixation. The allometric diversity hypothesis may be valid in this region but is rejected for the same reasons as region 1. In region 4, the temperature hypothesis and the allometric diversity mechanism likely dominates due to the diatom abundance and low temperature caused by the Malvinas current.

The change in fCO_2 between 1991-2018, 1995-2018, and 2013-2018 is dominated by the temperature difference caused by the season of when the cruise was conducted and by the increase in DIC. The cruises in 1991 and 2018 were conducted at approximately the same time of the year, and the main cause for fCO_2 increase was increased DIC due to intrusion of anthropogenic CO_2. The cruise in 1995 was conducted earlier in the year than in 2018 (October and December), and the fCO_2 change is caused by both the timing (south of 20°S) and the increase in DIC due to intrusion of anthropogenic CO_2 (between 10°N and 20°S). The cruise in 2013 took place earlier in the year than the cruise in 2018 (October and December), and the fCO_2 change appears caused by this difference in timing.

The variations of $\delta PO^{13}C$ in the sea surface appears to be mainly caused by the thermodynamic fractionation on the DIC -$CO_{2(aq)}$. The natural $[CO_{2(aq)}]$ may be contributing to the high $\delta PO^{13}C$, but this is not possible to determine with any certainty because of the effects of the intrusion of isotopically light anthropogenic CO_2. At the chl max depth, the $\delta PO^{13}C$ is controlled by ϵ_p. ϵ_p varies with the environmental conditions and the cell physiology of the given organism. Both the effect of natural $[CO_{2(aq)}]$ and the size of the plankton groups were tested to determine the latitudinal trend of ϵ_p, but neither can explains the trend due to uncertainties in the result. At 200 m the $\delta PO^{13}C$ is controlled by neither the thermodynamic effect or ϵ_p. Given the restriction of the measurements, it is therefore not possible to explain the variation in $\delta PO^{13}C$ at 200 m.

6.1 Outlook

For future studies, it would be beneficial to:

- Use data from several seasons to be able to study the different hypothesizes in more detail.
- Measure the size of the particulate matter to be able to test the allometric diversity hypothesis more correctly.

- Measure more plankton groups, in particular, diatoms, which is abundant in region 4 (by measurements of particulate and inorganic Si).
- Obtain data of the primary production (by a O_2/Ar instrument, as was intended for this research cruise). This would have indicated the rate of primary production and if there were a bloom in region 4.
- measure hydrogen, which is used to determine if nitrogen fixation is occurring because nitrogen fixation is affecting several variables.

Some practical improvements could be made during the research cruise. If there were done more CTD stations with more than three depths, it would be possible to create reliable contour plots. Also, because there were low material amounts on the filters, at least 1000 ml should always be used when filtering water samples from the open ocean.

Bibliography

Aandera (2018). Oxygen Optode 4831 / 4831F. *https://www.aanderaa.com/media/pdfs/oxygen-optode-4831_4831f.pdf*, pages 1–2 [Date Accessed: 2019–10–15].

Bakker, D. C., Pfeil, B., Landa, C. S., Metzl, N., O'Brien, K. M., Olsen, A., Smith, K., Cosca, C., Harasawa, S., Jones, S. D., Nakaoka, S. I., Nojiri, Y., Schuster, U., Steinhoff, T., Sweeney, C., Takahashi, T., Tilbrook, B., Wada, C., Wanninkhof, R., Alin, S. R., Balestrini, C. F., Barbero, L., Bates, N. R., Bianchi, A. A., Bonou, F., Boutin, J., Bozec, Y., Burger, E. F., Cai, W. J., Castle, R. D., Chen, L., Chierici, M., Currie, K., Evans, W., Featherstone, C., Feely, R. A., Fransson, A., Goyet, C., Greenwood, N., Gregor, L., Hankin, S., Hardman-Mountford, N. J., Harlay, J., Hauck, J., Hoppema, M., Humphreys, M. P., Hunt, C. W., Huss, B., Ibánhez, J. S. P., Johannessen, T., Keeling, R., Kitidis, V., Körtzinger, A., Kozyr, A., Krasakopoulou, E., Kuwata, A., Landschützer, P., Lauvset, S. K., Lefèvre, N., Lo Monaco, C., Manke, A., Mathis, J. T., Merlivat, L., Millero, F. J., Monteiro, P. M., Munro, D. R., Murata, A., Newberger, T., Omar, A. M., Ono, T., Paterson, K., Pearce, D., Pierrot, D., Robbins, L. L., Saito, S., Salisbury, J., Schlitzer, R., Schneider, B., Schweitzer, R., Sieger, R., Skjelvan, I., Sullivan, K. F., Sutherland, S. C., Sutton, A. J., Tadokoro, K., Telszewski, M., Tuma, M., Van Heuven, S. M., Vandemark, D., Ward, B., Watson, A. J., and Xu, S. (2016). A multi-decade record of high-quality fCO2 data in version 3 of the Surface Ocean CO2 Atlas (SOCAT). *Earth System Science Data*, 8(2):383–413.

Becker, M. (2016). *Autonomous 13C measurements in the North Atlantic - a novel approach for identifying patterns and driving factors of the upper ocean carbon cycle.* Phd thesis, Universität zu Kiel.

Bhattacharyya, G. K. and Johnson, R. A. (1977). Correlation: A Measure of Linear Relationship. In *Statistical Concepts and Methods*, chapter 12, pages 400–420. John Wiley & Sons, Inc.

Corporation, T. E. (2005). DELTA V Advantage | DELTA V Plus. *http://www.ebd.csic.es/lie/PDF/DELTA_V_AdvantagePDF_26513.pdf*, pages 1–16.

Dickson, A. G. (1990). Standard potential of the reaction: AgCl(s) + 1 2H2(g) = Ag(s) + HCl(aq), and and the standard acidity constant of the ion HSO4- in synthetic sea water from 273.15 to 318.15 K. *The Journal of Chemical Thermodynamics*, 22(2):113–127.

Dickson, A. G., Sabine, C. L., and Christian, J. R. (2007). Guide to Best Practices for Ocean CO2 Measurements. *IOCCP Report*, 3(8):191 pp.

Dlugokencky, E. and Tans, P. (2019). Globally averaged marine surface annual mean data. *www.esrl.noaa.gov/gmd/ccgg/trends/*, pages 1 [Date Accessed: 2019–11–01].

Eide, M., Olsen, A., Ninnemann, U. S., and Eldevik, T. (2017). A global estimate of the full oceanic 13C Suess effect since the preindustrial. *Global Biogeochemical Cycles*, 31(3):492–514.

Fisher, T. (2013). Thermo Scientific GasBench II. *https://assets.thermofisher.com/TFS-Assets/CMD/brochures/BR-30036-IRMS-GasBench-II-BR30036-EN.pdf*, pages 1 [Date Accessed: 2019–09–05].

Fisher, T. (2015). Attune ™ NxT Acoustic Focusing Cytometer. *http://tools.thermofisher.com/content/sfs/manuals/100024235_AttuneN*
(100024235):1 [Date Accessed: 2019–05–30].

Francey, R. J., Allison, C. E., Etheridge, D. M., Trudinger, C. M., Enting, I. G., Leuenberger, M., Langenfelds, R. L., Michel, E., and Steele, L. P. (1999). A 1000-year high precision record of δ 13 C in atmospheric CO 2 A 1000-year high precision record of d13C in atmospheric CO 2. *Tellus*, 51(2):170–193.

Galbraith, E. D. and Martiny, A. C. (2015). A simple nutrient-dependence mechanism for predicting the stoichiometry of marine ecosystems. *Proceedings of the National Academy of Sciences of the United States of America*, 112(27):8199–8204.

Garcia, C. A., Baer, S. E., Garcia, N. S., Rauschenberg, S., Twining, B. S., Lomas, M. W., and Martiny, A. C. (2018). Nutrient supply controls particulate elemental concentrations and ratios in the low latitude eastern Indian Ocean. *Nature communications*, 9(1):4868.

Gundersen, K. and Lunde, L. F. (2015). En kort sammenfatning av analytiske prinsipp og litteratur referanser for metoder brukt ved Kjemilaboratoriet , fagområde uorganisk kjemi Innholdsfortegnelse. *Havforskningsinstituttet*, 3:1–11.

Heinze, C., Meyer, S., Goris, N., Anderson, L., Steinfeldt, R., Chang, N., Le Quéré, C., and Bakker, D. C. E. (2015). The ocean carbon sink – impacts, vulnerabilities and challenges. *Earth System Dynamics*, 1:327–358.

Ito, T. and Follows, M. J. (2005). Preformed phosphate, soft tissue pump and atmospheric CO2. *Journal of Marine Research*, 63(4):813–839.

Ito, T., Follows, M. J., and Boyle, E. A. (2004). Is AOU a good measure of respiration in the oceans? *Geophysical Research Letters*, 31(17):1–4.

Keeling, R. F., Arne, K., and Gruber, N. (2010). Ocean Deoxygenation in a Warming World. *Annual Review of Marine Science*, 2:199–229.

Langdon, C. (1991). Titration Using the Amperometric Technique. *The GO-SHIP Repeat Hydrographical Manual: A Collection of Expert Reports and Guidelines*, pages 1–18.

Laufkötter, C., Vogt, M., and Gruber, N. (2013). Long-term trends in ocean plankton production and particle export between 1960-2006. *Biogeosciences*, 10(11):7373–7393.

Laufkotter, C., Vogt, M., Gruber, N., Aita-Noguchi, M., Aumont, O., Bopp, L., Buitenhuis, E., Doney, S. C., Dunne, J., Hashioka, T., Hauck, J., Hirata, T., John, J., Le Quere, C., Lima, I. D., Nakano, H., Seferian, R., Totterdell, I., Vichi, M., and Volker, C. (2015). Drivers and uncertainties of future global marine primary production in marine ecosystem models. *Biogeosciences*, 12(23):6955–6984.

Leblanc, K., Quéguiner, B., Diaz, F., Cornet, V., Michel-Rodriguez, M., Durrieu De Madron, X., Bowler, C., Malviya, S., Thyssen, M., Grégori, G., Rembauville, M., Grosso, O., Poulain, J., De Vargas, C., Pujo-Pay, M., and Conan, P. (2018). Nanoplanktonic diatoms are globally overlooked but play a role in spring blooms and carbon export. *Nature Communications*, 9(1):1–12.

Lee, K., Tong, L. T., Millero, F. J., Sabine, C. L., Dickson, A. G., Goyet, C., Park, G. H., Wanninkhof, R., Feely, R. A., and Key, R. M. (2006). Global relationships of total alkalinity with salinity and temperature in surface waters of the world's oceans. *Geophysical Research Letters*, 33(19):1–5.

Lewis, E. and Wallace, D. (1998). Program developed for CO2 system calculations. *ORNL/CDIAC-105*, pages 1–38.

Longhurst, A. (1995). Seasonal cycles of pelagic production and consumption. *Progress in Oceanography*, 36(2):77–167.

Longhurst, A. R. (2007). Ecological Geography of the Sea. *Academic Press*, pages 35–40,89–113.

Lueker, T. J., Dickson, A. G., and Keeling, C. D. (2000). Ocean p CO 2 calculated from dissolved inorganic carbon , alkalinity , and equations for K 1 and K 2 : validation based on laboratory measurements of CO 2 in gas and seawater at equilibrium. *Marine Chemestry*, 70:105–119.

Luis Otero-Ferrer, J., Cermeño, P., Bode, A., Fernández-Castro, B., Gasol, J. M., Morán, X. A. G., Marañon, E., Moreira-Coello, V., Varela, M. M., Villamaña, M., and Mouriño-Carballido, B. (2018). Factors controlling the community structure of picoplankton in contrasting marine environments. *Biogeosciences*, 15(20):6199–6220.

Maier-Reimer, E. and Hasselmann, K. (1987). Transport and storage of CO2 in the ocean ——an inorganic ocean-circulation carbon cycle model. *Climate Dynamics*, 2(2):63–90.

Markgraf, B. (2018). Carleton University: The Winkler Method – Measuring Dissolved Oxygen. *https://sciencing.com/winkler-titration-method-6076224.html*, pages 1 [Date Accessed: 2019–05–30].

Martiny, A. C., Pham, C. T., Primeau, F. W., Vrugt, J. A., Moore, J. K., Levin, S. A., and Lomas, M. W. (2013). Strong latitudinal patterns in the elemental ratios of marine plankton and organic matter. *Nature Geoscience*, 6(4):279–283.

Nier, A. O. (1950). A redetermination of the relative abundances of the isotopes of carbon, nitrogen, oxygen, argon, and potassium. *Physical Review*, 77(6):789–793.

NOAA (2019a). Climate at a Glance: Global Time Series. *NOAA National Centers for Environmental information, URL: https://www.ncdc.noaa.gov/cag/*, pages [Date Accessed: 2019–11–01].

NOAA (2019b). Cold & Warm Episodes by Season. *URL: https://origin.cpc.ncep.noaa.gov/products/analysis_monitoring/ensostuff/ONI+* pages [Date Accessed: 2019–11–13].

Ödalen, M., Nycander, J., Oliver, K. I., Brodeau, L., and Ridgwell, A. (2018). The influence of the ocean circulation state on ocean carbon storage and CO2 drawdown potential in an Earth system model. *Biogeosciences*, 15(5):1367–1393.

Ohkouchi, N., Ogawa, N. O., Chikaraishi, Y., Tanaka, H., and Wada, E. (2015). Biochemical and physiological bases for the use of carbon and nitrogen isotopes in environmental and ecological studies. *Progress in Earth and Planetary Science*, 2(1):1–17.

O'Leary, M. H. (1981). ScienceDirect.com - Phytochemistry - Carbon isotope fractionation in plants. *Phytochemistry*, 20(4):5–567.

Olguín Salinas, H. F., Brandini, F., and Boltovskoy, D. (2015). Latitudinal patterns and interannual variations of spring phytoplankton in relation to hydrographic conditions of the southwestern Atlantic Ocean (34°–62°S). *Helgoland Marine Research*, 69(2):177–192.

Olsen, A., Key, R. M., Van Heuven, S., Lauvset, S. K., Velo, A., Lin, X., Schirnick, C., Kozyr, A., Tanhua, T., Hoppema, M., Jutterström, S., Steinfeldt, R., Jeansson, E., Ishii, M., Pérez, F. F., and Suzuki, T. (2016). The global ocean data analysis project version 2 (GLODAPv2) - An internally consistent data product for the world ocean. *Earth System Science Data*, 8(2):297–323.

Paulino, A., Heldal, M., Norland, S., and Egge, J. (2013). Elemental stoichiometry of marine particulate matter measured by wavelength dispersive X-ray fluorescence (WDXRF) spectroscopy. *Journal of the Marine Biological Association of the United Kingdom*, 93(8):2003–2014.

Peltzer, E. T. (2016). lsqbisec. *https://www.mbari.org/index-of-downloadable-files/*, pages 1 [Date Accessed: 2019–06–17].

Pierrot, D., Neill, C., Sullivan, K., Castle, R., Wanninkhof, R., Lüger, H., Johannessen, T., Olsen, A., Feely, R. A., and Cosca, C. E. (2009). Recommendations for autonomous underway pCO2 measuring systems and data-reduction routines. *Deep-Sea Research Part II: Topical Studies in Oceanography*, 56(8-10):512–522.

Pitta, P., Nejstgaard, J. C., Tsagaraki, T. M., Zervoudaki, S., Egge, J. K., Frangoulis, C., Lagaria, A., Magiopoulos, I., Psarra, S., Sandaa, R. A., Skjoldal, E. F., Tanaka, T., Thyrhaug, R., and Thingstad, T. F. (2016). Confirming

the "rapid phosphorus transfer from microorganisms to mesozooplankton in the eastern mediterranean sea" scenario through a mesocosm experiment. *Journal of Plankton Research*, 38(3):1–20.

Port, R. (2019). The LI-820 CO 2 Gas Analyzer. *http://www.echokr.com/down/05_1.pdf*, pages 1 [Date Accessed: 2019–05–30].

Quéré, C., Andrew, R., Friedlingstein, P., Sitch, S., Hauck, J., Pongratz, J., Pickers, P., Ivar Korsbakken, J., Peters, G., Canadell, J., Arneth, A., Arora, V., Barbero, L., Bastos, A., Bopp, L., Ciais, P., Chini, L., Ciais, P., Doney, S., Gkritzalis, T., Goll, D., Harris, I., Haverd, V., Hoffman, F., Hoppema, M., Houghton, R., Hurtt, G., Ilyina, T., Jain, A., Johannessen, T., Jones, C., Kato, E., Keeling, R., Klein Goldewijk, K., Landschützer, P., Lefèvre, N., Lienert, S., Liu, Z., Lombardozzi, D., Metzl, N., Munro, D., Nabel, J., Nakaoka, S. I., Neill, C., Olsen, A., Ono, T., Patra, P., Peregon, A., Peters, W., Peylin, P., Pfeil, B., Pierrot, D., Poulter, B., Rehder, G., Resplandy, L., Robertson, E., Rocher, M., Rödenbeck, C., Schuster, U., Skjelvan, I., Séférian, R., Skjelvan, I., Steinhoff, T., Sutton, A., Tans, P., Tian, H., Tilbrook, B., Tubiello, F., Van Der Laan-Luijkx, I., Van Der Werf, G., Viovy, N., Walker, A., Wiltshire, A., Wright, R., Zaehle, S., and Zheng, B. (2018). Global Carbon Budget 2018. *Earth System Science Data*, 10(4):2141–2194.

Sarmiento, J. L. and Gruber, N. (2006). Ocean Biogeochemical Dynamics. *Prinston University Pre*, page 503.

Sarmiento, J. L., Hughes, T., Stouffer, R. J., and Manabe, S. (1998). Simulated response of the ocean carbon cycle to anthropogenic climate warming. *Nature*, 395(6682):245–249.

Sathyendranath, S. and Platt, T. (2001). Primary Production Distribution. *Encyclopedia of Ocean Sciences*, pages 2272–2277.

SBE (2013). Sea Bird Electronics 63 Digital Optical Dissolved Oxygen Sensor. *http://www.comm-tec.com/Docs/Manuali/SBE/63_006.pdf*, pages 1–49.

SBE (2015a). Sea Bird Electronics 21 SEACAT Thermosalinograph. *SBE 21 SEACAT Thermosalinograph*, pages 1–64.

SBE (2015b). Sea Bird Electronics 9plus CTD 50089. *SBE 9plus CTD 50089*, pages 50246–50246.

SBE (2016). Sea Bird Electronics CTD SBE 911plus. *http://sbe.seabird.com/products/spec_sheets/911data.htm*, pages 0–1.

Sigman, D. and Fripiat, F. (2019). Nitrogen Isotopes in the Ocean. *Encyclopedia of Ocean Sciences*, (1997):263–278.

Takahashi, T. (2002). Global air-sea flux of CO2 based on surface ocean pCO2, and seasonal biological and temperature effects. *Deep-Sea Research Part II*, 49:1601–1622.

Takahashi, T., Olafsson, J., Goddard, J. G., Chipman, D. W., and Sutherland, S. (1993). Seasonal variation of CO2 and nutrients in the high-latitude surface oceans. *Global Biogeochemical Cycles*, 7(4):843–878.

Talley, L. D. and Pickard, G. L. (2011). Descriptive physical oceanography : an introduction. *Eleviser*.

Toseland, A., Daines, S. J., Clark, J. R., Kirkham, A., Strauss, J., Uhlig, C., Lenton, T. M., Valentin, K., Pearson, G. A., Moulton, V., and Mock, T. (2013). The impact of temperature on marine phytoplankton resource allocation and metabolism. *Nature Climate Change*, 3(11):979–984.

Tuerena, R. E., Ganeshram, R. S., Humphreys, M. P., Browning, T. J., Bouman, H., and Piotrowski, A. P. (2019). Isotopic fractionation of carbon during uptake by phytoplankton across the South Atlantic subtropical convergence. *Biogeosciences Discussions*, pages 1–29.

Tyrrell, T. (2001). Redfield Ratio. *Encyclopedia of Ocean Sciences*, 4:2377–2386.

Uppström, L. R. (1974). The boron/chlorinity ratio of deep-sea water from the Pacific Ocean. *Deep-Sea Research and Oceanographic Abstracts*, 21(2):161–162.

Weiss, R. F. (1974). CARBON DIOXIDE IN WATER AND SEAWATER: THE SOLUBILITY OF A NON-IDEAL GAS. *Eleviser Scientific*, 2:203–215.

Zeebe, R. E. and Wolf-Gladrow, D. (2001). CO2 IN SEAWATER: EQUILIBRIUM, KINETICS, ISOTOPES. *Elsevier*.

Zhang, J., Quay, P. D., and Wilbur, D. O. (1995). Carbon isotope fractionation during gas-water exchange and dissolution of CO2. *Geochimica et Cosmochimica Acta*, 59(1):107–114.